INTRINSICALLY GREEN FLUORESCENT PAMAM AS NANOCARRIER AND NANOPROBE FOR TRACEABLE AND CONTROLLED DRUG DELIVERY AND BIO-IMAGING

By

Guoying Wang

Department of Biomedical Sciences

Supervisors:

Dr. Bingyang Shi, Dr. Adam Walker, Prof. Roger Chung

MACQUARIE University
SYDNEY·AUSTRALIA

This thesis is presented for the degree of Doctor of Philosophy

November 2019

Statement of Originality

This work has not previously been submitted for a degree or diploma in any university. To the best of my knowledge and belief, the thesis contains no material previously published or written by another person except where due reference is made in the thesis itself.

The research presented in this thesis was approved by Macquarie University Ethics Review Committee, AEC reference number: 2015/033-22.

Guoying Wang   07-Nov-2019

Acknowledgments

I would like to express the deepest appreciation to all the people who have contributed in some way to the project mentioned in this thesis. Foremost, I would like to express my sincere gratitude to my principle supervisor Dr. Bingyang Shi who has helped and encouraged me at all stages of my thesis work with immense care and great patience. His motivation, enthusiasm, and extensive knowledge have deeply infected me during my PhD period. His timely advices, meticulously scrutiny and rich experimental skills have helped me to accomplish my PhD tasks in a large extent.

I am also sincerely grateful to my associate supervisor Dr. Adam Walker, who opened up my knowledge in understanding the mechanism of amyotrophic lateral sclerosis (ALS) diseases that built up the foundation of this thesis. I am thankful for his professional advices and thoughtful comments to my projects that gave me a lot of new thoughts in managing my programs. Especially, I would like to appreciate Prof. Roger Chung, who has provided this creative MND platform for us to have a great opportunity in studying MND.

Besides my supervisors, I would like express my special thanks to Dr. Marco Morsch, who has given me great help in preparing zebrafish, operating zebrafish injections, fish imaging and data analysis. Without his help I can't get so many valuable animal data to support my thesis. Here, I would like to express my heartfelt thanks to Dr. Marco for his support in this thesis. Furthermore, I would like show my best acknowledges to Dr. Yiqing Lu, his extensive knowledge and rigorous scientific attitude has deeply infected me, also his professional advices have helped me solved a lot problems related to my thesis works. I would like also express my deepest thanks to Dr.Nima Sayyadi, who has given me plenty of professional comments on my thesis work.

My sincere thanks also goes to other fellows in Roger's group who had a significant impact on this work. Firstly, I would like to express my sincere thanks to Dr. Libing Fu, who has offered me great support in experiments design, sample preparation, data analysis and manuscript writing. I would like to especially thank Dr. Rowan Radford, who provided me several important antibodies that were very useful for my project. He also gave me grate help in operating the confocal microscopy and the data processing software, which was grateful to support my thesis. I would also like to especially thank Mr. Andres Vidal-itriago, who has provided me a special gene-edited zebrafish line. Other members, Miss Flora Cheng, Dr. Amanda Wright, Miss Stephanie Rayner, who have given me great help in operating western blot, immunostaining, I would like to express my most sincere thanks to all of them.

My grateful acknowledge also goes to the International Macquarie University Research Excellence Scholarship (iMQRES) that gives me financial support for my PhD project.

Finally, I would like to acknowledge my beloved family, my wife, my parents, for their love, selfless support and encouragement to finish my studies. A special thanks to my wife, Amy, who has always been there with me and encouraged me, let me no longer feel so lonely in a foreign country. A special thanks to my son George, who has brought so much joy in my life. I am so happy to watch him grow up.

List of Publications

1. G. Wang, L. Fu, A. Walker, X. Chen, D. Lovejoy, M. Hao, A. Lee, R. Chuang, H. Rizos, M. Irvine, M. Zheng, X. Liu, Y. Lu, B. Shi. Label-free fluorescent poly (amidoamine) dendrimer for traceable and controlled drug delivery. *Biomacromolecules*. 2019 20 (5), 2148-2158.

2. J. Zhu, G. Wang, C. Alves, H. Tomas, Z. Xiong, M. Shen, J. Rodrigues, X. Shi. Multifunctional Dendrimer-Entrapped Gold Nanoparticles Conjugated with Doxorubicin for pH-Responsive Drug Delivery and Targeted Computed Tomography Imaging. *Langmuir,* 2018, 34(41): 12428-12435.

3. Z. Cao, N. Adnan, G. Wang, A. Rawal, B. Shi, R. Liu, K. Liang, L. Zhao, J. Gooding, C. Boyer, Z. Gu. Enhanced colloidal stability and protein resistance of layered double hydroxide nanoparticles with phosphonic acid-terminated PEG coating for drug deliver. *Journal of colloid and interface science* 521 (2018): 242-251.

4.L. Fu, M. Morsch, B. Shi, G. Wang, A. Lee, R. Radford, Y. Lu, D. Jin, R. Chuang. "A versatile upconversion surface evaluation platform for bio–nano surface selection for the nervous system." *Nanoscale* 9, no. 36 (2017): 13683-13692.

5. G. Wang, B. Shi, A. Walker. Nanotechnology inspired new strategies for treatments in ALS. Prepare to submit to *Biomaterials*.

6. G. Wang, L. Fu, M. Morsch, B. Shi, A. Walker, R. Chuang, N. Sayyadi, A. Vidal-Itrigo. Intrinsic Green Fluorescent PAMAM as Nanoprobe for Zebrafish Fluorescence Imaging. Prepare to submit to *Small*.

7. G. Wang, L. Fu, B. Shi, A. Walker, R. Chuang, N. Sayyadi. A. Wright. Intrinsically Fluorescent PAMAM Dendrimer as Drug Carrier for Neuron Protection Study. Prepare to submit to *Advanced Healthcare Materials*.

8. G. Wang, Y. Sun, J. Wang, Y. Li, Y. Yuan, C. Liu, B. Shi. Multistage Delivery Nanocarriers with Enhanced Penetration into Tumor Tissue and Tunable Release Controllability. Prepare to submit to ***Advanced Functional Materials.***

([1], [5], [6], [7] are closely related to my PhD project)

Conference Papers

1) G. Wang, L. Fu, B. Shi. Developing a new endogenous fluorescent poly(amidoamine) dendrimer for traceable and controlled drug delivery. *ICBS 2017 - International Chemical Biology Society, 2017, Shanghai, China.* (Poster, First Author)

2) G. Wang, L. Fu, B. Shi. Developing a new endogenous fluorescent poly(amidoamine) dendrimer for traceable and controlled drug delivery. *2nd Annual EnCouRage Research Symposium, 2017, Sydney, Australia.* (Poster, First Author)

3) G. Wang, A. Babazadeh, B. Shi. Intrinsically Fluorescent PAMAM Dendrimer as Drug carrier and Nanoprobe: Bioimaging and Neuron Protection Study. *Macquarie Neurodegeneration Meeting, Macquarie University, 2019, Sydney, Australia.* (Poster, First Author)

4) G. Wang, M. Morsch, B. Shi. Intrinsically Fluorescent PAMAM Dendrimer as Nanocarrier and Nanoprobe: Bioimaging and Neuron Protection Study. *International Conference on Nanoscience and Nanotechnology (ICONN 2020). Brisbane, Australia.* (Oral, Conference speaker)

INTRINSICALLY GREEN FLUORESCENT PAMAM AS NANOCARRIER AND NANOPROBE FOR TRACEABLE AND CONTROLLED DRUG DELIVERY AND BIO-IMAGING

Abstract

Amyotrophic lateral sclerosis (ALS) is a rapidly progressive neurodegeneration disease that mainly affects motor neurons that control muscle movement. Patients normally die with respiratory muscle failure within 3~5 years from the time of diagnosis. Current therapeutic approaches can only modestly slow the disease progress. Recent advances in nanotechnology have shown great potential for developing a nano-based therapeutic strategy in enhancing the power of ALS therapeutic agents. Those benefits including but not limited to: (1) Improve the drug's bioavailability/bio-stability; (2) Enhance the biological barriers penetration; (3) Target specific disease sites; (4) Traceable drug/gene delivery. Therefore, it is of great importance to develop multifunctional nanomaterials that can be used in delivering ALS treatment drugs.

Among numerous nanomaterials, intrinsically fluorescent Poly(amidoamine) dendrimers (IF-PAMAM) have attracted extensive attention in the fields of biological imaging and drug delivery due to their detectable signals, small size, excellent biocompatibility, abundant functional terminal groups, and superior photo-stability. To date, several intrinsically blue fluorescent PAMAM dendrimers have been successfully applied for traceable drug/gene delivery. However, those blue fluorescent dendrimers typically require UV as the excitation light, which may cause side effects to healthy cells or tissues. Additionally, under UV excitation, the emission spectra from those PAMAM dendrimers were mainly concentrated at the range of 400 ~500 nm, which was close to the spontaneous fluorescence spectra from biological tissues, thus affecting their effect as fluorescent probes for *in vivo* application. Therefore, the development of biocompatible, photo-stable, and high fluorescence performance PAMAM dendrimers for traceable drug delivery or bio-imaging is still a challenge.

In my PhD project, we firstly developed a novel highly biocompatible and label-free (intrinsically) fluorescent PAMAM through a simple reaction of NH_2-terminated PAMAM (Generation 5) with acetaldehyde. This unique intrinsically fluorescent PAMAM (FG5) emitted a strong green fluorescence under the maximum excitation around 485 nm. Due to the replacement of the positively charged amino groups with neutrally charged methyl groups, the inherent cytotoxicity of NH_2-terminated PAMAM was largely eliminated. The higher excitation wavelength made the FG5 a much safer drug carrier for tracking and bio-imaging. The fluorescent anti-cancer drugs Doxorubicin (DOX) were selected as model drugs to evaluate the dual-tracking (nanocarrier and payload) capability of this system, thus providing base for delivering other clinic important drugs. The effective delivery of nanocomposites to melanoma cancer cells (SKMEL28) and excellent intracellular tracing of these nanoparticles suggest that these novel FG5 are warrant for further study of other clinical drugs.

Selective targeting of motor neuron protective drugs to the central nervous system (CNS) remains a great challenge for effective amyotrophic lateral sclerosis (ALS) therapy due to the presence of blood-brain barrier (BBB) and blood spinal cord barrier (BSCB). Therefore, the second aim of the thesis was to assess the CNS targeting capability of the fabricated FG5. In this chapter, Transferrin (Tf) was selected as a transport ligand to facilitate the BBB penetration of carrier/drug nanocomplexes. Neuron protection drug Edaravone (EDV) was encapsulated in the PEGylated FG5 (FGP), and Tf functionalized FG5 (FGP-Tf) by a solvent replacement (precipitation) method. The enhanced BBB transportation and elevated neuron protection function of EDV loaded FGP-Tf (FGP-Tf/EDV) were confirmed by the *in vitro* BBB model and motor neuron cells model. To the best of our knowledge, this is the first report of IF-PAMAM as a nanocarrier for neuroprotective drug delivery, which is of great importance in developing IF-PAMAM based nanomedicines for ALS treatment.

To accelerate the transformation of IF-PAMAM-based nanomedicines from theoretical to clinical, it is practically required to evaluate the *in vivo* behaviour through standard animal models. Therefore, the third aim of this thesis was to fill the gaps in utilizing intrinsically fluorescent PAMAM dendrimers in *in vivo* models. The excellent performance for *in vivo* imaging and real-time tracking of our fabricated FG5 was verified by the strong *in vivo* green fluorescent signals, superior photo-stability, and very low fluorescent background (noise) from biological organisms. Additionally, we also provided a simple and effective zebrafish platform to evaluate the *in vivo* behaviour of IF-PAMAM based nanoprobes, which was beneficial for optimizing IF-PAMAM based nanostructure for future *in vivo* drug delivery.

Through the comprehensive study in this thesis, we thereby developed a novel intrinsically green fluorescent PAMAM with excellent biocompatibility, remarkable fluorescent performance, superior photo-stability that provided the fundamental nanomaterial (multifunctional PAMAM) for this thesis. Importantly, the enhanced BBB transportation and neuron protection function of FGP-Tf/EDV in *in vitro* models, accompanied with the prolonged blood circulation, and excellent tissue diffusion function of FGP-Tf in *in vivo* zebrafish model provided a solid basis for further evaluating the therapeutic effect of FGP-Tf/EDV in ALS animal models.

Key Words: IF-PAMAM, drug delivery, bio-imaging, BBB, zebrafish, ALS

Contents

List of Abbreviation (in alphabetic order)

Abbreviation	Description
AD	Alzheimer's disease
ALS	Amyotrophic lateral sclerosis
BBB	Blood brain barrier
BSCB	Blood spinal cord barrier
BSA	Bovine serum albumin
CA	Caudal artery
CNS	Central nervous system
CV	Caudal vein
DLS	Dynamic light scattering
DMEM	Dulbecco`s Modified Eagle Media
DOX	Doxorubicin
DOX·HCl	Doxorubicin hydrochloride
EDV	Edaravone
ER	Endoplasmic Reticulum Stress
FBS	Fetal bovine serum
FCM	Flow cytometry
FDA	Food and Drug Administration
FG5	Intrinsically fluorescent PAMAM, generation 5
FITC	Fluorescein isothiocyanate

FTIR	Fourier Transform Infrared Spectroscopy
GFP	Green fluorescent protein
IF-PAMAM	Intrinsically fluorescent PAMAM
I.V.	Intravenous injection
LSCM	Laser scanning confocal microscopy
MND	Motor neuron disease
NHS	N-Hydroxysuccinimide
NPs	Nanoparticles
PAMAM	Poly(amidoamine) dendrimer
PBS	Phosphate buffered saline
PD	Parkinson's disease
PEG	Polyethylene glycol
PEI	Polyethylenimine
ROS	Reactive oxygen species
TDP-43	TAR DNA-binding protein 43
TEA	Triethylamine
TEM	Transmission electron microscopy
Tf	Transferrin
UCNPs	Upconversion nanoparticles
UV	Ultraviolet

Chapter 1 Introduction

1.1 Project background and structure

Amyotrophic lateral sclerosis (ALS) is a serious neurodegenerative disease that mainly affects motor neurons that control muscle movement. The complicated pathogenesis of ALS has resulted in limited therapy options. Besides, the insufficient cerebral drug accumulation, deficient bioavailability, short life time, and "off-target" effect of many ALS treatment drugs have significantly hindered their therapeutic efficiency. To address the above limitations in ALS treatment, new strategies are practically required. Encouragingly, the great achievements of nanotechnology-based approaches in treating neurodegenerative diseases (e.g. AD, PD) in the last few years have opened a gate for nano-based ALS treatment.

Among numerous nanostructures, Poly(amidoamine) dendrimers (PAMAM) are well known for their excellent performance as drug/gene delivery vehicles and nanoprobes due to their smaller size, monodisperse, abundant functional terminal groups, and large internal cavity. Those unique properties have provided PAMAM dendrimers great potential in delivering therapeutic agents for ALS treatment. However, the inherent cytotoxicity and a lack of detectable signals have hindered their practical applications. Various approaches have been implemented to make PAMAM visible, most frequently through the conjugation of fluorophore molecules, such as FITC, Cy5 and Alexa Fluor series, onto the dendritic scaffold of PAMAM. However, fluorophore labelling may affect the size, surface structure, hydrophilicity, and biocompatibility of the PAMAM dendrimers. In addition, the detachment or degradation of labelled fluorophore, accompany with the photo-bleaching were other problems that may affect the fluorescence performance of those fluorescent PAMAM. Fortunately, 20 years ago, researchers found a weak intrinsically blue fluorescence from OH-terminated PAMAM in an accidental experiment, after that, people have developed a variety of intrinsically fluorescent PAMAM, typically through oxidation, low pH, or chemical engineering.

However, the majority of those PAMAM dendrimers mainly emit blue fluorescence and usually require ultraviolet light as an excitation source, which will inevitably bring some negative effects, such as biosafety under UV stimulation and auto-fluorescence from biological organisms. Therefore, developing more powerful intrinsically fluorescent PAMAM dendrimers remains challenging.

In this PhD project, we aim to design and develop a novel intrinsically fluorescent PAMAM with high emission intensity, high biocompatibility, low fluorescent background from biological organisms, and superior photo stability that can be used for traceable drug delivery and bio-imaging. Previous report from our group has demonstrated an intrinsically fluorescent acetaldehyde-modified-cystine linker. Due to the n-π* transition in formed Schiff bases structures, this linker can emit green fluorescence. Inspired by this mechanism, we made a hypothesis that this kind of intrinsic fluorescence can also be applied for PAMAM dendrimers. Thereby, the main lines of this thesis including: (1) Prove the hypothesis that Schiff-base can induce intrinsically green fluorescence in PAMAM; (2) Evaluate the fluorescence performance; (3) Apply these materials for controlled and traceable drug delivery by using a fluorescent drug model; (4) Utilize these materials for *in vitro* and *in vivo* imaging. The structure of the PhD project is illustrated in Fig 1.
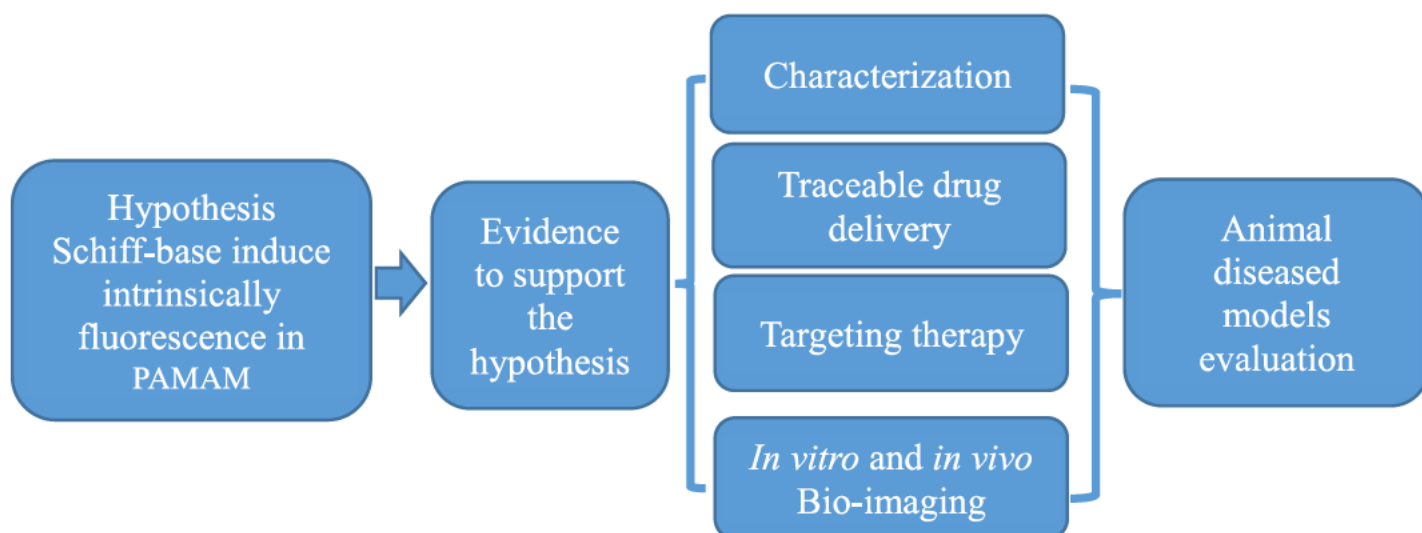
Figure 1 The outline of the PhD project

1.2 Objectives and strategy

1) To prove the hypothesis, amino groups-terminated PAMAM dendrimer were modified with acetaldehyde. The optical and physical properties were characterized. (Chapter 3)

2) To realize the dual tracking of nanocarriers and cargoes, a fluorescent drug Doxorubicin (DOX) was encapsulated in the PAMAM internal cavity. (Chapter 3)

3) To achieve targeted therapy, the intrinsically fluorescent PAMAM was further functionalized with brain targeting protein (Transferrin). (Chapter 4)

4) To evaluate the neuron protection capability, the neuron protection drug Edaravone was selected as a drug model and encapsulated in the PAMAM internal cavity. (Chapter 4)

5) To assess the *in vivo* tracking and bio-imaging function, a transparent zebrafish model was used to evaluate the *in vivo* behaviours of those intrinsically fluorescent PAMAM, such as fluorescent performance, blood circulation, bio-distribution, biological barrier penetration, and particle localization et al. (Chapter 5)

1.3 Thesis Structure

This thesis is composed by 1 literature review paper and 3 research papers. The research manuscript from chapter 3 has already been published. The review paper and other 2 research papers have been prepared for submission.

Chapter 2 Literature review

In chapter 1, we have introduced the background and structure of this thesis including the basic knowledge of ALS and why we choose nanotechnology to combat this disease. Thus, it's important to systematically introduce the recent advances of nanotechnologies in ALS to give us guideline to develop novel nanomaterials to treat ALS. The highlights of this review include:

1. Summary introduction of proposed pathogenic mechanisms of ALS.

2. Current challenges of delivering ALS therapeutic agents to CNS.

3. Opportunities for nanotechnology-based strategies to mediate ALS therapeutic drug delivery to CNS.

4. Current therapeutic strategies specifically targeting ALS pathophysiology and how nanomaterials can be designed to enhance the power of ALS therapeutic drugs.

5. Other emerging nanotechnologies for potential ALS drug delivery.

6. Perspectives in nano-based strategies for ALS treatment.

The overall objective of this review is to broaden the understanding of the design and to develop nanostructures that can serve for ALS treatment.

  This literature review has been prepared to submit to *Biomaterials*. I am the first author of this manuscript. The majority of this work was completed by myself (>80%) from literature organizing to manuscript writing. Dr. Bingayang Shi has given me plenty of professional comments and suggestions in constructing the manuscript structure.

Nanotechnology inspired new strategies for treatments in ALS

Guoying Wang[1], Bingyang Shi[1]

1.Department of Biomedical Sciences, Faculty of Medicine & Health Sciences, Macquarie University, Sydney, NSW 2109, Australia

Abstract

Amyotrophic lateral sclerosis (ALS), also known as motor neuron disease (MND), is a progressive neurodegeneration disease that affects both upper and lower motor neurons, which results in losing muscle control and eventual paralysis [1]. The main obstacle limiting ALS treatment is that the causes of spontaneous ALS (sALS) are extremely complicated and largely unknown. Scientists are exerting to exploit new therapeutic strategies based on the disclosed molecular, cellular functions of the nervous system and the identified genes that cause ALS. Unfortunately, the translational progress in ALS clinical trials is almost stagnant. The insufficient bioavailability/bio-stability, inadequate cerebral accumulation, and the "off-target" effect are some of the major obstacles that hinder the clinical efficacy of many ALS therapeutic agents. In the last few years, significant advances in nanotechnology have shown great potential in addressing one or more obstacles that limiting the application of ALS drugs in clinical, opening the gate for nano-based therapeutic strategies of ALS treatment. Therefore, the systematic introduction of the recent advances of nanotechnologies in ALS and other neurodegenerative diseases is of great benefit to accelerate the developing of nanomedicines in ALS therapy. In this review, the challenges of delivering ALS drugs to the CNS and the opportunities of nanotechnology to address these challenges are discussed. Additionally, the spectrum of the pathophysiology of ALS is revisited with a discussion of how nanomaterials may be designed to combat these pathophysiologies. Finally, challenges and perspectives for the development of ALS targeting nanomedicines are described.

2.1 Introduction

Amyotrophic lateral sclerosis (ALS), also known as motor neuron disease (MND) or Lou Gehrig's disease, is a rapidly progressive neurodegenerative disease that causes dysfunction of the nerves that control muscle movement [2]. According to statistics, the morbidity of ALS is around one to three people per 100,000 worldwide [3]. To date, there is no effective treatment for ALS, while the reported median life expectancy of ALS patients ranged from 24 to 48 months from the time of diagnosis. Nevertheless, some ALS patients can live for more than five years [3]. ALS mainly affects motor neurons in the brain (upper motor neurons), brainstem, and the spinal cord (lower motor neurons) (Fig 1A), leading to progressive motor neuron degradation and muscle atrophy, which ultimately results in paralysis and eventually death due to respiratory failure [1]. The causes of the ALS have proven to be extremely complicated and largely unclear, undoubtedly contributing to only few treatment options [3].

ALS can be categorized as familial (fALS) or sporadic (sALS), depending on whether or not the patient has a family history of the disease. fALS is generally considered to account for 5% to 20% of all cases of ALS [2]. More than 25 genes have been found associated with fALS, of which C9orf72 (40%), SOD1 (20%), FUS (1–5%), and TARDBP (1–5%) are the majority four genes account for most of the familial ALS cases [4]. The causes of neuron death are still unclear. The degenerative disorder of motor neurons is believed to be involved in many genetic, cellular, and molecular processes. Broadly, gene mutation, glutamate excitotoxicity, protein misfolding and aggregation, endoplasmic reticulum (ER) stress, neuroinflammation, oxidative stress, mitochondrial dysfunction, loss of trophic factors, cytoskeletal elements and axonal transport are some of the principal theories that have proposed in causing ALS [5] (Fig 1C). Many therapeutic strategies have been developed based on these mechanisms, disappointingly, to date, the U.S. Food and Drug Administration (FDA) has only

approved two drugs that slow ALS progression, albeit modestly: Riluzole and Edaravone [3]. Almost all other clinical trials have failed to display any improved clinical efficacy in the treatment of ALS over the last 20 years [6-7]. Insufficient understanding of the mechanism, inappropriate animal models, imperfect clinical trial design, lack of effective biomarkers, delayed diagnosis, insufficient bioavailability/bio-stability of drugs, and low efficiency of delivering ALS drugs to CNS are some of the potential reasons hindering significant translational progress in ALS clinical trials [6, [8]].

To address the above limitations in ALS treatment, new strategies are practically required. Encouragingly, the great achievements of nanotechnology-based approaches in treating neurodegenerative diseases (e.g. AD, PD) in the last few years have opened a gate for nano-based ALS treatment strategies. These include but are not limited to the features of improving drug bioavailability/biostability, overcoming biological barriers (BBB/BSCB), reducing side effects, targeting disease sites, and achieving real-time tracking [8-9]. In view of this, many drugs with poor clinical efficacy can be revitalized by nanotechnology. Therefore, systematically discussing how to resort to nanotechnology to improve the efficacy of drugs will greatly benefit the progress of ALS treatment. This review outlined the various challenges in delivering ALS drugs to CNS and how nanotechnology can be applied to address these challenges. ALS pathophysiology is also revisited together with an outline of how the nanomaterials have been designed or can be potentially utilized to combat the pathophysiology are further discussed. The remarkable outcomes from nanotechnology-based neurodegeneration disease treatment, providing us an optimistic attitude that one or more of the nanotechnology-based strategies will become available to benefit ALS patients living shortly.
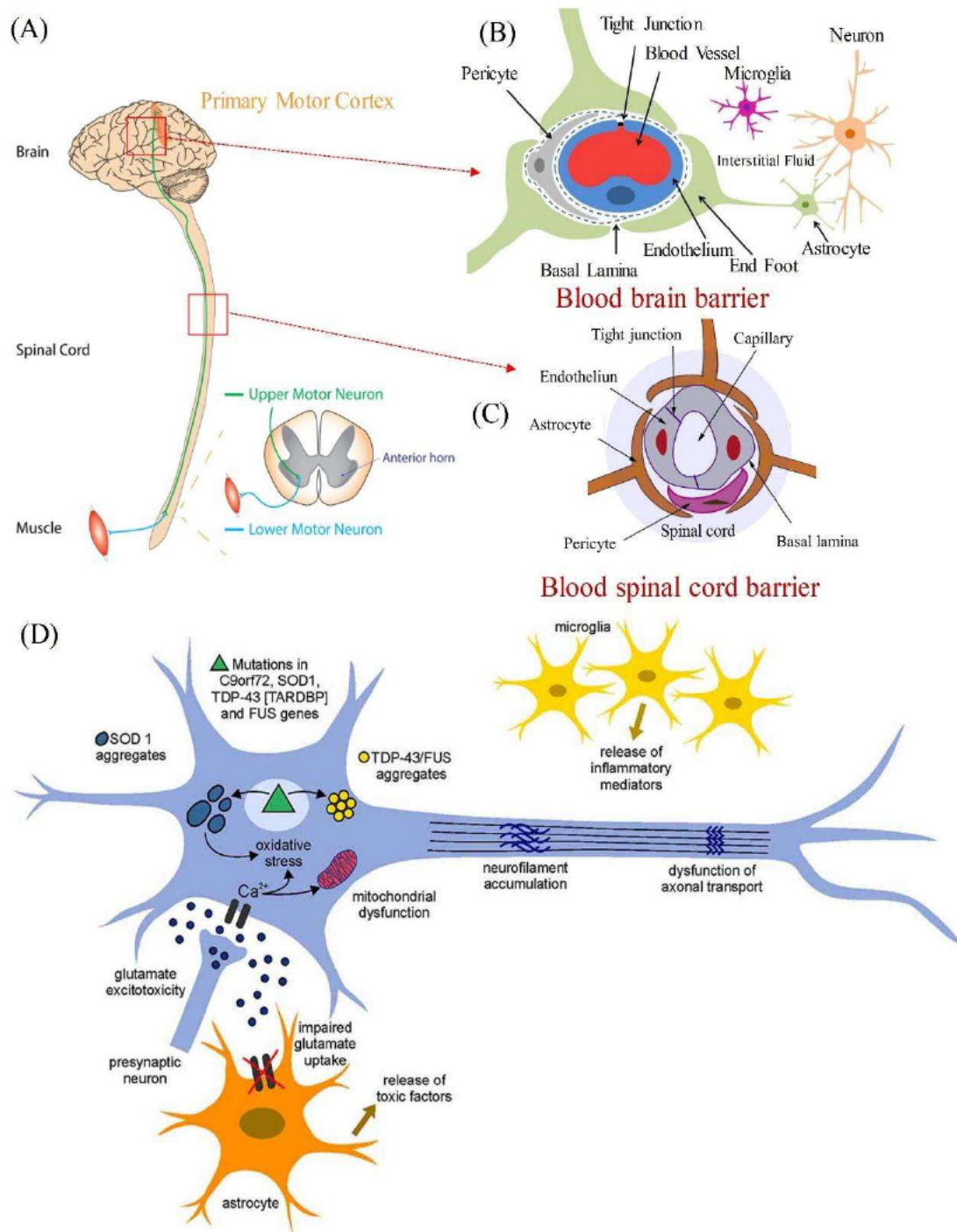
Figure 1 *(A) Nerves system involves typical ALS includes upper motor neurons (located in the brain) and lower motor neurons (located in the spinal cord and brainstem). The illustration of the structure of blood–brain barrier (BBB) (B) and blood–spinal cord barrier (BSCB) (C) that composed the blood–Central Nervous System barrier. (D)The proposed cellular and molecular mechanisms involved in ALS. Copyright with permission from ref 5.*

2.2 Proposed mechanisms of ALS

Although the precise mechanisms of ALS are still poorly understood, its believed that ALS is mediated by a complex interaction between cellular, molecular, and genetic pathways. To our best knowledge and literature report, the principal proposed disease mechanisms contributing to ALS are listed in the following. (1) Gene mutation; Genes are known to be involved in ALS mainly affect their normal functions like protein production, RNA processing and cellular metabolism. So far, more than 25 genes have been identified to ALS, and C9orf72, SOD1, FUS, and TARDBP contributed to most family ALS cases [10]. (2) Protein misfolding and aggregation; Several essential RNA-binding proteins in ALS, such as TDP-43, FUS, ATXN2, hnRNPA1/A2, may undergo cytosolic accumulation and nuclear depletion, thereby causing protein misfolding and aggregation. The most common case is TDP-43 aggregation, which is found in more than 95% of ALS patients (both sporadic and familial) [11-12]. (3) Glutamate Excitotoxicity; Neuron cell death caused by high levels of intracellular calcium is widely believed to be linked with excessive stimulation by the increased synaptic glutamate levels [13]. (4) Oxidative stress; The higher production rate of free radicals or reactive oxygen species (ROS) than the ability of neurons to remove them will lead to the excessive oxidative stress, resulting in irreversible damage to the cell structures and their normal functions as excessive oxidative stress are well known to cause damage to cellular proteins, DNA and RNA. In most ALS cases, the patients are diagnosed with increased levels of oxidative damage in the serum, urine samples, or cerebrospinal fluid (CSF) [14]. (5) Mitochondrial dysfunction; Mitochondria are vital organelles for a variety of cellular functions, such as energy metabolism, phospholipid biogenesis, apoptosis, and calcium homeostasis. Mitochondrial dysfunction has been extensively found in ALS animal models and patients that have been recognized directly attribute to disease pathogenesis [14]. (6) Neuroinflammation; ALS is not considered as autoimmunity disease, acute neuroinflammation may benefit the function of motor neurons while chronic

inflammation may lead to motor neurons degeneration, meanwhile, plenty of anti- and proinflammatory growth factors and cytokines have been found involved in pathological changes that linked to ALS [15-16]. (7) Cytoskeletal elements and axonal transport; Increasing evidence has point out the abnormal accumulation of neurofilaments (NFs) and mislocation of phosphorylated NFs in motor neuron cell bodies or axons attributed a crucial pathological of ALS. Current therapeutic strategies based on the above mechanisms have shown great progress, such as genomic and proteomic therapy, that may help to halt or reverse the progression of the disease [17]. However, there are still several critical challenges for delivering ALS therapeutic drugs to CNS and will be discussed in detail in the next section. Furthermore, the current progress in nanotechnology mediated ALS or other neurodegeneration disease therapy based on the above mechanisms are further discussed in section 4.

2.3 Current treatment and clinical trials for ALS

Until now, the US Food and Drug Administration (FDA) has approved only two drugs for the treatment of ALS: Riluzole and Edavarone. Riluzole was first approved by the FDA in 1995, and in the ensuing decades, many other countries, including Australia, Canada, and throughout Europe, also approved Riluzole as the first line drug for ALS[18]. It is thought that Riluzole can reduce the excitotoxicity of glutamate by preventing the release of glutamate, as excessive glutamate accumulation in the brain and spinal cord is one of the main features of ALS[19]. Edavarone received FDA approval in 2017 and Health Canada approval in 2018[20]. Edavarone treatments are also available in Japan and South Korea. Edavarone acts as an effective ROS scavenger (for example, oxygen radicals) in the central nervous system, and excess ROS is considered a major mechanism for inducing neuronal death[20]. Although these two treatments have slowed down the symptoms to some extent, the treatment effect is still very limited[21]. Currently, more drugs and treatments have been used in clinical trials (Table 1)[22]. In the

near future, more drugs may be available to treat ALS patients. However, given the extremely complicated causes for ALS, drugs targeting a single mechanism may not produce significant therapeutic effects, a combination of drugs may lead to better clinical outcomes. In addition, given the existence of biological barriers (e.g. BBB, BSCB) and inherent limitations of the drug (e.g. low solubility, easy degradation, biological toxicity, etc.), how to effectively transport therapeutic drugs to CNS is another major obstacle that slows the development of ALS drugs[23]. In the next section, we will discuss the challenges of delivering ALS therapeutic drugs to CNS.

Table 1. Ongoing Phase-III interventional trials on ALS

Compound	Target/mechanism	Recruiting	Identifier
Aroursodeoxycholic acid	Anti-apoptotic	Not yet	NCT03800524
Methylcobalamin	B12 vitamin derivative	Yes	NCT03548311
Masitinib	Tyrosine kinase c-Kit inhibitor	Not yet	NCT03127267
CannTrust CBD Oil	Active cannabinoid	Yes	NCT03690791
Arimoclomol	Stimulates repair pathways	Yes	NCT03491462
Levosimendan	Calcium channel sensitizer	Yes	NCT03505021
Deferiprone	Iron chelator	Not yet	NCT03293069
MSC-NTF cells	Mesenchymal cell therapy	Yes	NCT03280056

Search query: ALS (Amyotrophic Lateral Sclerosis) https://clinicaltrials.gov/ Filtered for: tatus: Recruiting − Not yet recruiting − Active, not recruiting − Enrolling by invitation;Study type: Interventional (Clinical Trial); Study Phase: Phase-III.

2.4 Challenges of delivering ALS therapeutic drugs to CNS

Although plenty of newly developed therapeutic agents (e.g. therapeutic proteins, neurotrophic factors, antisense oligonucleotides) have been synthesized to combat ALS, the therapeutic efficiency of those drugs have been rendered insufficient by their unsatisfactory *in vivo* properties, such as low stability in biological environments, poor permeability to cross BBB, rapid enzymatic degradation, immune system clearance, unfavorable pharmacokinetic properties, and inappropriate release profiles [24]. Any one of these limitations may explain why a particular therapeutic agent fails to effectively target CNS and achieve clinical

efficacy. The major challenges of delivering ALS therapeutic drugs to CNS is described in the following section.

2.4.1 Blood-brain barrier

The blood-brain barrier (BBB) (Fig 1B) is one of the most critical protection mechanisms in the central nervous system (CNS). The BBB only selectively allows individual substances such as nutrients and small lipid-soluble molecules to pass through the brain capillary endothelial membrane while limiting the entrance of pathogens or toxins [25] (Fig 2A). However, this protection mechanism is also a major barrier for delivering ALS therapeutic drugs to the brain, which hinders more than 90 percent of small-molecule drugs and nearly all biologics (e.g. siRNA, DNA, AOS) [24]. Moreover, the BBB not only controls blood-to-brain influx of nutrients but also controls brain-to-blood or CSF-to-blood excretion of drugs and endogenous compounds through efflux transporters[26] (Fig 2A). For example, P-glycoprotein (P-gp), one the most widely studied multidrug resistance proteins, plays as the primary efflux transporter of many endogenous substrates and unwanted molecules, including a large number of lipid-soluble drugs. The activity of P-gp constitutes a major cause for the failure of many potential ALS therapeutics to effectively penetrate the BBB and reach therapeutic concentrations in the CNS[27]. Additionally, various metabolizing and degrading enzymes (e.g. phase I and phase II enzymes) have been found distributed at the membrane of brain capillary endothelial cells, accompanied by a large number of transporter proteins that strictly regulate the passage of therapeutic substances to brain. Many drug candidates that might otherwise penetrate BBB are blocked by these barriers[28]. Collectively, these features impose major obstacles to the successful delivery of drugs into the brain.

2.4.2 Biostability and Bioavailability

Insufficient biostability and bioavailability are other problems that persist aside BBB-permeability. In particular, approximately half new developed chemical therapeutics in the pharmaceutical industry has shown extremely low solubility in water, which is an acknowledged problem in the development of new ALS therapeutic drugs[29]. To date, most clinical used drugs for CNS disease are small (<400 Da), lipid-soluble molecules that can cross the BBB by active transmembrane diffusion. However, the drug absorbed by the brain capillary endothelial cells must then be delivered to the interstitial fluid of the brain tissue to play function. Consequently, a drug molecule that is too lipid soluble risks sequestration by stacking at the capillary bed and may not reach the cells behind the BBB. In addition, the high lipid solubility of drugs may also lead to non-selective uptake by other peripheral tissue, thus lowering drug concentration in the blood. Therefore, it's crucial to design the drugs with appropriate lipid solubility to guarantee the sufficient drug accumulation that presented in the CNS [30]. Recently, newer generations of biological therapeutics (e.g. nucleic acid constructs, neurotrophic factors and therapeutic proteins) have shown promising efficiency in treating ALS[21], take SOD1 shRNA, for instance, using an adeno-associated virus serotype 9 (AAV9) vehicle to deliver an shRNA to reduce the synthesis of ALS-causing human SOD1 mutants has demonstrated extended survival in SOD1G93A mice by delaying both disease onset and slowing down disease progression[31]. However, these biomolecules are not BBB permeable and are more susceptible to the influence of biological enzymes, as evidenced by their extremely short lifetime[32]. These have seriously hampered the effectiveness of ALS drugs in the CNS.

2.4.3 Systemic distribution and clearance

Another major obstacle for drug delivery to CNS is its systemic distribution that attenuates the "on-target" effect of drugs. As discussed in section 2.2, many lipid drugs may passively diffuse into the central nervous system, these lipophilic

therapeutics also more readily absorbed by cells in all other tissues after intravenous injection[33], as a result, a larger drug dose must be given to achieve the required therapeutic concentration in the brain. This non-specific systemic distribution may lead to increased systemic toxicity and affect patients' quality of life[34] [35]. In addition to systemic distribution, the rapid systemic clearance of many drugs also significantly affects the blood drug concentration. For example, in terms of oral dosages (e.g. Tiglutik (riluzole oral suspension)), due to the enzymatic and nonenzymatic degradation in the gastrointestinal (GI) tract, these drugs may have insufficient systemic bioavailability after oral administration before the drug reaches the systemic circulation [36]. While intravenous administration circumvents these problems, the major problem is that hydrophilic drug molecules may typically suffer rapid renal clearance on account of poor reabsorption after glomerular filtration, whereas lipophilic drugs are often converted into hydrophilic metabolites in the liver before renal or biliary excretion[33]. Therefore, it was deduced that the lacking therapeutic efficacy of administrated riluzole or edaravone might due to their systemic distribution and fast systemic clearance[37].

2.5 Opportunities of nanotechnology to mediate CNS drug delivery in ALS

In the past few decades, several nanomedicines have been approved by the FDA and have shown far greater therapeutic efficacy than drugs alone, such as Genexol-PM, Abraxane, Kadcyla, that gives us an optimistic attitude to develop ALS nanomedicines[38]. For CNS drug delivery, nanocarriers confer great opportunities to effectively package and protect the therapeutic agents and subsequently transport enough drugs across the BBB while avoiding extensive systemic distribution [9]. In the following section, we describe the opportunities of nanotechnology to mediate CNS drug delivery in ALS.

2.5.1 Overcoming the BBB/BSCB

Recently, great progress has achieved to deliver drugs or diagnostic agents into the brain or spinal cord using nanotechnology. Many features can affect the efficiency of NPs pass through BBB/BSCB, in particular, their inherent properties such as nanoparticle types, size and surface charge, and their surface functionalization are among those features that have been extensively reviewed by Saraiva et. al[39] and shown in Fig 2B. Different pathway of nanomaterials crossing BBB is described in Fig 2C, particularly, nanoparticles can cross BBB by absorptive-mediated transport (AMT), receptor-mediated transport (RMT) and cell-mediated transport (CMT), among them RMT is the away been most widely studied and applied[23]. Different nanostructures that can be used for BBB penetration are shown in Fig 2D. for example, several lipid NPs based nanomedicines have been approved by FDA and showed the promising capability for brain drug delivery, Poly(amidoamine) dendrimers (PAMAM) have been recognized as one of the most versatile nanoparticles that can be utilized for drug/gene delivery[39]. To facilitate their capability of crossing BBB, nanoparticles are usually engineered with various ligands (Fig 2B), for example, the ligands that capable of adsorbing brain penetrating proteins (e.g. tween 80), the ligands that capable of interacting directly with the brain endothelial cell receptors (e.g. transferrin, brain-specific antibody and peptides) and the ligands that able to increase endothelial cell endocytosis (e.g. cationic polymer, amphipathic peptides). Besides, the ligands that capable of improving blood circulation (e.g. poly (ethylene glycol) (PEG), cell membrane) are also widely used in arming nanomaterials[39]. Moreover, the capability of nanoparticles to cross the BBB can be enhanced by utilizing a combination of techniques that manipulate the BBB. The BBB can be temporarily forced open with certain drugs or physical stimulation that allows nanoparticles to penetrate between the opened tight junction (TJ)[23]. Furthermore, nanoparticle delivery of therapeutic agents can also be enhanced by the co-administration of inhibitors of efflux pumps or employing polymeric P-gp inhibitors as carrier's composition [40].
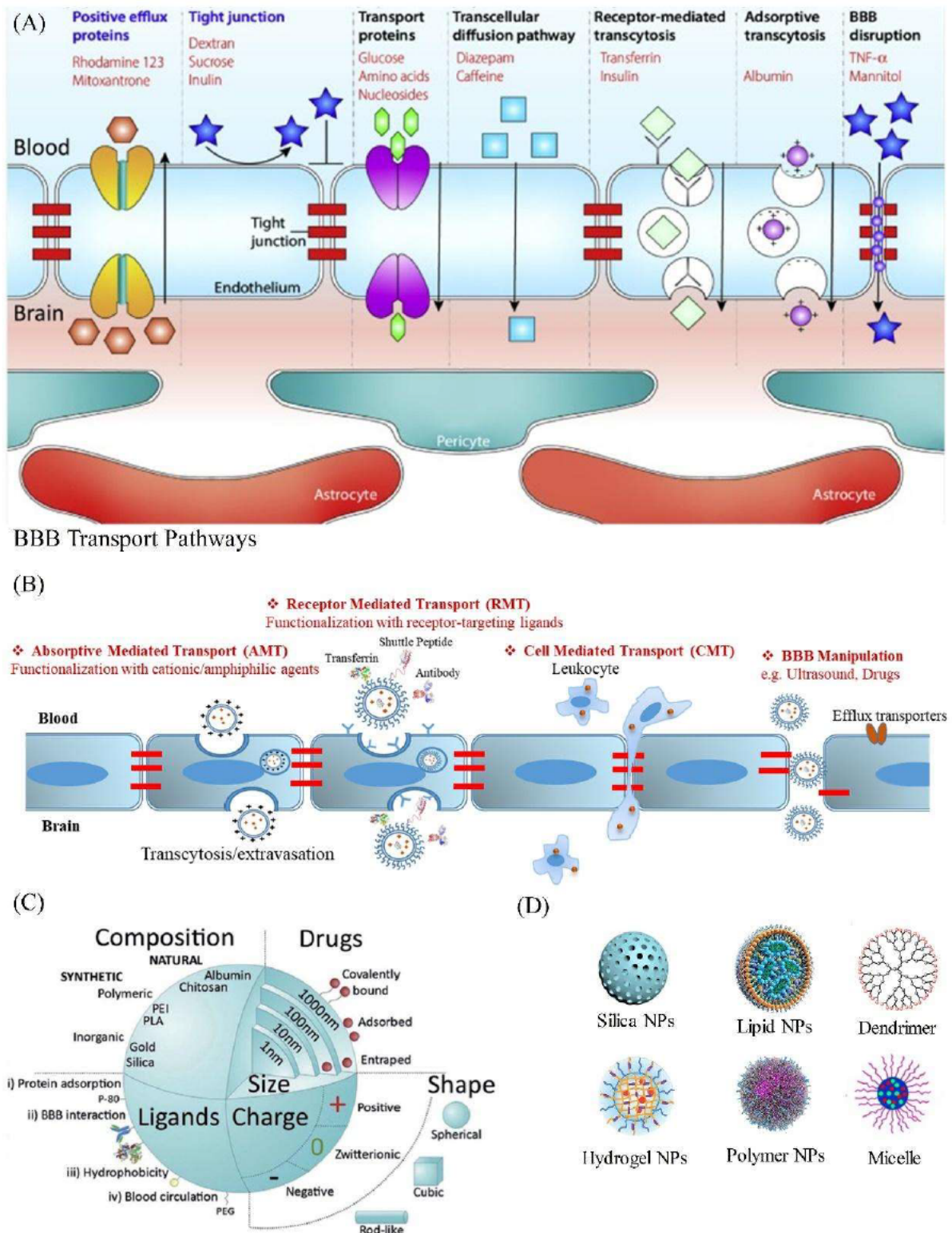
BBB Transport Pathways

Figure 2 (A) Typical blood-brain barrier transport pathways for substances pass through the BBB. (B) Typical non-invasive nanotechnology-based CNS drug-delivery strategies crossing BBB. (C) The major NPs features involve in the

permeability of BBB and systemic delivery. Copyright with permission from ref. 25,39.

2.5.2 Improving bioavailability and increasing drug exposure time in the body

Many of the newly discovered drug molecules are insoluble in water and must be used with additional additives, such as surfactants, oils, ethanol, that normally cause inconvenience administration or side effects [21]. SP600125 (an anthrapyrazolone inhibitor of JNK), take in an instance, can be used for stabilization of STMN2 in ALS therapy, but SP600125 is poorly soluble in water, DMSO is normally needed for experimental requirement, which significantly hinders its application in the clinical trial[41]. By using nanotechnology, these hydrophobic drugs can be encapsulated inside or conjugated to their surface, resulting in increased dissolution rate and solubility[42, 43]. Another problem that hinders the application of many drugs in CNS is the short half-life due to rapid systemic excretion or enzymatic degradation. The half-life of edaravone, for example, is only 4.5 to 6 h while the half-life of nucleic acid constructs is even shorter (serval min), thus higher doses and frequent drugs use have to be adopted for chronic lifelong treatment leading to declined quality of life and increased risk of side effects[44]. The last few years have seen the rapid development of nanotechnology, the drugs encapsulated in nanocarriers have been successfully applied to various diseases with prolonged drug retention time during blood circulation [32]. Firstly, drug encapsulated in nanoparticles can reduce renal clearance due to increased size, as renal clearance is prevented once size <15 nm[45]. Secondly, nanoparticle formulation may also protect drugs from metabolizing by enzymes in the liver and other metabolizing tissues by their physical barrier[46]. Thirdly, the controlled release manner of drugs from nanocarriers makes it possible to maintain an effective blood drug concentration for a long time. Finally, through the surface coating with extracted cell-membrane, natural polysaccharides, stealth peptides et al. [47], those emerged stealth

nanocarriers may protect the drugs been cleared by the immune system, thus extending the drug expose time in the body.

2.5.3 Targeting drugs to specific locations

Wide systemic distribution of therapeutics can lead to insufficient accumulation in disease regions[24]. Better, tightly focused, drug delivery is needed to improve the development of therapeutics for ALS. For instance, nano-vehicles capable of selectively targeting neurons or axons should have significant application in ALS, as these would allow specific visualization of peripheral axonal and neuronal compartments, which could be highly useful as a diagnostic[48]. Additionally, neuron or axon targeting nanocarriers could also deliver therapeutics directly to injury sites. Exploiting the presence of GM1, GD1a, GD1b, and GT1b [49](the most abundant gangliosides in the neuronal and axonal compartments of mammalian nerves) may provide a means to achieve specific targeting. These moieties localize in the outer leaflet of plasma membranes. The head-groups of these gangliosides are accessible to lectins present in bacterial toxins or antibodies[50]. Thus it may be possible that bacterial toxins or antibodies can be engineered onto the nano-vector surface to facilitate specific delivery of therapeutic agents to peripheral neurons or axons. An alternative approach is to use an *in vivo* phage-display screen, to identify a axonal import targeting peptide (TAxI), that delivered protein cargo into spinal cord motor neurons after intramuscular injection[51]. These examples and potentially others, illustrate the opportunity for arming nanomaterials to selectively deliver ALS therapeutics to injury sites. Alternatively, stimuli-responsive nanocarriers by using ultrasound, pH, ROS, enzymes, light et al. [52-54], also presented the ability to control the release behaviour of drugs, which can potentially enhance the targeting and the control of dosage. In particular, triggering drug release by a ROS responsive manner has shown great advantage to others in treating neurodegeneration diseases since oxidative stress has been implicated in most of the disease cases.

The restrained drug release in normal cells largely reduce the risk of side effects on normal tissues/organs after long-term use of therapeutic drugs [55].

2.5.4 Real-time tracking and imaging

In the drug development process, it is crucial to evaluate whether a drug agent has reached the desired target. However, most drugs lack an intrinsic trackable signal and attempting to conjugate a fluorophore will likely change their pharmacological properties. Thus, nanotechnology confers an opportunity to incorporate sensitive, selective and rapid real-time tracking and imaging functionality. For example, magnetic NPs (MNPs) with intrinsic magnetic properties are positioned as the most promising nanomaterial for use as contrast agents for magnetic resonance imaging (MRI)[56]. Quantum dot (QDs) nanoparticles with unique optical, excitation/emission and photostable properties imbue them with several advantages over use of chemical fluorophores in bio-imaging[57]. Polymer NPs or solid lipid NPs can also be functionalized with a wide variety of biomolecules with unique chemistries to also enable drug detection of its *in vitro* and *in vivo* bio-distribution[58]. Other nanomaterials, such as intrinsic fluorescent dendrimer[58], upconversion nanoparticles (UCNPs)[59], and gold nanoparticles, with unique optical and physical properties are also showing excellent capability for real-time tracking or imaging. A practical example was shown in Fig 3, Linying and his co-workers discovered a tri-responsive polymer–gold nanoparticle that can co-deliver gene (siRNA) and therapeutic drug (Curcumin) for Parkinson's disease (PD) treatment[60], meanwhile, an aggregated Au cluster in specific diseased cells (PD dopaminergic neurons) allows for accurate imaging of PD via enhanced computed tomography (CT)[60]. Similarly, nanotechnology could also provide the opportunity for accurate ALS imaging and precise drug delivery.
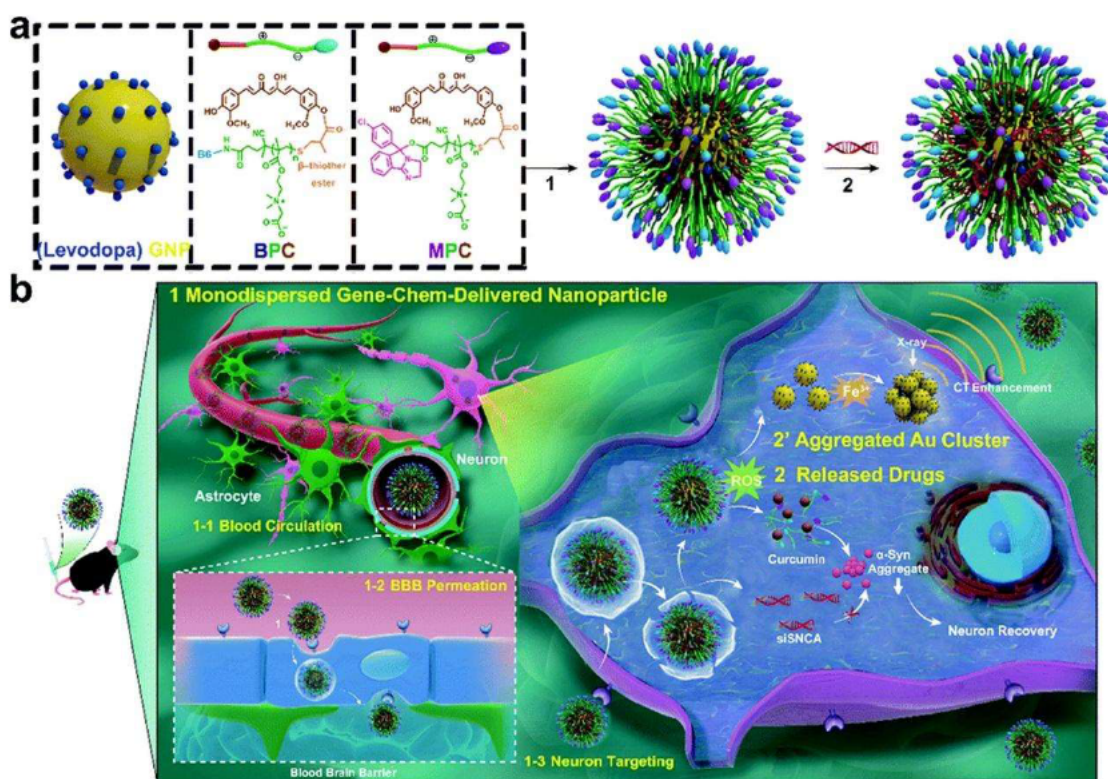
Fig 3 Schematic illustration of the formation of MBPCS nanoparticle and their switchable assembly diagram in vivo. a) Assembly of levodopa-quinone gold nanoparticles (GNP) and pro-drugs BPC and MPC to form MBPCS and their procedure to load siRNA. b) Switchable assembly of GNP in vivo. 1-1 The drug-gene co-delivery MBPCS circulation in the blood; 1-2 MBPCS could penetrate BBB via B6 peptide-mediated transport; 1-3 Neuron targeting via Mazindol (MA); 2 Release drugs by the ROS controlled manner; 2' Aggregated Au cluster for imaging via enhance computed tomography (CT). Copyright with permission from ref. 60.

2.6 Designing new therapeutic nanomaterials specifically targeting ALS pathophysiology

The effective delivery of therapeutic drugs, trophic factors and biomacromolecules across the BBB/BSCB to CNS remains a challenge for ALS treatment[8]. As discussed in section 3, the rapid development of nanotechnologies has made them capable of solving one or more factors that limit the treatment of ALS. In this part, various aspects of ALS pathophysiology are revisited and how

the nanomaterials have been designed or can be potentially utilized to combat the pathophysiology are discussed, thus providing the basis to accelerate the transformation of nanomedicine from theory to ALS clinical trials.

2.6.1 Glutamate Excitotoxicity

Glutamate works as a primary excitatory neurotransmitter in the CNS. Excess glutamate can lead to over-stimulation of the NMDA receptors (glutamate and ion channel protein receptor) and subsequently induce glutamate excitotoxicity[61]. Increasing evidence has pointed out that glutamate excitotoxicity plays an important role in the progress of ALS and more than 40 percent of sALS have been characterized with glutamate dysfunction [61, 62]. Riluzole is the first FDA approved drug for ALS quite well-known as an attenuator to glutamate excitotoxicity by blocking the release of glutamate. But its low aqueous solubility, short half-life (9-15 h after repeated doses), insufficient cerebral accumulation, and some side-effects at higher dosage are the major limitations that hinder its clinical application[63]. In the last few years, scientists have engaged in developing diverse nano-formulations to enhance its neuroprotective power of Riluzole against various neurodegeneration diseases. For example, Sa Bondì and his co-workers have produced riluzole loaded solid lipid nanoparticles (SLNs). The SLNs were able to successfully deliver riluzole into the brain (1.3 times higher than free drug after 8h I.V.). Moreover, a low drug distribution presented in liver, spleen, kidneys, heart, and lungs were found for riluzole-loaded SLNs when compared to free drugs, which has shown potential benefits in reducing side effects to those organs[64]. In addition to use drug to control the glutamate release, re-establishing glutamatergic homeostasis through up-regulating the expression of GLT1 (EAAT2) has demonstrated great progress in animal models and shown to be a promising way to remedy the damaged glutamate neurochemistry[65]. However, the unfavourable pharmacokinetic properties, such as poor water solubility, low oral bioavailability, as well as severe peripheral adverse effects

may lead to failure of some preclinical GLT1 (EAAT2) regulators (e.g. ceftriaxone) in achieving clinical efficiency [65] [66]. Recent advances by using nano-based drug delivery systems have demonstrated the possibility of encapsulating those GLT1 (EAAT2) upregulators in nanostructures (e.g. liposome, polymer nanoparticles, nano-micelle) to address the above pharmacokinetic issues. Further functionalization of the drug loaded nanocomplexes with brain target agents will facilitate the transportation of those nanocomplexes across BBB to CNS (Fig 4). The released drug from nanocarriers is expected to exert an effect in astrocytes to up-regulate the GLT1 expression. Subsequently, the glutamate excitotoxicity to neurons can be reduced by increasing glutamate uptake in astrocytes (Fig 4). Other drugs towards control of glutamate levels in ALS are also under active investigation (e.g. AMPA, Gacyclidine, Valproic acid). Those drugs can also be packaged as CNS targeted nanomaterials for optimal therapeutic effect[65].
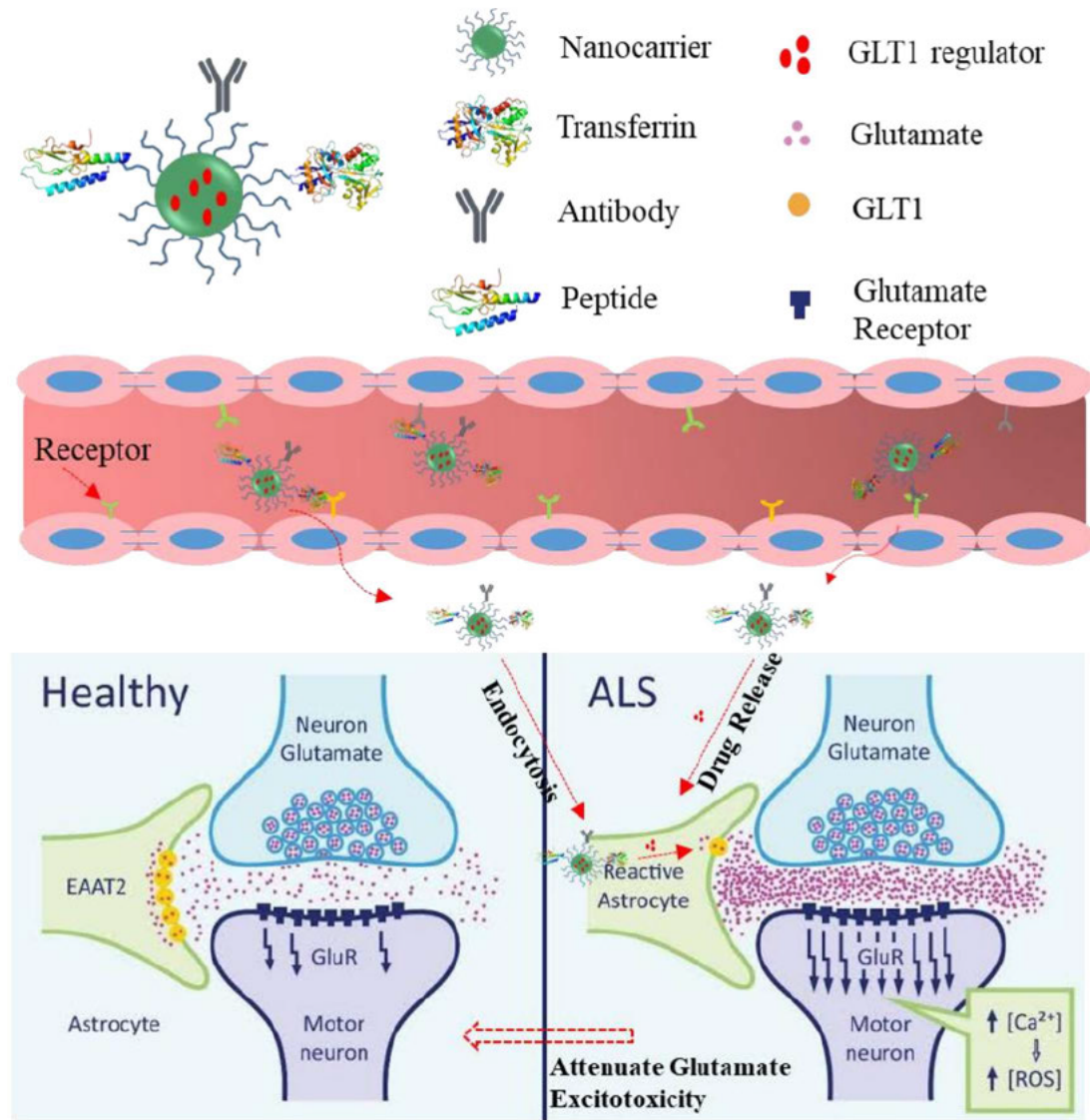
Figure 4. Schematic illustration of GLT1 (EAAT2) regulator loaded nanoparticles across BBB and regulate the GLT1 expression.

2.6.2 Oxidative Stress

The excessive production of ROS combined with lacking oxidant eliminating mechanisms has been recognized as the major pathogenesis of ALS[62]. The second FDA approved ALS treatment Edaravone (EDV) is a drug well known for its antioxidant function. It protects nerve cells by clearing damaging reactive oxygen species (ROS) in the body[20]. To improve the therapeutic efficiency of EDV in ALS, several nanostructures have been developed to better deliver EDV to the brain, such as agonistic micelles and solid lipid nanoparticles[67, 68].

Additionally, the combined administration of EDV and BBB interferers have demonstrated great efficiency for delivering EDV to the brain. For example, in a study conducted by Qu et al., EDV was encapsulated into the inner hydrophobic core of the agonistic micelle (EDV-AM) while the outer hydrophilic shell was conjugated with A2AR agonistic agents (signaling adenosine 2A receptor), the specific delivery of EDV into brain ischemia was facilitated by temporary trigger TJ opening with EDV-AM-A2AR signaling [67] (Fig 5A), after that EDV was released from intracerebral EDV-AM that can efficiently eradicate ROS produced by diseased brain cells. Meanwhile, the side effects involved in irreversible BBB damage was significantly minimized with the rapid restoration of the TJs. In addition to medication options, various metal oxide nanoparticles were also shown to be effective in eliminating ROS, such as Fe_3O_4 NPs, CuFe-PB-like NPs, CeO_2 NPs[69, 70]. Their function as free radical scavengers are mainly arising from non-stoichiometric crystal defects and oxygen deficiencies. CeO_2 NPs, for instance, with antioxidant properties has shown efficiency in ameliorating muscle strength and prolonging life in an ALS mouse model, as seen, the CeO_2 NPs treatment has prolonged median survival after onset in ALS mice from 22.0 ± 2.5 days (only treated with vehicle) to 33.0 ± 3.7 days[71]. However, the presence of the BBB dramatically hinders the accumulation of therapeutic nanoparticles in brain. Herein, the functionalization of those metal oxide nanoparticles with BBB penetrating agents (e.g. peptide, antibody, transferrin) is essential for exerting their highly effective in neuroprotection. Indeed, an effective stroke therapeutic strategy has been developed by Bao and his coworkers by engaging monodisperse ceria nanoparticles (CeO_2 NPs) and BBB penetrating agents[72]. As shown in Fig 5B, the surface of CeO_2 NPs was functionalized with Angiopep-2 and poly (ethylene glycol) to facilitate the BBB penetration and system circulation, meanwhile, the Edaravone was loaded by surface adsorption. Selective accumulation of CeO_2 NPs in brain tissues was demonstrated by receptor-mediated transport, and the elimination of ROS was achieved by synergistic of

the loaded edaravone and ceria nanoparticles[72]. It's worth noting that the safety and approaches for better treatment strategy of these metal nanoparticles in ALS animal models require further investigation.

2.6.3 Inflammation

Current research and clinical discoveries have shown that inflammation in the CNS is a key factor in ALS[73]. Increasing evidence suggests that the abnormal immune/inflammatory activity of non-neuronal cells, such as microglia and astrocytes, plays a crucial role in the disease onset and progression rather than autoimmune. A transient neuroinflammation response may benefit the survival of motor neurons while chronically activated astrocytes and microglia, accompany by infiltrating immune cells were proposed to attribute the principle pathological in ALS patients and ALS animal models. Besides, a large number of anti- and proinflammatory growth factors and cytokines (e.g. IFN-γ, IL-6, VEGF, TNF-α, IL-1β, and IL-10) were found involved in pathological changes that linked to ALS[74]. Thereby, targeting inflammatory mediators with anti-inflammatory therapeutic agents may thus be of potential benefit for neuroprotection in ALS, and indeed several clinical drugs like thalidomide, celecoxib, and minocycline have demonstrated efficiency in halting or delaying disease progress in ALS animal models[21, 75, 76]. However, clinical used anti-inflammatory drugs are often systemically administered at high doses to exert an effect, which would inevitably increase inflammation and cause cell toxicity. Therefore, it is crucial to find an effective and more compatible way for drug delivery. With the development of nanotechnology, biocompatible nanomaterials closely fulfill the above requirement with more safety and effective. A practical application of nanotechnology used for anti-inflammatory drug delivery was shown in Fig 5C, the anti-inflammatory drug arctigenin was loaded in a cluster-like mesoporous silica NPs (MSN) and surface functionalized with CAQK peptides to target brain injury and spinal cord injury (SCI) sites[74]. The smaller size of MSN-based drug

delivery system (<100 nm) enables the nanocomplexs passing through BBB and BSCB. Enhanced neurons protection and accelerated SCI recovery were demonstrated in an animal model through inhibiting the activation of astrocytes and diminishing the express of interleukin-17 (IL-17) and other inflammatory factors [74]. Similar to this design, deliver anti-inflammatory drug to ALS involved disease sites through nanotechnology may potentially benefit the patients by inhibiting neuroinflammation.
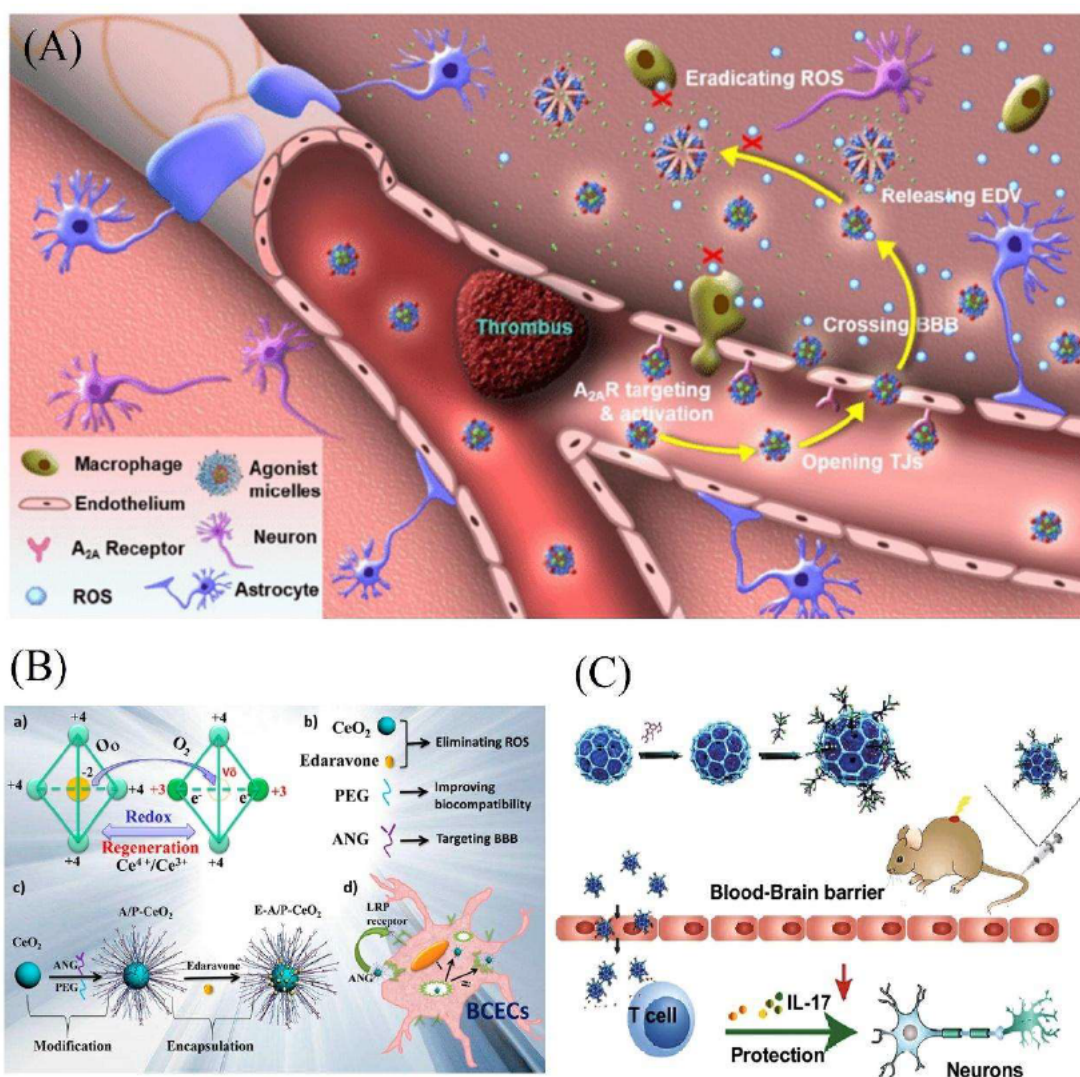

Figure 5, (A) Edaravone-Encapsulated Agonistic Micelles Enhanced the BBB penetration via temporary trigger TJ opening to rescue ischemic brain tissue. (B) Edaravone-Loaded Ceria Nanoparticles realize Blood−Brain Barrier penetrating and neuroprotection for Stroke Treatment. (C) Anti-inflammatory

agent loaded Silica-Based Drug Delivery System to specific target brain injury and SCI sites. Copyright with permission from ref. 67, 72, 74.

2.6.4 Transition-metal dyshomeostasis

A common pathophysiology that involves in many neurodegenerative diseases such as ALS is the excessive accumulation of the transition metals like copper ($Cu2+$) and iron ($Fe3+$) in the CNS[77]. Although iron doesn't directly induce diseases, it indeed plays a crucial role in promoting disease progression by catalyzing the formation of ROS and increasing oxidative stress. Thus, iron chelators (e.g. Deferiprone, Clioquinol, Apocynin) have shown therapeutic benefit in regulating transition-metal dyshomeostasis in many neurodegenerative diseases[78, 79]. However, those chelators normally host severe adverse effects and lack of tissue-specific targeting. Thus, incorporating chelators with nanotechnology may benefit their efficiency of passing BBB, increasing their selectivity in specific sites, facilitating their antioxidant capabilities[79]. Besides, some special inorganic nanostructures also show potential capability in metal-chelating that may beneficial for regulating transition-metal dyshomeostasis without the issue of drug loading and releasing. For example, black phosphorus (BP) nanosheets were designed as new chelating agents to capture excess redox-active Cu (Wansong Chen et al.)[80] . As seen in Fig 6A, it was shown that the BP nanosheets are not only effectively capture excess $Cu2+$ to protect neuronal cells from transition-metal dyshomeostasis induced neurotoxicity, but can also pass through the BBB under near-infrared laser irradiation via its inherent photothermal effect, which shows a great advantage to other conventional chelating substances. Additionally, the excellent bio-stability and biocompatibility warrant its safety for future clinical trials. More studies are needed to demonstrate their therapeutic efficiency in ALS animal models to further guide their application in ALS treatment.

2.6.5 Mitochondrial dysfunction

Mitochondrial plays an important role in cellular respiration, energy production, and calcium homeostasis. Mitochondrial dysfunction in neurons significant affects the normal cellular function and the neuronal cell death caused by the abnormal generation of ROS under mitochondrial dysfunction has been proposed as a major reason contributing to ALS [81]. As discussed above, various anti-oxidative agents and metal oxide nanoparticles were shown to be effective in combating oxidative stress[70]. Thereby, selectively deliver anti-oxidative drugs or therapeutic NPs to mitochondria might be a beneficial strategy for neurodegenerative disease therapy, including ALS[82]. Indeed, studies have shown that it is possible to selectively scavenge extracellular, intracellular, and mitochondrial ROS by applying different types of ceria nanoparticles (Fig 6B), Hyek Jin Kwon et al. have used those NPs for application in treating Parkinson disease (PD) [83, 84]. In another study, Bapurao et al. developed a biodegradable nanoparticle platform with high BBB penetration efficiency (~12%) and markedly brain astrocyte accumulation features that provid an alternative strategy to facilitate the neuroprotection processes by enhancing protection of astrocytes from mitochondrial dysfunctions and oxidative damage (Fig 6C)[85]. These preliminary suggest that it should be possible to design similar nanoparticles for ALS treatment. Additionally, increasing evidence has revealed that more than 50 mitochondrial proteins are up-regulated associated with the increased levels of SOD1 expression[86], thus, except scavenging ROS, nanotechnology based therapeutic approach towards to SOD1 also acts as a promising regulator for mitochondrial dysfunction. For example, SOD1 loaded PLGA NPs have been reported to confer human neuron protection by eliminating hydrogen peroxide-induced oxidative stress[85]. However, whether such nanoparticles offer a genuine therapeutic opportunity in ALS needs verification in follow-up studies.
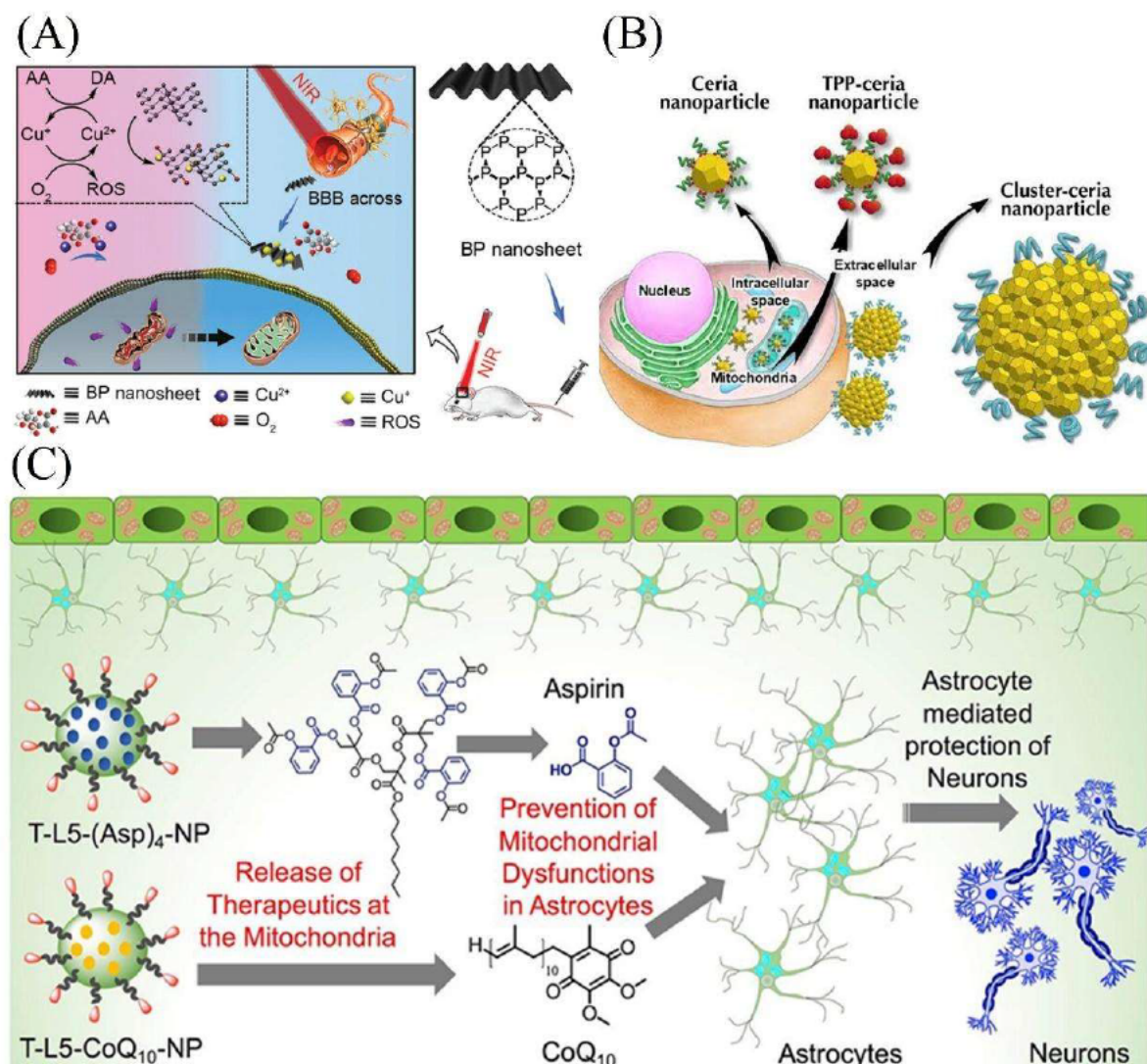
Figure 6. (A) The application of Black Phosphorus Nanosheets for Neurodegenerative Disorder Therapy. BP nanosheets cross BBB via near-infrared laser irradiation and protect neurons via selectively capture excess Cu2+ and application. (B) Different CeO2 nanostructures eradicate intracellular, extracellular, and mitochondria ROS, respectively. (C) Schematic illustration of T-L5-CoQ10-NP and T-L5-(Asp)4-NP target mitochondria of astrocytes that facilitates the neuroprotection processes by protecting astrocytes from mitochondrial dysfunctions and oxidative damage. T-L$_5$: TPP-(CH$_2$)$_5$-COOH. TPP: Tri-phenyl-phosphonium. Copyright with permission from ref. 80, 83, 85.

2.6.6 Protein misfolding and aggregation

Increasing evidence has demonstrated the crucial role of protein misfolding and aggregation in ALS affected neurons and glial cells, and the lack of clearance mechanisms has been recognized as one of the major pathogenesis in ALS[11, 87]. Protein misfolding results in the formation of protein aggregation and protein inclusions, thereby affecting their normal function in supporting neuron activity. Several proteins misfolding, such as TDP-43, SOD1, and Ubiquilin-2, are widely found in ALS patients[88]. Especially, the protein aggregation of RNA-binding protein TDP-43 in the brain and spinal cord neurons is found in nearly all ALS patients, and rare mutations in the gene encoding TDP-43 can cause ALS[89]. ASOs therapy has been shown the effect of substantially slow disease progression in a rat ALS model. However, SOD1 mutations only account for 2~5% of ALS cases[89]. Thereby, therapeutic targeting TDP-43 may benefit the majority of ALS patients. However, down regulate the expression of TDP-43 is not feasible, given its critical cellular function. Thus, more advanced strategies have emerged in a better way to combat TDP-43 aggregation. For example, in study conduct by Lindsay et al., the ataxin-2 targeted ASOs were administrated in CNS in TDP-43 transgenic mice, after a single treatment the pathology was largely reduced and the lifespan was markedly extended, which suggests that targeting ataxin-2 could represent an effective therapeutic strategy for broadly ALS patients[90]. More recently, in another study, post-translational stabilization of STMN2 by SP600125 (an anthrapyrazolone inhibitor of JNK) can rescue neurite outgrowth and axon regeneration deficits that induced by TDP-43 depletion and significantly improve the survival[41]. As nanotechnology has been widely used for gene and drug delivery and great progress has been achieved in CNS disease, using nano-vehicle to delivery those ASOs or inhibitor drugs to target TDP-43 aggregation may be a promising strategy for better therapeutic of ALS.

2.6.7 Gene Defects

In ALS, around 10% of cases have shown familial inheritance. By now, more than 25 genes have been identified to contribute ALS, which is estimated to be involved in 70% fALS and 15% sALS. Among them, SOD1, C9orf72, TARDBP, FUS are the major gene mutations associated with most of the fALS cases (>60%) and some sALS cases. Therapeutic approaches toward these mutations by RNA interference (RNAi) technology, antisense oligonucleotides or other nucleic acid substances have shown delayed disease progression in animals[91]. However, most studies have only focused on using virus vectors, such as adenovirus (AAV), herpesvirus (HSV), and lentivirus to deliver gene therapy substances to treat ALS[92-94], the immunogenicity and safety of these carriers are the major obstacles that hinder their further clinical applications[95]. The rapid development of nanotechnology in the recent decade has made it available to deliver novel DNA, antisense oligonucleotides (ASOs) and RNA for gene therapy, largely superseding viral vectors[96] with decreased immune response and flexibility design to overcome biological barriers[97]. For example, to deliver SOD1 ASOs to motor neurons, Chen et al. prepared calcium phosphate lipid-coated nanoparticles (CaP-lipid NPs) that could effectively and safely deliver SOD1 ASOs to motor neurons[98], meanwhile, the efficiency in a SOD1 mice model is undergoing. In another study, the therapeutic siRNA against the β-site amyloid precursor protein-cleaving enzyme 1 (BACE1) that for Alzheimer's disease (AD) therapy was prepared through the self-assembly process (Fig 7A)[99]. Under the aid of CGN and QSH peptide, the siRNA loaded nanocomplexes could actively cross BBB and accumulated in neurons near amyloid plaques. The single treatment has effectively reduced the expression BACE1 in protein and mRNA levels, and thereby reduced the production of Aβ production and the damage of neurons in the mouse model. This is a practical example that can be applied to delivery ALS related therapeutic genes passing through BBB and targeting specific sites. It is worth noting that despite these encouraging results, the reliability of

nanomaterials to transport genes and ASOs and the druggability of targets still needs to be further studied.

2.6.8 Neuroprotective and Neurotrophic Factors

Another potential treatment modality in ALS is increasing the expression of neurotrophic proteins or drug compounds that promote neuronal survival and regeneration or are neuroprotective. In the last few years, a large number of neurotrophic include BDNF, CNTF, GDNF, IGF-1, BMP-7, FGF; HGF, VEGF, and G-CSF[100] have been investigated in many of ALS models. It is perhaps not surprising that neuroprotective or neurotrophic therapeutics have recruited large patient populations in Phase 3 trials. However, these have largely failed to generate an effective therapeutic by short half-life and low BBB permeability[82, 83]. With the aid of nanotechnology, the biological stability, brain targeting, pharmacokinetic efficiency of neuroprotective and neurotrophic factors were greatly enhanced [101] [102]. A scheme of a practical approach to deliver neurotrophic to the brain was shown in Fig 7B. The nanocarriers are functionalized with efflux inhibitor and brain-specific antibody to enable the delivery of variety neuroprotectors across BBB by RMT[103]. The released neurotrophic in CNS enables to rejuvenate damaged neurons[103]. In the study conducted by Igor and his coworkers[104], for instance, PLGA nanoparticles were coated with poloxamer 188 (PX) to enable NPs across the BBB, the brain-derived neurotrophic factor (BDNF) was encapsulated in the NPs (NP-BDNF-PX), after intravenous (IV) injection in a mice model, a significantly higher level BDNF was detected in mice brain compared to control and the neuroprotective effect was also markedly improved. Thus, nanotechnology could be applied to improve the performance and efficacy of neuroprotective and neurotrophic factors for ALS treatment.
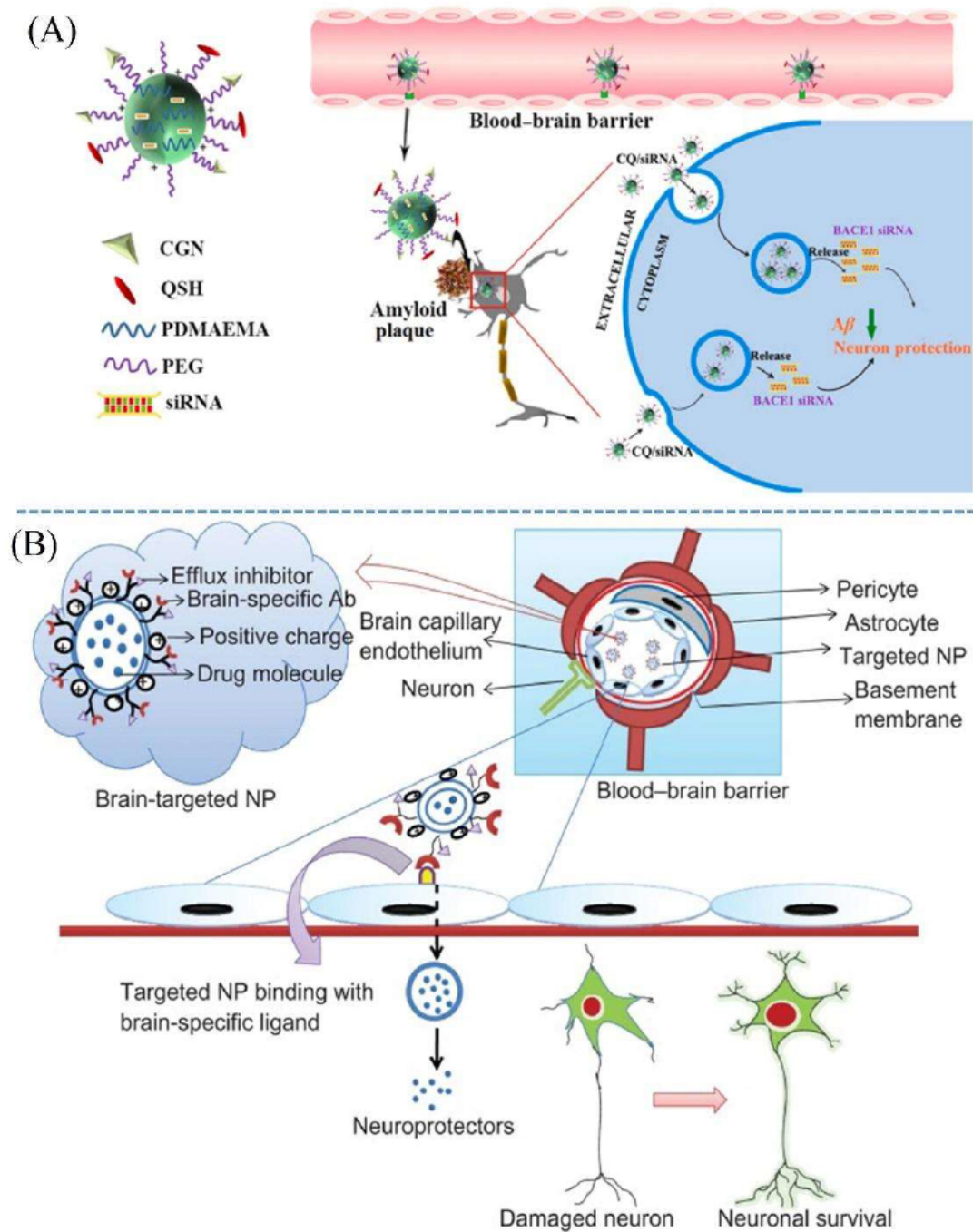
Figure 7 (A) Delivery small interfering RNA (siRNA) to the neurons via a polymer nanoparticles platform to improve the therapeutic efficiency of Alzheimer's disease. CGN: BBB targeting peptide; QSH: Aβ-targeting ligand. (B) Schematic illustration of preparation desire nanoparticles platform to deliver neuro-protect factors to the brain. The surface of NPs can be engineered with brain-specific antibodies, proteins, and efflux inhibitors that facilitate NPs penetration. Copyright with permission from ref. 99, 103.

2.7 Other emerging nanotechnologies for potential ALS drug delivery

With the rapid development of nanotechnology, more and more new approaches have been applied to the problem of penetrating the blood-brain barrier to better increase the therapeutic index of a variety of therapeutics. In this section, we will list several emerging nanotechnologies that boost nanocarriers crossing the BBB and discuss their potential applications in ALS drug delivery.

2.7.1 Glucosylated nanocarrier

Glucose transporter-1 (GLUT1) expressed in BCECs (brain capillary endothelial cells) is at a much higher level compared to many other transporters and receptors. Recently, researchers have exploited that a large number GLUT1 expressed in BCECs immigrated from luminal to the abluminal plasma membrane after animal fasting, following a rapid glycaemic increase enables a boost delivery of nanocarriers across the BBB that mediated by GLUT1[105](Fig 8A). Additionally, an increased nanocarriers accumulation in neurons was also observed, accompany with the boost BBB penetration, glucosylated nanocarriers showed the potential for brain drug delivery to treat brain neuron involved disease include ALS.

2.7.2 Virus mimic nanomaterials

The human brain can be infected by various virus like HIV, rabies virus, and adenovirus. Virus mimic nanocarriers can be designed to keep the capability of viruses penetrating BBB while eliminating their infection activity. For example, Lee et al. have fabricated rabies virus- inspired silica- coated gold nanorods (AuNRs@SiO2) that host similar size, shape, and surface glycoprotein characteristics with rabies virus[106]. Although the surface of the AuNRs@SiO2 was only covered with RVG29 (peptide derived from the rabies virus glycoprotein), it still kept mimic *in vivo* behavior of the rabies virus that can bypass the blood–brain barrier and travel into the brain through the neuronal pathway [106] (Fig 8B). Meanwhile, the peptide coating also dramatically improved

the system's bio-stability and biocompatibility that guarantee the bio-safety for further clinical application. Therefore, the virus mimic nanomaterials have provided us a new thought to deliver drugs to CNS through the neuronal pathway, which may facilitate the drug's BBB penetration efficiency while ensuring safety.

2.7.3 Exosomes

Exosomes are intracellular membrane-based natural nanomaterials that have shown great advantages to other nanomaterials due to their non-immunogenic feature and their ability to deliver variety cargoes [107, 108]. For instance, Lydia et al. have reported that exosomes can deliver siRNA to the mice brain[109]. As shown in Fig 8C, to reduce immunogenicity, exosomes were extracted from self-derived dendritic cells (harvest bone marrow and stimulated with interleukins); To engage the targeting, the dendritic cells were engineered to express Lamp2b. The fabricated exosomes can deliver siRNA specifically to microglia, neurons, or oligodendrocytes in the mice brain that results in a specific gene knockdown[109]. In another study, exosomes were produced from human mesenchymal stem cells (MSCs) and activated with interferon gamma, after loading anti-inflammatory, neuroprotective RNA and protein molecules, those exosomes were intravenously administrated in an autoimmune encephalomyelitis (EAE) mouse model and demonstrated the great ability of slipping through the blood-spinal cord barrier and rejuvenating lost motor skills [110]. Moreover, the exosome delivery systems have shown great biological tolerance that enables them to be better investigated in clinical trials. Novel exosome nanotechnology, therefore, has the potential to deliver a wide range of therapeutics pass through the BBB to treat a variety of neurological diseases, including ALS[107]. With the coming out of more and more emerging nanotechnologies for CNS disease treatment, it is believed that there will be a great improvement in the efficiency of drug delivery to CNS for ALS treatment.
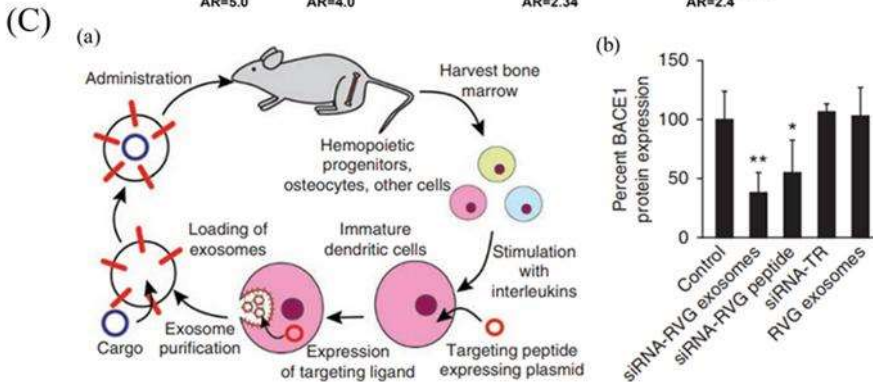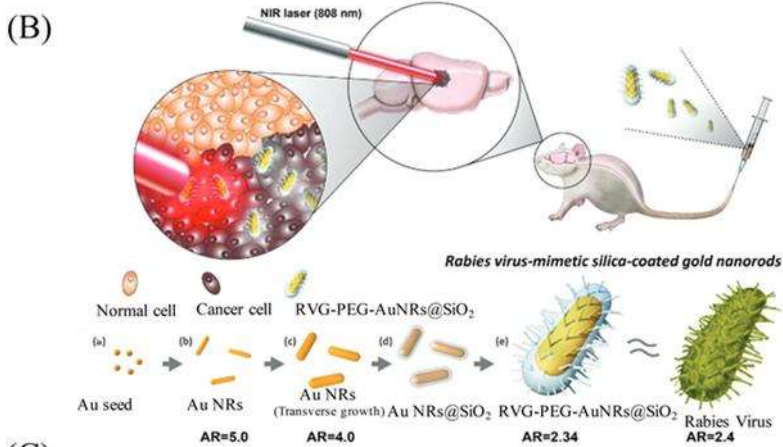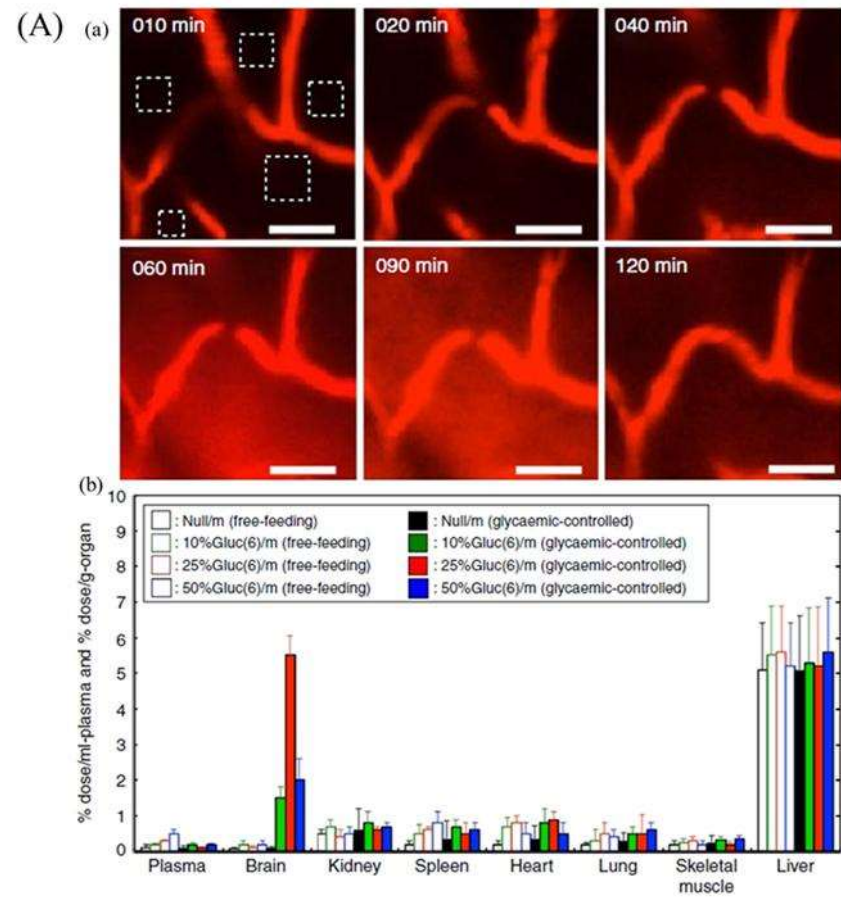
Figure 8. Other novel nanotechnologies with great potential for ALS drug/gene delivery (A) Glycaemic control increases the ability of glucosylated nanocarriers to cross the BBB into the brain. (a) Visualize the process of glycaemic controlled glucosylated nanocarriers cross the brain blood vessel; (b) Bio-distribution of different types of glucosylated nanocarriers in major organs. (B) Rabies virus mimic silica-coated gold nanorods bypass the blood–brain barrier (BBB) via neuronal pathways to treat brain disease. (C) Delivery of therapeutic siRNA to the mouse brain by systemic injection of targeting exosomes. (a) Schematic illustration of the preparation of targeting exosomes; (b) Gene silencing efficiency by different vehicles. Copyright with permission from ref. 105, 106, 109.

2.8 Conclusion and Perspectives

Scientists are exerting to unravel molecular, cellular, functions of the nervous system and identify genes and pathways that cause ALS, great progress resulted from the discoveries of new mechanisms, revealing the way for developing a potential therapy for ALS. However, there is still a long way for them from clinical use due to the lack of safe and effective delivery routes[111]. In the last few years, the rapid development of nanotechnology, opening the gate for a nano-based therapeutic strategy of ALS. The drug's properties like bioavailability, biostability, BBB penetration, neurons targeting et al., can be extremely enhanced by utilizing nanotechnology. Many therapeutic macromolecules, such as siRNA, ASOs, pDNA, their power to combat ALS can also be significantly improved by using nanocarriers. In addition, multifunctional methods of delivery and imaging technologies to evaluate whether drugs have reached the desired target will significantly benefit the field, and nanotechnology approaches warrant further investigation and investment. Moreover, nanotechnology also makes it possible to transport multiple therapeutic substances simultaneously (e.g. small molecules, genes, and therapeutic proteins) to exert more effective therapeutic outcomes[110,

[112]. Given the rapid growth of nanotechnologies, revolutionary tools will emerge, leading to new insights in ALS treatment and diagnosis.

In the last decades, nanosized biomaterials such as liposomes and polymers have been approved for clinical use[113]. However, newer classes of nanomaterials such as gold NPs, Qdots, and metallic nanoparticles are probably years away from reaching clinical trials. One of the key concerns to be addressed is that of nanomaterial biosafety, as the majority of work performed within the past decade has been focused on proof-of-principle demonstrations of nanomaterials for biomedical applications[114]. Additionally, the large-scale production of nano-drugs is another major obstacle to their clinical application[114, 115]. As this young, exciting, and rapidly developing field begins to mature in the next decade, we anticipate more effective transportation and targeting strategies will emerge, increasing the likelihood that nanotechnologies will contribute to ALS treatment.

Reference:

[1] M. Orsini, A.B. Oliveira, O.J. Nascimento, C.H.M. Reis, M.A.A. Leite, J.A. de Souza, C. Pupe, O.G. de Souza, V.H. Bastos, M.R. de Freitas, Amyotrophic lateral sclerosis: new perpectives and update, Neurol. Int. 7(2) (2015).

[2] O. Hardiman, A. Al-Chalabi, A. Chio, E.M. Corr, G. Logroscino, W. Robberecht, P.J. Shaw, Z. Simmons, L.H. Van Den Berg, Amyotrophic lateral sclerosis, Nature Reviews Disease Primers 3 (2017) 17071.

[3] B. Oskarsson, T.F. Gendron, N.P. Staff, Amyotrophic lateral sclerosis: an update for 2018, Mayo Clinic Proceedings, Elsevier, 2018, pp. 1617-1628.

[4] R. Chia, A. Chiò, B.J. Traynor, Novel genes associated with amyotrophic lateral sclerosis: diagnostic and clinical implications, Lancet Neurol. 17(1) (2018) 94-102.

[5] P. Van Damme, W. Robberecht, L. Van Den Bosch, Modelling amyotrophic lateral sclerosis: progress and possibilities, Dis. Models Mech. 10(5) (2017) 537-549.

[6] J. Rosenfeld, M.J. Strong, Challenges in the understanding and treatment of amyotrophic lateral sclerosis/motor neuron disease, Neurotherapeutics 12(2) (2015) 317-325.

[7] D. Petrov, C. Mansfield, A. Moussy, O. Hermine, ALS clinical trials review: 20 years of failure. Are we any closer to registering a new treatment?, Front. Aging Neurosci. 9 (2017) 68.

[8] Z. Mazibuko, Y.E. Choonara, P. Kumar, L.C. Du Toit, G. Modi, D. Naidoo, V. Pillay, A review of the potential role of nano-enabled drug delivery technologies in amyotrophic lateral sclerosis: lessons learned from other neurodegenerative disorders, J. Pharm. Sci. 104(4) (2015) 1213-1229.

[9] Y.H. Tsou, X.Q. Zhang, H. Zhu, S. Syed, X. Xu, Drug delivery to the brain across the blood–brain barrier using nanomaterials, Small 13(43) (2017) 1701921.

[10] A. Sharma, A.K. Lyashchenko, L. Lu, S.E. Nasrabady, M. Elmaleh, M. Mendelsohn, A. Nemes, J.C. Tapia, G.Z. Mentis, N.A. Shneider, ALS-associated mutant FUS induces selective motor neuron degeneration through toxic gain of function, Nat. Commun. 7 (2016) 10465.

[11] C. Soto, S. Pritzkow, Protein misfolding, aggregation, and conformational strains in neurodegenerative diseases, Nat. Neurosci. (2018) 1.

[12] C.-C. Chou, Y. Zhang, M.E. Umoh, S.W. Vaughan, I. Lorenzini, F. Liu, M. Sayegh, P.G. Donlin-Asp, Y.H. Chen, D.M. Duong, TDP-43 pathology disrupts nuclear pore complexes and nucleocytoplasmic transport in ALS/FTD, Nat. Neurosci. 21(2) (2018) 228.

[13] D.S. Howland, J. Liu, Y. She, B. Goad, N.J. Maragakis, B. Kim, J. Erickson, J. Kulik, L. DeVito, G. Psaltis, Focal loss of the glutamate transporter EAAT2 in a transgenic rat model of SOD1 mutant-mediated amyotrophic lateral sclerosis (ALS), Proc. Natl. Acad. Sci. U. S. A. 99(3) (2002) 1604-1609.

[14] M.T. Carrì, C. Valle, F. Bozzo, M. Cozzolino, Oxidative stress and mitochondrial damage: importance in non-SOD1 ALS, Front. Cell. Neurosci. 9 (2015) 41.

[15] D. Lall, R.H. Baloh, Microglia and C9orf72 in neuroinflammation and ALS and frontotemporal dementia, J. Clin. Invest. 127(9) (2017) 3250-3258.

[16] G. Morello, A.G. Spampinato, S. Cavallaro, Neuroinflammation and ALS: transcriptomic insights into molecular disease mechanisms and therapeutic targets, Mediators Inflammation 2017 (2017).

[17] M.A. McMahon, D.W. Cleveland, Gene therapy: gene-editing therapy for neurological disease, Nat. Rev. Neurol. 13(1) (2017) 7.

[18] T. Dharmadasa, M.C. Kiernan, Riluzole, disease stage and survival in ALS, Lancet Neurol. 17(5) (2018) 385-386.

[19] J. Mandrioli, S.A. Malerba, E. Beghi, N. Fini, A. Fasano, E. Zucchi, S. De Pasqua, C. Guidi, E. Terlizzi, E. Sette, Riluzole and other prognostic factors in ALS: a population-based registry study in Italy, J. Neurol. 265(4) (2018) 817-827.

[20] J.D. Rothstein, Edaravone: a new drug approved for ALS, Cell 171(4) (2017) 725.

[21] H. Lu, W.D. Le, Y.-Y. Xie, X.-P. Wang, Current therapy of drugs in amyotrophic lateral sclerosis, Curr. Neuropharmacol. 14(4) (2016) 314-321.

[22] V. Cinzia, A. Savina, S. Mario, Histamine beyond its effects on allergy: Potential therapeutic benefits for the treatment of Amyotrophic Lateral Sclerosis (ALS), Pharmacol. Ther. (2019).

[23] D. Furtado, M. Björnmalm, S. Ayton, A.I. Bush, K. Kempe, F. Caruso, Overcoming the blood–brain barrier: the role of nanomaterials in treating neurological diseases, Adv. Mater. 30(46) (2018) 1801362.

[24] E. Blanco, H. Shen, M. Ferrari, Principles of nanoparticle design for overcoming biological barriers to drug delivery, Nat. Biotechnol. 33(9) (2015) 941.

[25] M.D. Sweeney, A.P. Sagare, B.V. Zlokovic, Blood–brain barrier breakdown in Alzheimer disease and other neurodegenerative disorders, Nat. Rev. Neurol. 14(3) (2018) 133.

[26] W. Löscher, H. Potschka, Drug resistance in brain diseases and the role of

drug efflux transporters, Nat. Rev. Neurosci 6(8) (2005) 591.

[27] M. Aryal, K. Fischer, C. Gentile, S. Gitto, Y.-Z. Zhang, N. McDannold, Effects on P-glycoprotein expression after blood-brain barrier disruption using focused ultrasound and microbubbles, PLoS One 12(1) (2017) e0166061.

[28] A.M. Grabrucker, B. Ruozi, D. Belletti, F. Pederzoli, F. Forni, M.A. Vandelli, G. Tosi, Nanoparticle transport across the blood brain barrier, Tissue Barriers 4(1) (2016) e1153568.

[29] K.T. Savjani, A.K. Gajjar, J.K. Savjani, Drug solubility: importance and enhancement techniques, ISRN Pharmaceutics 2012 (2012).

[30] W.A. Banks, Characteristics of compounds that cross the blood-brain barrier, BMC Neurol., BioMed Central, 2009, p. S3.

[31] K.D. Foust, D.L. Salazar, S. Likhite, L. Ferraiuolo, D. Ditsworth, H. Ilieva, K. Meyer, L. Schmelzer, L. Braun, D.W. Cleveland, Therapeutic AAV9-mediated suppression of mutant SOD1 slows disease progression and extends survival in models of inherited ALS, Mol. Ther. 21(12) (2013) 2148-2159.

[32] M. Zheng, W. Tao, Y. Zou, O.C. Farokhzad, B. Shi, Nanotechnology-based strategies for siRNA brain delivery for disease therapy, Trends Biotechnol. 36(5) (2018) 562-575.

[33] R.S. Kadam, D.W. Bourne, U.B. Kompella, Nano-advantage in enhanced drug delivery with biodegradable nanoparticles: contribution of reduced clearance, Drug Metab. Disposition 40(7) (2012) 1380-1388.

[34] R. Nau, F. Sörgel, H. Eiffert, Penetration of drugs through the blood-cerebrospinal fluid/blood-brain barrier for treatment of central nervous system infections, Clin. Microbiol. Rev. 23(4) (2010) 858-883.

[35] F. ud Din, W. Aman, I. Ullah, O.S. Qureshi, O. Mustapha, S. Shafique, A. Zeb, Effective use of nanocarriers as drug delivery systems for the treatment of selected tumors, Int. J. Nanomed. 12 (2017) 7291.

[36] M. Sharma, R. Sharma, D.K. Jain, Nanotechnology based approaches for enhancing oral bioavailability of poorly water soluble antihypertensive drugs,

Scientifica 2016 (2016).

[37] R.P. Dash, R.J. Babu, N.R. Srinivas, Two decades-long journey from Riluzole to Edaravone: revisiting the clinical pharmacokinetics of the only two amyotrophic lateral sclerosis therapeutics, Clin Pharmacokinet 57(11) (2018) 1385-1398.

[38] Z. Li, S. Tan, S. Li, Q. Shen, K. Wang, Cancer drug delivery in the nano era: An overview and perspectives, Oncol. Rep. 38(2) (2017) 611-624.

[39] C. Saraiva, C. Praça, R. Ferreira, T. Santos, L. Ferreira, L. Bernardino, Nanoparticle-mediated brain drug delivery: overcoming blood–brain barrier to treat neurodegenerative diseases, J. Controlled Release 235 (2016) 34-47.

[40] L. Kou, R. Sun, Y.D. Bhutia, Q. Yao, R. Chen, Emerging advances in P-glycoprotein inhibitory nanomaterials for drug delivery, Expert Opin Drug Deliv 15(9) (2018) 869-879.

[41] J.R. Klim, L.A. Williams, F. Limone, I.G. San Juan, B.N. Davis-Dusenbery, D.A. Mordes, A. Burberry, M.J. Steinbaugh, K.K. Gamage, R. Kirchner, ALS-implicated protein TDP-43 sustains levels of STMN2, a mediator of motor neuron growth and repair, Nat. Neurosci. 22(2) (2019) 167.

[42] S.K. Sahoo, R. Misra, S. Parveen, Nanoparticles: a boon to drug delivery, therapeutics, diagnostics and imaging, Nanomedicine in Cancer, Pan Stanford2017, pp. 73-124.

[43] J. Wang, J.D. Byrne, M.E. Napier, J.M. DeSimone, More effective nanomedicines through particle design, Small 7(14) (2011) 1919-1931.

[44] H. Sawada, Clinical efficacy of edaravone for the treatment of amyotrophic lateral sclerosis, Expert Opin. Pharmacother 18(7) (2017) 735-738.

[45] H.S. Choi, W. Liu, P. Misra, E. Tanaka, J.P. Zimmer, B.I. Ipe, M.G. Bawendi, J.V. Frangioni, Renal clearance of nanoparticles, Nat. Biotechnol. 25(10) (2007) 1165.

[46] U. Agrawal, R. Sharma, M. Gupta, S.P. Vyas, Is nanotechnology a boon for oral drug delivery?, Drug Discov. Today 19(10) (2014) 1530-1546.

[47] J. Bourquin, A. Milosevic, D. Hauser, R. Lehner, F. Blank, A. Petri□Fink, B. Rothen□Rutishauser, Biodistribution, clearance, and long□term fate of clinically relevant nanomaterials, Adv. Mater. 30(19) (2018) 1704307.

[48] D. Silva Adaya, L. Aguirre-Cruz, J. Guevara, E. Ortiz-Islas, Nanobiomaterials' applications in neurodegenerative diseases, J. Biomater. Appl. 31(7) (2017) 953-984.

[49] E. Posse de Chaves, S. Sipione, Sphingolipids and gangliosides of the nervous system in membrane function and dysfunction, FEBS Lett. 584(9) (2010) 1748-1759.

[50] K.A. Sheikh, G. Zhang, Antibody-based neuronal and axonal delivery vectors for targeted ligand delivery, Neural Regen. Res. 11(5) (2016) 712.

[51] D.L. Sellers, J.M. Bergen, R.N. Johnson, H. Back, J.M. Ravits, P.J. Horner, S.H. Pun, Targeted axonal import (TAxI) peptide delivers functional proteins into spinal cord motor neurons after peripheral administration, Proc. Natl. Acad. Sci. U. S. A 113(9) (2016) 2514-2519.

[52] F. Muhammad, M. Guo, W. Qi, F. Sun, A. Wang, Y. Guo, G. Zhu, pH-triggered controlled drug release from mesoporous silica nanoparticles via intracelluar dissolution of ZnO nanolids, J. Am. Chem. Soc. 133(23) (2011) 8778-8781.

[53] W. Lv, J. Xu, X. Wang, X. Li, Q. Xu, H. Xin, Bioengineered boronic ester modified dextran polymer nanoparticles as reactive oxygen species responsive nanocarrier for ischemic stroke treatment, ACS Nano 12(6) (2018) 5417-5426.

[54] S.W. Kim, K.T. Oh, Y.S. Youn, E.S. Lee, Hyaluronated nanoparticles with pH-and enzyme-responsive drug release properties, Colloids Surf. B. Biointerfaces 116 (2014) 359-364.

[55] J. Geng, M. Li, L. Wu, C. Chen, X. Qu, Mesoporous silica nanoparticle□based H2O2 responsive controlled□release system used for Alzheimer's disease treatment, Adv. Healthcare Mater. 1(3) (2012) 332-336.

[56] H.C. Wu, T.W. Wang, M.C. Bohn, F.H. Lin, M. Spector, Novel magnetic

hydroxyapatite nanoparticles as non☐viral vectors for the glial cell line☐derived neurotrophic factor gene, Adv. Funct. Mater. 20(1) (2010) 67-77.

[57] S.S. Minami, B. Sun, K. Popat, T. Kauppinen, M. Pleiss, Y. Zhou, M.E. Ward, P. Floreancig, L. Mucke, T. Desai, Selective targeting of microglia by quantum dots, J. Neuroinflammation 9(1) (2012) 22.

[58] J. Nicolas, S. Mura, D. Brambilla, N. Mackiewicz, P. Couvreur, Design, functionalization strategies and biomedical applications of targeted biodegradable/biocompatible polymer-based nanocarriers for drug delivery, Chem. Soc. Rev. 42(3) (2013) 1147-1235.

[59] L. Fu, M. Morsch, B. Shi, G. Wang, A. Lee, R. Radford, Y. Lu, D. Jin, R. Chung, A versatile upconversion surface evaluation platform for bio–nano surface selection for the nervous system, Nanoscale 9(36) (2017) 13683-13692.

[60] L. Liu, Y. Li, R. Liu, Q. Shen, Y. Li, Z. Shi, J. Shen, W. Ji, X. Zhang, Switchable nanoparticle for programmed gene-chem delivery with enhanced neuronal recovery and CT imaging for neurodegenerative disease treatment, Mater. Horiz. (2019).

[61] H. Blasco, S. Mavel, P. Corcia, P. Gordon, The glutamate hypothesis in ALS: pathophysiology and drug development, Curr. Med. Chem. 21(31) (2014) 3551-3575.

[62] S. Zarei, K. Carr, L. Reiley, K. Diaz, O. Guerra, P.F. Altamirano, W. Pagani, D. Lodin, G. Orozco, A. Chinea, A comprehensive review of amyotrophic lateral sclerosis, Surg. Neurol. Int. 6 (2015).

[63] S.K. Verma, I. Arora, K. Javed, M. Akhtar, M. Samim, Enhancement in the neuroprotective power of riluzole against cerebral ischemia using a brain targeted drug delivery vehicle, ACS Appl. Mater. Interfaces 8(30) (2016) 19716-19723.

[64] M.L. Bondì, E.F. Craparo, G. Giammona, F. Drago, Brain-targeted solid lipid nanoparticles containing riluzole: preparation, characterization and biodistribution, Nanomedicine 5(1) (2010) 25-32.

[65] P. Rao, M.M. Yallapu, Y. Sari, P.B. Fisher, S. Kumar, Designing novel

nanoformulations targeting glutamate transporter excitatory amino acid transporter 2: Implications in treating drug addiction, J. Pers. Med. 1(1) (2015) 3.

[66] T.M. File Jr, M.H. Wilcox, G.E. Stein, Summary of ceftaroline fosamil clinical trial studies and clinical safety, Clin. Infect. Dis 55(suppl_3) (2012) S173-S180.

[67] Q. Jin, Y. Cai, S. Li, H. Liu, X. Zhou, C. Lu, X. Gao, J. Qian, J. Zhang, S. Ju, Edaravone-encapsulated agonistic micelles rescue ischemic brain tissue by tuning blood-brain barrier permeability, Theranostics 7(4) (2017) 884.

[68] T. Yang, L. Ferrill, L. Gallant, S. McGillicuddy, T. Fernandes, N. Schields, S. Bai, Verapamil and riluzole cocktail liposomes overcome pharmacoresistance by inhibiting P-glycoprotein in brain endothelial and astrocyte cells: A potent approach to treat amyotrophic lateral sclerosis, Eur. J. Pharm. Sci. 120 (2018) 30-39.

[69] H. Wei, E. Wang, Nanomaterials with enzyme-like characteristics (nanozymes): next-generation artificial enzymes, Chem. Soc. Rev. 42(14) (2013) 6060-6093.

[70] J. Wu, X. Wang, Q. Wang, Z. Lou, S. Li, Y. Zhu, L. Qin, H. Wei, Nanomaterials with enzyme-like characteristics (nanozymes): next-generation artificial enzymes (II), Chem. Soc. Rev. 48(4) (2019) 1004-1076.

[71] W. DeCoteau, K.L. Heckman, A.Y. Estevez, K.J. Reed, W. Costanzo, D. Sandford, P. Studlack, J. Clauss, E. Nichols, J. Lipps, Cerium oxide nanoparticles with antioxidant properties ameliorate strength and prolong life in mouse model of amyotrophic lateral sclerosis, Nanomed. Nanotechnol. Biol. Med. 12(8) (2016) 2311-2320.

[72] Q. Bao, P. Hu, Y. Xu, T. Cheng, C. Wei, L. Pan, J. Shi, Simultaneous Blood–Brain Barrier Crossing and Protection for Stroke Treatment Based on Edaravone-Loaded Ceria Nanoparticles, ACS Nano 12(7) (2018) 6794-6805.

[73] W. Zhao, D.R. Beers, S.H. Appel, Immune-mediated mechanisms in the pathoprogression of amyotrophic lateral sclerosis, J. Neuroimmune Pharmacol

8(4) (2013) 888-899.

[74] G. Sun, S. Zeng, X. Liu, H. Shi, R. Zhang, B. Wang, C. Zhou, T. Yu, Synthesis and Characterization of a Silica-Based Drug Delivery System for Spinal Cord Injury Therapy, Nano-Micro Letters 11(1) (2019) 23.

[75] S.I. Khalid, L. Ampie, R. Kelly, S.S. Ladha, C. Dardis, Immune modulation in the treatment of amyotrophic lateral sclerosis: a review of clinical trials, Front. Neurol. 8 (2017) 486.

[76] M. Kiaei, S. Petri, K. Kipiani, G. Gardian, D.-K. Choi, J. Chen, N.Y. Calingasan, P. Schafer, G.W. Muller, C. Stewart, Thalidomide and lenalidomide extend survival in a transgenic mouse model of amyotrophic lateral sclerosis, J. Neurosci. 26(9) (2006) 2467-2473.

[77] L. Zecca, M.B. Youdim, P. Riederer, J.R. Connor, R.R. Crichton, Iron, brain ageing and neurodegenerative disorders, Nat. Rev. Neurol. 5(11) (2004) 863.

[78] R.J. Ward, D.T. Dexter, R.R. Crichton, Neurodegenerative diseases and therapeutic strategies using iron chelators, J. Trace Elem. Med. Biol 31 (2015) 267-273.

[79] D. J Bonda, G. Liu, P. Men, G. Perry, M. A Smith, X. Zhu, Nanoparticle delivery of transition-metal chelators to the brain: oxidative stress will never see it coming!, CNS Neurol Disord Drug Targets (Formerly Current Drug Targets-CNS & Neurological Disorders) 11(1) (2012) 81-85.

[80] W. Chen, J. Ouyang, X. Yi, Y. Xu, C. Niu, W. Zhang, L. Wang, J. Sheng, L. Deng, Y.N. Liu, Black phosphorus nanosheets as a neuroprotective nanomedicine for neurodegenerative disorder therapy, Adv. Mater. 30(3) (2018) 1703458.

[81] M. Di Carlo, D. Giacomazza, P. Picone, D. Nuzzo, P.L. San Biagio, Are oxidative stress and mitochondrial dysfunction the key players in the neurodegenerative diseases?, Free Radic. Res. 46(11) (2012) 1327-1338.

[82] R. Wen, B. Banik, R.K. Pathak, A. Kumar, N. Kolishetti, S. Dhar, Nanotechnology inspired tools for mitochondrial dysfunction related diseases, Adv. Drug Del. Rev. 99 (2016) 52-69.

[83] H.J. Kwon, D. Kim, K. Seo, Y.G. Kim, S.I. Han, T. Kang, M. Soh, T. Hyeon, Ceria Nanoparticle Systems for Selective Scavenging of Mitochondrial, Intracellular, and Extracellular Reactive Oxygen Species in Parkinson's Disease, Angew Chem. Int. Ed. Engl. 57(30) (2018) 9408-9412.

[84] H.J. Kwon, M.-Y. Cha, D. Kim, D.K. Kim, M. Soh, K. Shin, T. Hyeon, I. Mook-Jung, Mitochondria-targeting ceria nanoparticles as antioxidants for Alzheimer's disease, ACS Nano 10(2) (2016) 2860-2870.

[85] B. Surnar, U. Basu, B. Banik, A. Ahmad, B. Marples, N. Kolishetti, S. Dhar, Nanotechnology-mediated crossing of two impermeable membranes to modulate the stars of the neurovascular unit for neuroprotection, Proc. Natl. Acad. Sci. U. S. A. 115(52) (2018) E12333-E12342.

[86] W. Tan, P. Pasinelli, D. Trotti, Role of mitochondria in mutant SOD1 linked amyotrophic lateral sclerosis, BBA-MOL BASIS DIS. 1842(8) (2014) 1295-1301.

[87] S. Lee, H.-J. Kim, Prion-like mechanism in amyotrophic lateral sclerosis: are protein aggregates the key?, Exp. Neurobiol. 24(1) (2015) 1-7.

[88] J.P. Taylor, R.H. Brown Jr, D.W. Cleveland, Decoding ALS: from genes to mechanism, Nature 539(7628) (2016) 197.

[89] E.L. Scotter, H.-J. Chen, C.E. Shaw, TDP-43 proteinopathy and ALS: insights into disease mechanisms and therapeutic targets, Neurotherapeutics 12(2) (2015) 352-363.

[90] L.A. Becker, B. Huang, G. Bieri, R. Ma, D.A. Knowles, P. Jafar-Nejad, J. Messing, H.J. Kim, A. Soriano, G. Auburger, Therapeutic reduction of ataxin-2 extends lifespan and reduces pathology in TDP-43 mice, Nature 544(7650) (2017) 367.

[91] D.M. O'Connor, N.M. Boulis, Gene therapy for neurodegenerative diseases, Trends Mol. Med. 21(8) (2015) 504-512.

[92] Y. Manabe, I. Nagano, M. Gazi, T. Murakami, M. Shiote, M. Shoji, H. Kitagawa, Y. Setoguchi, K. Abe, Adenovirus-mediated gene transfer of glial cell line-derived neurotrophic factor prevents motor neuron loss of transgenic model

mice for amyotrophic lateral sclerosis, Apoptosis 7(4) (2002) 329-334.

[93] M. Suzuki, C.N. Svendsen, Ex vivo gene therapy using human mesenchymal stem cells to deliver growth factors in the skeletal muscle of a familial ALS rat model, Gene Therapy for Neurological Disorders, Springer2016, pp. 325-336.

[94] L.V. Reddy, T.M. Miller, RNA-targeted Therapeutics for ALS, Neurotherapeutics 12(2) (2015) 424-427.

[95] M. Rezaee, R.K. Oskuee, H. Nassirli, B. Malaekeh-Nikouei, Progress in the development of lipopolyplexes as efficient non-viral gene delivery systems, J. Controlled Release 236 (2016) 1-14.

[96] J.M. Scarrott, S. Herranz-Martín, A.R. Alrafiah, P.J. Shaw, M. Azzouz, Current developments in gene therapy for amyotrophic lateral sclerosis, Expert Opin. Biol. Ther. 15(7) (2015) 935-947.

[97] J. Chen, Z. Guo, H. Tian, X. Chen, Production and clinical development of nanoparticles for gene delivery, Mol. Ther-Meth. Clin. D 3 (2016) 16023.

[98] L. Chen, C. Watson, M. Morsch, N.J. Cole, R.S. Chung, D.N. Saunders, J.J. Yerbury, K.L. Vine, Improving the delivery of SOD1 antisense oligonucleotides to motor neurons using calcium phosphate-lipid nanoparticles, Front. Neurosci. 11 (2017) 476.

[99] Q. Guo, X. Zheng, P. Yang, X. Pang, K. Qian, P. Wang, S. Xu, D. Sheng, L. Wang, J. Cao, Small interfering RNA delivery to the neurons near the amyloid plaques for improved treatment of Alzheimer′s disease, Acta Pharm. Sin. B 9(3) (2019) 590-603.

[100] S. Shruthi, R. Sumitha, A.M. Varghese, S. Ashok, B.C. Sagar, T. Sathyaprabha, A. Nalini, B.W. Kramer, T.R. Raju, K. Vijayalakshmi, Brain-derived neurotrophic factor facilitates functional recovery from ALS-cerebral spinal fluid-induced neurodegenerative changes in the NSC-34 motor neuron cell line, J. Neurodegener. Dis. 17(1) (2017) 44-58.

[101] J. Tan, Y. Wang, X. Yip, F. Glynn, R.K. Shepherd, F. Caruso, Nanoporous peptide particles for encapsulating and releasing neurotrophic factors in an animal

model of neurodegeneration, Adv. Mater. 24(25) (2012) 3362-3366.

[102] C.-Y. Chung, M. Lin, I. Lee, T.-H. Lee, M.-H. Lee, J.-T. Yang, Brain-derived neurotrophic factor loaded PS80 PBCA nanocarrier for in vitro neural differentiation of mouse induced pluripotent stem cells, Int. J. Mol. 18(3) (2017) 663.

[103] J.R. Kanwar, B. Sriramoju, R.K. Kanwar, Neurological disorders and therapeutics targeted to surmount the blood–brain barrier, Int. J. Nanomedicine 7 (2012) 3259.

[104] I. Khalin, R. Alyautdin, T.W. Wong, J. Gnanou, G. Kocherga, J. Kreuter, Brain-derived neurotrophic factor delivered to the brain using poly (lactide-co-glycolide) nanoparticles improves neurological and cognitive outcome in mice with traumatic brain injury, Drug Deliv. 23(9) (2016) 3520-3528.

[105] Y. Anraku, H. Kuwahara, Y. Fukusato, A. Mizoguchi, T. Ishii, K. Nitta, Y. Matsumoto, K. Toh, K. Miyata, S. Uchida, Glycaemic control boosts glucosylated nanocarrier crossing the BBB into the brain, Nat. Commun. 8(1) (2017) 1001.

[106] C. Lee, H.S. Hwang, S. Lee, B. Kim, J.O. Kim, K.T. Oh, E.S. Lee, H.G. Choi, Y.S. Youn, Rabies virus□inspired silica□coated gold nanorods as a photothermal therapeutic platform for treating brain tumors, Adv. Mater. 29(13) (2017) 1605563.

[107] M.J. Haney, N.L. Klyachko, Y. Zhao, R. Gupta, E.G. Plotnikova, Z. He, T. Patel, A. Piroyan, M. Sokolsky, A.V. Kabanov, Exosomes as drug delivery vehicles for Parkinson's disease therapy, J. Controlled Release 207 (2015) 18-30.

[108] S.E. Andaloussi, S. Lakhal, I. Mäger, M.J. Wood, Exosomes for targeted siRNA delivery across biological barriers, Adv. Drug Del. Rev. 65(3) (2013) 391-397.

[109] L. Alvarez-Erviti, Y. Seow, H. Yin, C. Betts, S. Lakhal, M.J. Wood, Delivery of siRNA to the mouse brain by systemic injection of targeted exosomes, Nat. Biotechnol. 29(4) (2011) 341.

[110] M. Riazifar, M.R. Mohammadi, E.J. Pone, A. Yeri, C. Lässer, A.I. Segaliny,

L.L. McIntyre, G.V. Shelke, E. Hutchins, A. Hamamoto, Stem Cell-Derived Exosomes as Nanotherapeutics for Autoimmune and Neurodegenerative Disorders, ACS Nano (2019).

[111] J.K. Patra, G. Das, L.F. Fraceto, E.V.R. Campos, M. del Pilar Rodriguez-Torres, L.S. Acosta-Torres, L.A. Diaz-Torres, R. Grillo, M.K. Swamy, S. Sharma, Nano based drug delivery systems: recent developments and future prospects, J. Nanobiotechnology 16(1) (2018) 71.

[112] X. Xu, W. Ho, X. Zhang, N. Bertrand, O. Farokhzad, Cancer nanomedicine: from targeted delivery to combination therapy, Trends Mol. Med. 21(4) (2015) 223-232.

[113] A.C. Anselmo, S. Mitragotri, Nanoparticles in the clinic, Biosens. Bioelectron. 1(1) (2016) 10-29.

[114] H. Su, Y. Wang, Y. Gu, L. Bowman, J. Zhao, M. Ding, Potential applications and human biosafety of nanomaterials used in nanomedicine, J. Appl. Toxicol. 38(1) (2018) 3-24.

[115] M.S. Muthu, B. Wilson, Challenges posed by the scale-up of nanomedicines, Nanomedicine 7(3) (2012) 307-309.

Chapter 3

In the Chapter 2, we conducted a literature review about nanotechnology inspired strategies in ALS treatment, which has provided us new insights in designing novel nanostructures for controllable and traceable drug delivery. Among numerous nanostructures, Poly(amidoamine) dendrimers (PAMAM) have been recognized as one of the most versatile nanoparticles that can be utilized for drug/gene delivery, diagnosis and bioimaging due to their really small size, highly branched, mono-disperse, and abundant surface functional agents [1, 2]. However, the inherent cytotoxicity and a lack of detectable signals have impeded its practical applications. To address the above problems, several intrinsically blue fluorescent PAMAM have been designed and showed great advantages to fluorescently-labelled PAMAM dendrimers in terms of biocompatibility, structure stability, and photo-stability [3, 4]. Nonetheless, there are still some drawbacks linked to those intrinsically blue fluorescent PAMAM, such as low emission intensity, using UV as excitation source that may harmful to healthy cells and tissues, under UV excitation the strong fluorescent background from biological organisms may affect their fluorescent performance. In this chapter, we engaged in developing new intrinsically fluorescent PAMAM (IF-PAMAM) to address the above obstacles that limiting the application of those blue fluorescent PAMAM.

In this chapter, we described the development of a novel green fluorescent PAMAM dendrimer (FG5) through convenient modification of the primary amine groups of PAMAM with acetaldehyde. The fabricated FG5 can emit strong green fluorescence, which is contributed to the n-π* transition in the resulting Schiff bases [5]. Based on our best knowledge and literature review, this is the first report of this type of green fluorescent PAMAM. Before we apply this novel FG5 in ALS study, we choose fluorescent anticancer drug doxorubicin as a model drug to evaluate the FG5 as fluorescent nanocarrier for traceable and controlled drug delivery. Due to its inherent fluorescence, Doxorubicin (DOX) is widely used to

evaluate the drug delivery system, in addition the low solubility of DOX in water makes it can be effectively loaded in the hydrophobic cavity of PAMAM. [6]. Considering current ALS treatment drugs (Edaravone and Riluzole) are non-fluorescent, the fluorescent feature of DOX allow us to achieve dual tracking of nanocarrier and drug in *in vitro* models, which provides the basis to develop FG5 based nanomedicines for ALS treatment. The effective drug delivery efficiency and excellent intracellular tracking ability made this novel intrinsically green fluorescent PAMAM promising candidates suitable for delivering a wide of clinical drugs.

3.1 Contribution to Paper

The results generated from this chapter were reported in a first-author peer reviewed paper in ***Biomacromolecules.***

	G. W	L. F	A. W	X.C	D.L	M. H	A.L	R.C	H.R	M. I	X.L	Y.L	B. S
Experiment Design	•		•									•	•
Sample Preparation	•					•				•			
Data Collection	•	•											
Analysis	•	•											
Manuscript	•	•	•	•	•		•	•	•		•	•	•

I undertook the majority of work towards this publication (approximately 80%) from literature review, experiment design, data collection, data analysis to the final stage of publication preparation. My supervisor A.W, Y.L and B.S have contributed great work in helping me design the experiment and revise the manuscript. Other people have contributed depended effort in helping me prepare samples, analyse data and revise the manuscript.

Reference:

1. Mekuria, S. L.; Debele, T. A.; Tsai, H.-C., *Rsc Advances* **2016,** *6* (68), 63761-63772.

2. Li, J.; Liang, H.; Liu, J.; Wang, Z., *Int. J. Pharm.* **2018,** *546* (1-2), 215-225.

3. Tsai, Y.-J.; Hu, C.-C.; Chu, C.-C.; Imae, T., *Biomacromolecules* **2011,** *12* (12), 4283-4290.

4. Janaszewska, A.; Studzian, M.; Petersen, J. F.; Ficker, M.; Paolucci, V.; Christensen, J. B.; Tomalia, D. A.; Klajnert-Maculewicz, B., *Colloids Surf. B. Biointerfaces* **2017,** *159*, 211-216.

5. Du, X.; Shi, B.; Tang, Y.; Dai, S.; Qiao, S. Z., *Biomaterials* **2014,** *35* (21), 5580-5590.

6. Liao, H.; Liu, H.; Li, Y.; Zhang, M.; Tomás, H.; Shen, M.; Shi, X., *J. Appl. Polym. Sci.* **2014,** *131* (11).

Label-free fluorescent poly(amidoamine) dendrimer for traceable and controlled drug delivery

Guoying Wang[a,b], Libing Fu[a,b], Adam Walker [a,e], Xianfeng Chen[f] , David B Lovejoy [a], Mingcong Hao[b], Albert Lee [a], Roger Chung[a], Helen Rizos[a], Mal Irvine[a], Xiuhua Liu*[c], Yiqing Lu* [b,d], Bingyang Shi*[a,b]

[a]Department of Biomedical Sciences, Faculty of Medicine & Health Sciences, Macquarie University, Sydney, NSW 2109, Australia

[b]Henan-Macquarie University joint center for Biomedical Innovation, Henan University, Kaifeng, 475001, China

[c]School of Chemical Engineering, Henan University, Kaifeng, 475001, China

[d]Department of Physics and Astronomy, Faculty of Sciences & Engineering, Macquarie University, Sydney, NSW 2109, Australia

[e]Queensland Brain Institute, The University of Queensland, St Lucia, QLD 4072, Australia

[f]School of Engineering, Institute of Bioengineering, The University of Edinburgh, King's Buildings, Mayfield Road, Edinburgh EH93JL, United Kingdom

Abstract

Poly(amidoamine) dendrimer (PAMAM) is well known for its high efficiency as a drug delivery vehicle. However, the intrinsic cytotoxicity and inherent lack of a detectable signal to facilitate tracking have impeded its practical applications. Herein, we have developed a novel label-free fluorescent and biocompatible PAMAM derivative by simple surface modification of PAMAM using acetaldehyde. The modified PAMAM possessed a strong green fluorescence, which was generated by the C=N bonds of the resulting Schiff Bases via n-π^* transition, while the intrinsic cytotoxicity of PAMAM was simultaneously ameliorated. Through further PEGylation, the fluorescent PAMAM demonstrated excellent intracellular tracking in human melanoma SKMEL28 cells. In addition, our PEGylated fluorescent PAMAM derivative achieved enhanced loading and

delivery efficiency of the anticancer drug doxorubicin (DOX) compared to the original PAMAM. Importantly, the accelerated kinetics of DOX-encapsulated fluorescent PAMAM nanocomposites in an acidic environment facilitated intracellular drug release, demonstrating comparable cytotoxicity to that of the free-form doxorubicin hydrochloride (DOX·HCl) against melanoma cells. Overall, our fluorescent PAMAM derivative offers a new opportunity of traceable and controlled delivery for DOX and other drugs of potential clinical importance.

Key Words:

Label-free fluorescence, PAMAM, Drug delivery, Intracellular tracking, Doxorubicin

3.2 Introduction

Dendrimers, a notable class of highly branched synthetic macromolecules, hold great promise for developing nanosized drug delivery systems (DDS) with specially designed targeting functions and controlled release capabilities for therapeutic applications in cancer, neurodegeneration and cardiovascular disease[1-4]. In particular, poly(amido amine) (PAMAM) dendrimers have attracted increasing interest as excellent candidates for DDS, due to their controllable molecular size, monodispersity and abundant surface functional groups[5-8]. To facilitate mechanistic studies and optimization of carrier design and delivery efficiency, it is practically required that the DDS have detectable signals to be traced intracellularly and in real time[9, 10]. However, the pristine PAMAM dendrimer is a non-fluorescent macromolecule, although, fluorescent labelling can be used to overcome this problem[11], these approaches result in changes in surface charge, solubility, biocompatibility and other physicochemical properties as well as limiting the potential for further surface modification and functionalization. Additionally, the cost, biosafety and disposal of labelling fluorescent materials present other problems in their practical applications[12, 13].

In last few years, researchers have reported several inherent blue photoluminescence PAMAM dendrimers and demonstrated that the emission intensity can be enhanced by lowering pH[14-16], oxidation protocols[14, 17] or surface chemistry engineering. However, most blue fluorescent dendrimers still need UV excitation, which poses major limitations in its application since UV is harmful to living cells and biological systems[19]. Moreover, to date relatively little research has reported other coloured (green, red) inherent fluorescent PAMAM. Therefore, it remains a crucial challenge to develop powerful label-free fluorescent PAMAM dendrimer for PAMAM-based DDS.

Herein, we developed a label-free green fluorescent PAMAM dendrimer by surface modification of pristine PAMAM with acetaldehyde to generate new traceable and controllable DDS (Scheme 1). Through the aldehyde-ammonia reaction, the terminal primary amino groups in PAMAM were replaced by imine. The modified PAMAM exhibited strong green fluorescence with a maximum emission at 507 nm and maximum excitation at 485 nm due to the n-π* transition of the C=N bonds in the resulting Schiff bases[20]. Attractively, this fluorescence behaviour was pH-independent, which was highly desirable for applications in biological systems. Furthermore, the intrinsic cytotoxicity of PAMAM, caused by high positive charge of the terminal amines, was substantially decreased[21], since replacement of amines by imine neutralised the overall surface charge. To ensure stability of the label-free fluorescent PAMAM in biological media, PEGylation was performed to introduce steric hindrance that prevented aggregation of the nanocarriers[22-24], and afforded excellent biocompatibility in both SKMel28 (human melanoma) and hCMEC/D3 (human brain endothelial capillary) cells. Traceability of the fluorescent PAMAM was also demonstrated in cells using fluorescence microscopy and flow cytometry. Furthermore, a model drug, doxorubicin (DOX), was encapsulated into our new nanocarriers by a precipitation method, and drug release kinetics were evaluated at different pH values[25]. Under acidic conditions, drug release was accelerated. To evaluate

cancer cell uptake and therapeutic efficacy, SKMel28 cells were used. Our optimized nanocomposites showed higher drug uptake efficacy and better therapeutic efficacy compared to hydrophobic DOX and PAMAM G5/DOX (G5/DOX) composites, respectively. These results demonstrate that this newly developed modified PAMAM is an improved DDS with potential clinical applicability.
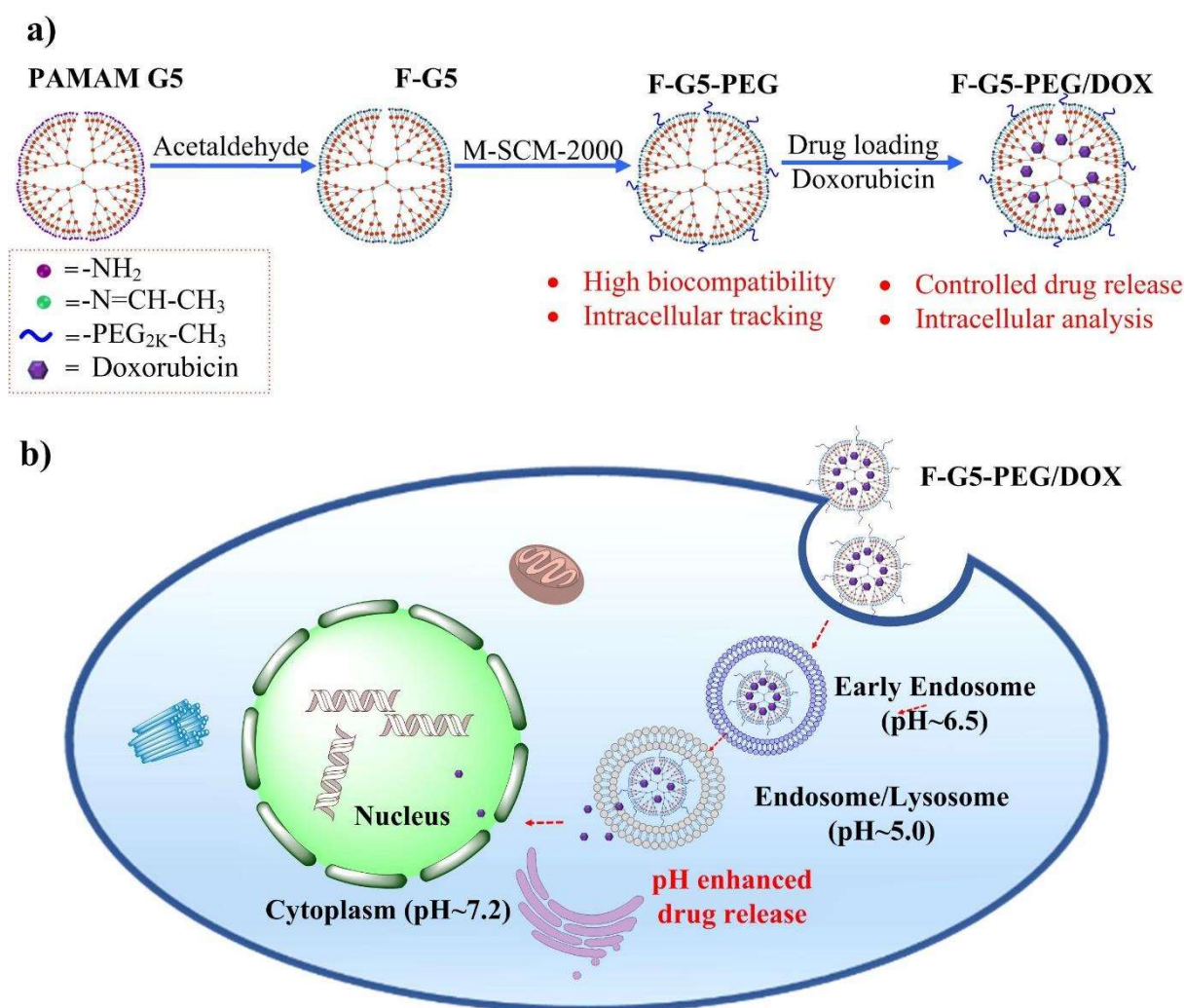
Scheme 1. A schematic description of endogenous fluorescent poly(amidoamine) dendrimer with excellent traceability and controlled drug release.

3.3 Materials and methods

3.3.1 Materials

Ethylenediamine core amine-terminated generation 5 PAMAM dendrimers (G5), acetaldehyde, triethylamine (TEA) and doxorubicin hydrochloride (DOX·HCl) were purchased from Sigma-Aldrich (NSW, Australia). Methoxy-PEG-Succinimidyl Carboxymethyl Ester (M-SCM-2000; Mw 2000) was purchased from Jenkem Technology (Beijing, China). Amicon® Ultra Centrifugal Filters (10 KD) were purchased from Merck Millipore (VIC, Australia). Dulbecco's Modified Eagle's Medium (DMEM) was purchased from Thermo Fisher Scientific (NSW, Australia), Endothelial Cell Growth Basal Medium-2 (EBM-2) was purchased from Lonza (Melbourne, Australia). VECTASHIELD® mounting medium was purchased from Vector Laboratories (US). (3-(4,5-dimethylthiazol-2-yl)-2,5-diphenyltetrazolium bromide (MTT) was purchased from Life Technologies (NSW, Australia). Other routine chemicals were obtained from Sigma-Aldrich and used as received. The water used in all the experiments was purified using a Milli-Q Plus 185 water purification system (Millipore) with a resistivity higher than 18 MU cm.

3.3.2 Synthesis of label-free Fluorescent PAMAM G5

The label-free fluorescent PAMAM G5 (F-G5) was synthesized by the reaction of acetaldehyde with amine-terminated G5 at room temperature. G5 (100 mg; 7 mmol) was dissolved in Milli-Q water (10 mL) and adjusted to pH 10 using NaOH solution (0.1 M). Acetaldehyde (in excess) was added dropwise to the G5 solution. The reaction mixture was protected from light and stirred at room temperature for 8 h, followed by centrifugation using Amicon filters at 4500 rpm for 30 min to remove any unreacted acetaldehyde. The purification process was repeated 3 times. The purified solution of F-G5 dendrimer was stored at 4 °C for further use.

3.3.3 PEGylation of F-G5

The prepared F-G5 was covalently conjugated with M-SCM-2000 via an NHS ester coupling reaction, with the feed molar ratio of 1:30. M-SCM-2000 (2.1 μmol) dissolved into 5 mL water, to which 0.07 μmol F-G5 was added quickly. The mixture was kept at room temperature and magnetically stirred for 4 h, followed by centrifugation using Amicon filters (4500 rpm for 30 min; repeated 4 times) to remove any unreacted M-SCM-2000. The purified solution of PEGylated F-G5 (F-G5-PEG) was stored at 4 °C for further use.

3.3.4 Qualification analysis of F-G5 and F-G5-PEG

Qualification analysis of F-G5 and F-G5-PEG was performed by NGC™ Medium-Pressure Liquid Chromatography Systems. Briefly, 0.5 mL G5, F-G5 or F-G5-PEG (1mg/mL in PBS, pH=7.4) was analysed by the gel filtration using an EnrichTMSEC650 (Bio-Rad) column and NGC purifier (Bio-Rad). Bovine Serum Albumins (BSA, Sigma, MW~ 66K) was used as reference protein. 0.1M PBS (pH=7.4) containing 5% glycerol was used as elution buffer.

3.3.5 Encapsulation of DOX within F-G5-PEG

DOX was encapsulated inside F-G5-PEG using a solvent-displacement (nanoprecipitation) method slightly modified from literature [26]. F-G5-PEG (0.07 μmol) was dissolved in 3 mL water, while 0.7 μmol DOX·HCl was dissolved in 0.4 mL methanol and neutralized sequentially with 3.5, 5.25, 7 μmol triethylamine (TEA) to generate hydrophobic DOX. The hydrophobic DOX solution was then added dropwise into F-G5-PEG solution and magnetically stirred overnight to evaporate excess methanol and TEA. The F-G5-PEG/DOX solution was centrifuged at 10,000 rpm for 10 min, to precipitate non-encapsulated free DOX (as free DOX is water insoluble). The precipitation was collected and dissolved into 5 mL methanol, followed by quantity analysis based on the DOX absorbance intensity at 480 nm via UV-visible measurement. G5/DOX nanocomposites were also prepared using the same protocol with the same molar ratio of G5 to DOX.

3.3.6 Characterisation

Transmission electron microscopy (TEM) was carried out using a CM10 (Philips) system at an acceleration voltage of 120 kV. F-G5-PEG was diluted to 0.5 mg/ml in distilled water and sonicated for 10 min, dropped onto carbon-coated copper grids, followed by negative staining using 2% Uranyl Acetate. UV-vis absorption spectra were recorded on a UV-2600 spectrophotometer (Shimadzu, Japan). Fluorescent emission and excitation spectra were recorded on a Fluorolog spectroscopy (Horiba, Australia). Fourier transform infrared (FTIR) spectra were taken on a NICOLET 6700 FTIR spectrometer (Thermo Scientific, Australia) at room temperature. The particle sizes and zeta potentials of samples in PBS (0.1 M) were measured at room temperature using a Zetasizer Nano ZS (Malvern, Australia) equipped with the ZET 5104 cell. ^{1}H Nuclear Magnetic Resonance (NMR) experiments were recorded using a 400 MHz Bruker NMR in D_2O.

3.3.7 Kinetic Release Study

F-G5-PEG/DOX nanocomposites and free DOX (50 μg equivalent DOX in 2 mL phosphate buffered saline (PBS), pH 7.4, 6.0 or 5.0) were placed in a dialysis bag with molecular weight cut-off (MWCO) of 10,000, hermetically tied, and suspended in 8 mL PBS buffer (pH 7.4, 6.0 or 5.0). The entire system was kept in a constant-temperature vibrator at 37 °C. Then, at each predetermined time point, 0.2 mL dialysis buffer was removed for measurement, and 0.2 mL PBS (at the corresponding pH) was added back to keep the total volume of the dialysis buffer constant. The released DOX was quantified by a microplate reader (PHERAstar FS, Australia) that measured the DOX fluorescence (λex = 480 nm, λem = 580 nm). The cumulative release (Cr) of DOX at each time point was obtained according to the equation

Cr = Wt/Wtot × 100%

where Wt and Wtot are the cumulative amount of released drug at time t and the total amount of encapsulated drug in the nanocomposites used in dialysis, respectively.

3.3.8 Cell Culture

SKMel28 cell line was obtained from the American Type Culture Collection (ATCC). Cells were cultured in DMEM supplemented with 10% fetal bovine serum (FBS, Sigma-Aldrich), 20 mM 4-(2-hydroxyethyl)-1-piperazineethanesulfonic acid (HEPES, Sigma-Aldrich), 4 mM L-Glutamine (Sigma-Aldrich), 100 U/mL penicillin, and 100 U/mL streptomycin (Life Technologies). hCMEC/D3 cell line was obtained from ATCC. Cells were cultured in EMB-2 medium supplemented with 5% FBS, 10 mM HEPES, 100 U/mL penicillin, and 100 U/mL streptomycin and 1 ng/mL basic fibroblast growth factor (Bfgf, ThermoFisher). Cultures were maintained at 37°C in a wet incubator with 5% CO_2, and the medium was replaced every 3 days.

3.3.9 Cytotoxicity Test

To test biocompatibility, SKMel28 and hCMEC/D3 cells were cultured in 96-well plates at density of 5000 cells/well and allowed to adhere overnight at 37°C in a humidified 5% CO_2-containing atmosphere. Growth media were replaced with media containing G5, F-G5, or F-G5-PEG. The cells were then incubated for 48 h before 20 μL MTT (5.0 mg/mL in PBS) was added to each well and further incubated for 4 h at 37°C. The media was then removed and 150 μL of dimethyl sulfoxide (DMSO) was added to each well to ensure complete solubilization of formazan crystals before cell viability was determined by absorption at 560 nm.

To test therapeutic efficacy, SKMel28 cells were cultured in 96-well plates at density of 5000 cells/well and allowed to adhere overnight at 37°C in a humidified 5% CO_2-containing atmosphere. Growth media were replaced with DMEM

containing DOX·HCl, DOX (TEA-treated), G5/DOX or F-G5-PEG/DOX at equivalent DOX concentrations range from 0.1 to 5 μg/mL. The cells were then incubated for 48 h, followed by MTT assay as described above.

3.3.10 Intracellular Tracking of F-PAMAM

SKMel28 cells were seeded at a concentration of 1×10^5 cells/well in 6-well plates containing slide cover glasses (24×24 mm), and cultured at 37 °C for 24 h. F-G5-PEG was added to the cell culture media to obtain a final concentration of 50 μg /mL for each well, and cells further incubated at 37 °C for 2, 4, 8 or 24 h. Cells were then washed with PBS followed by adding 1 mL Hoechst 33342 solution (Thermofisher, 1:2000 in PBS) and incubated for 10 minutes (protected from light). After Hoechst staining, cells were washed with PBS again and stained with Cytopainter (Abcam, ab176827) following the manufacturer's protocol. Live cell imaging was performed using a Zeiss LSM 880 laser-scanning confocal microscope.

3.3.11 Intracellular Drug Delivery

Intracellular drug delivery was assessed using a combination of cellular imaging and flow cytometry. For cellular imaging, SKMel28 cells were seeded at a concentration of 1×10^5 cells/well in 6-well plates containing glass slide covers and cultured at 37°C for 24 h. Next, DOX·HCl, DOX (TEA-treated), G5/DOX or F-G5-PEG/DOX were added to culture media to obtain a final DOX concentration of 2.5 μg/mL. Cells were then incubated at 37°C for 4 h, followed by washing with PBS (x 3) to remove non-cell incorporated drug. Subsequently, cells were fixed with 4 % paraformaldehyde solution and treated with VECTASHIELD® mounting medium with DAPI for 10 min at room temperature. Cells were imaged by a Zeiss LSM 880 laser-scanning confocal microscope.

For flow cytometry, SKMel28 cells were seeded at a concentration of 1×10^5 cells/well in 6-well plates and cultured at 37°C for 24 h. Next, DOX·HCl, DOX (TEA-treated), G5/DOX or F-G5-PEG/DOX were added to culture media to obtain a final DOX concentration of 2.5 μg /mL. Cells were then incubated at 37°C for 4 h, followed by washing with PBS (x3) to remove non-cell incorporated drug. Subsequently, cells were detached by trypsin, collected and concentrated, and then fixed with 4 % paraformaldehyde at 4°C overnight. The cells were analysed by a flow cytometer (BD LSR Fortessa X-20, Australia) using FITC and PE channels to quantify the amounts of F-PAMAM and DOX, respectively, in individual cells. Quantification was performed using standardized reference solutions of F-G5-PEG and DOX·HCl.

3.3.12 Statistical Analysis

One-way ANOVA was performed using Origin 8.0 software to compare the cytotoxicity of cells treated with different materials. The significance level was set as 0.05, and the data were indicated with (**) for $p < 0.01$ and (***) for $p < 0.001$. Data are expressed as the mean ± standard deviation. Each experiment was performed in triplicate.

3.4 Results and discussion

3.4.1 Physical and Optical Properties of F-PAMAM and PEGylated F-PAMAM

G5 PAMAM dendrimer was selected for the synthesis of label-free fluorescent dendrimer due to its relative small size (5.4 nm, theoretical value), monodispersity and numerous functionable amine groups[27, 28]. As shown in schematic 1, the label free fluorescent PAMAM (F-G5) was fabricated by simple surface modification using acetaldehyde. After 8 h reaction the colorless PAMAM turned to brown (Fig S1), indicating successful formation of Schiff base. PEG (M-SCM-2000) was then conjugated to the surface of F-G5 by classical esterification between N-hydroxysuccinimide (NHS) ester and primary amino groups contained in F-G5.

The F-G5 and PEGylated F-G5 (F-G5-PEG) were further characterised by TEM, DLS, FTIR, Liquid Chromatography and ^{1}H NMR.

TEM images in Fig. 1a showed that the F-G5-PEG had a relative uniform particle size of approximately 25-35 nm, which made them suitable for use as multifunctional drug nanocarriers. The size and Polydispersity Index (PDI) of nanoparticles was also acquired with DLS measurement. As shown in Fig 1 b, the initial size of G5 was 6.6±0.4 nm. After aldehyde modification, the size of F-G5 changed to 6.1±1.1nm, which is similar to G5. After PEGylation the size of F-G5-PEG increased to 7.8±0.6 nm, which was mainly caused by the addition of PEG layer. The PDI of G5, F-G5, F-G5-PEG were 0.286±0.08, 0.215±0.07, and 0.159±0.05 respectively, indicating that these nanostructures have good monodispersity. When compared the TEM results with DLS, we found that the size from TEM was significantly larger than the size from DLS, especially for G5 (theoretical size was 5.4 nm), the increased size may be caused by the formed non-uniform particle deposition and particle aggregation of dendrimers in the aqueous solution during drying step. We further analysed the zetapotential by DLS, as seen in Fig 1c, compared with G5, the zeta potential of F-G5/F-G5-PEG showed a significant charge decrease from +28.2 to approximately +4.8mV. This decreased surface charge was likely primarily due to the replacement of amino groups with non-charged methyl groups and PEG.

FTIR was next used to characterize the surface functionalization of F-G5 and F-G5-PEG. As displayed in Fig S1, the peaks at 2970, 2873 and 1374 cm^{-1} indicated the presence of -CH$_3$ groups, suggesting the successful introduction of the Schiff base (-N=CH-) structure on the PAMAM surface. The peaks at 2880 and 1098 cm^{-1} indicated the presence of C-O-C and confirm the successful conjugation of PEG on the surface of label free fluorescent dendrimer. The absorption peaks due to adsorbed H$_2$O around 1623 cm^{-1} may potentially overlap with the absorption peaks of -N=C- group and amide I, which are normally observed at 1615~1700 cm^{-1}.

The chemical structure of each dendrimer product and intermediate was also characterized by ^{1}H NMR spectroscopy. The spectra of F-G5 and F-G5-PEG were collected to further confirm the successful introduction of various functional groups to the G5 dendrimer. As shown in Fig S2, the chemical shifts of F-G5 at 1.83 and 8.37 ppm were assigned to -CH3 and -N=CH- groups respectively, demonstrating the successful incorporation of the Schiff base structure to PAMAM G5. As calculated from NMR spectrum, around 31.7% amino groups were replaced by -N=C-CH$_3$ groups. The chemical shifts of F-G5-PEG at 3.63 ppm were assigned to -CH2-CH2- repeat segments and indicate the successful conjugation of PEG on the surface of F-G5. The chemical shift peak of F-G5-PEG at 2.71 ppm assigned to -NHS was no longer detected, indicating that the NHS had completely reacted with F-G5. However, the chemical shift peak of F-G5-PEG at1.83 and 8.37 ppm was disappeared, that's likely because the plenty of PEG chain decreased the sensitivity of 1H NMR. The structure change was further characterized by fluorescent spectrophotometer.

As shown in Fig 1d, our developed PAMAM exhibited green fluorescence due to the n-π* transition of the C=N bonds in the formed Schiff bases, showing similar excitation and emission spectra as our previously reported acetaldehyde modified-cystine (AC). No emission was detected with the original G5 at 485 nm excitation (Fig S4), suggesting that the fluorescence of F-G5-PEG was only due to the formation of the C=N bonds in the formed Schiff bases. We further tested the fluorescence intensity of F-G5-PEG at three different pH values (pH 7.4, 6.0, and 5.0) and verified that the fluorescence of F-G5-PEG was pH-independent (Fig S5), suggesting that our label free fluorescent PAMAM could be generally applied to biological systems since the fluorescence will not be adversely affected by differing pH levels present in sub-cellular organelles. The long-term stability assay (shown in Fig S5) demonstrated a marginal fluorescence intensity reduction during the first 48 h (~5%) followed by a ~20% fluorescence intensity reduction after 5 days' continuous incubation, which suggested that this label-free

fluorescent PAMAM maintains excellent biological environmental stability. We further compared the fluorescence intensity of F-G5 and F-G5-PEG at the same molar concentration (Figure S6) and found that the PEGylation didn't affect the fluorescent properties, which implies that the esterification of F-G5 wouldn't change the Schiff base structure.

The molecular size of G5, F-G5 and F-G5-PEG was analysed by NGC™ Medium-Pressure Liquid Chromatography Systems. As shown in Fig 2, G5 was eluted earlier than F-G5, which maybe because the PAMAM G5 exists in dimer in PBS buffer. The elution time of F-G5 was later than that of BSA and PAMAM G5, indicating that the molecular weight of F-G5 was smaller than that of BSA and G5 dimer, which suggested that F-G5 could mainly disperse in PBS buffer as a single molecule. The elution time of F-G5-PEG was slightly earlier than that of BSA, which was mainly because the conjugated PEG increased the total molecular size of F-G5.
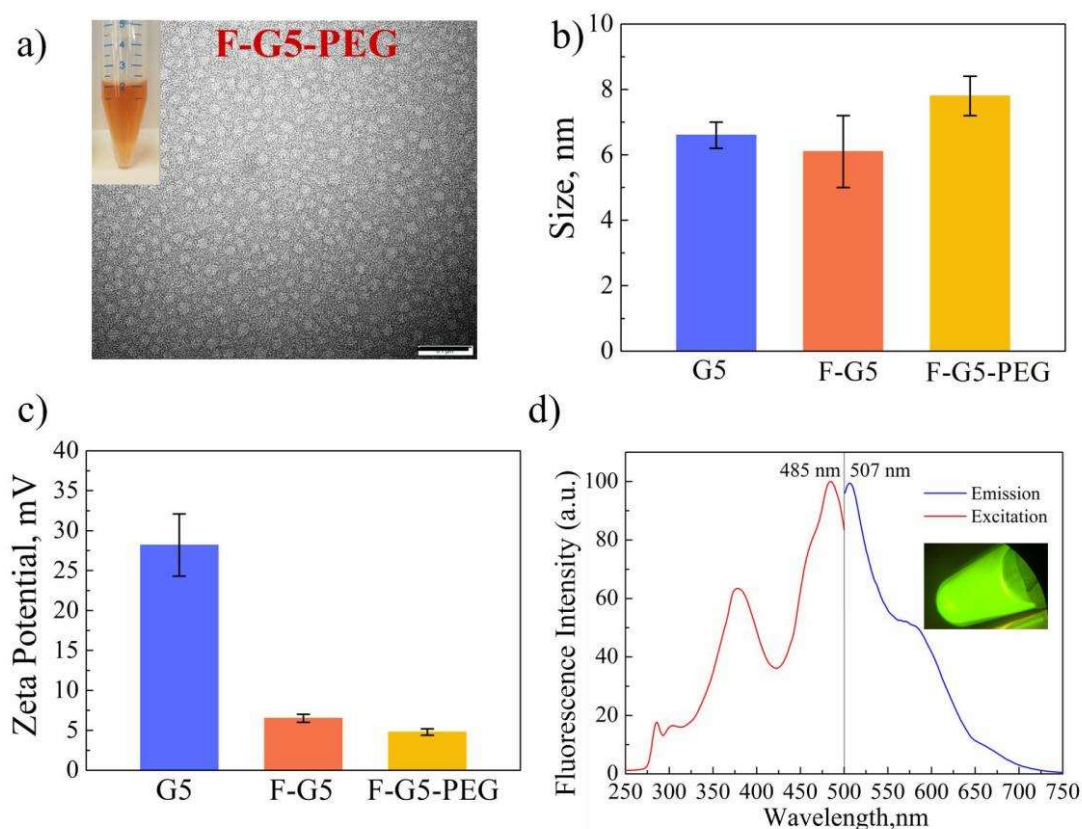
Figure 1. The physical and fluorescence characteristics of modified PAMAM, (a) TEM image of F-G5-PEG in aqueous solutions (The insets showed the digital images of samples), Bar = 0.1 μm; (b) The size distribution of G5, F-G5 and F-G5-PEG by number distribution (in PBS); (c) The zetapotential of G5, F-G5 and F-G5-PEG by DLS (in PBS) (d) The excitation and emission spectra of F-G5-PEG (The insets showed the fluorescent image of F-G5-PEG under 485 laser excitation); (b) (c) Data are expressed as the mean ± standard deviation.
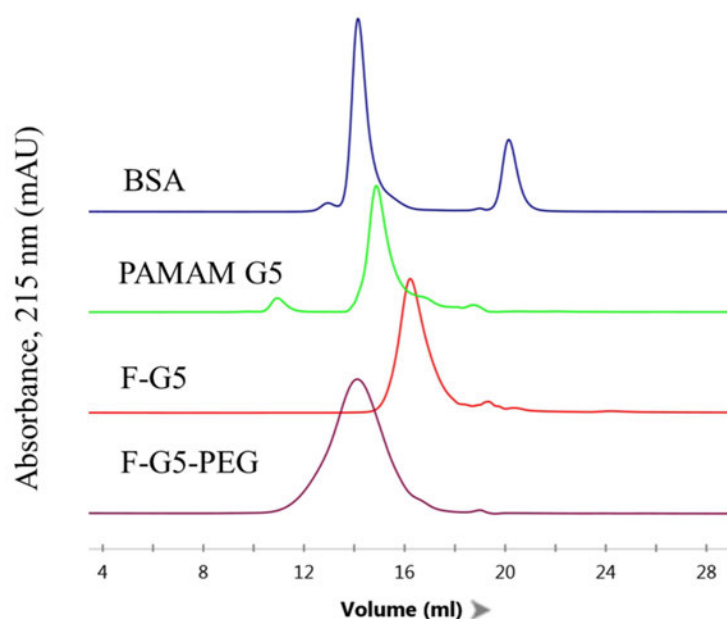
Figure 2. Chromatograms of PAMAMG5, F-G5, F-G5-PEG and BSA by NGC™ Medium-Pressure Liquid Chromatography Systems

3.4.2 Biocompatibility of F-PAMAM and PEGylated F-PAMAM
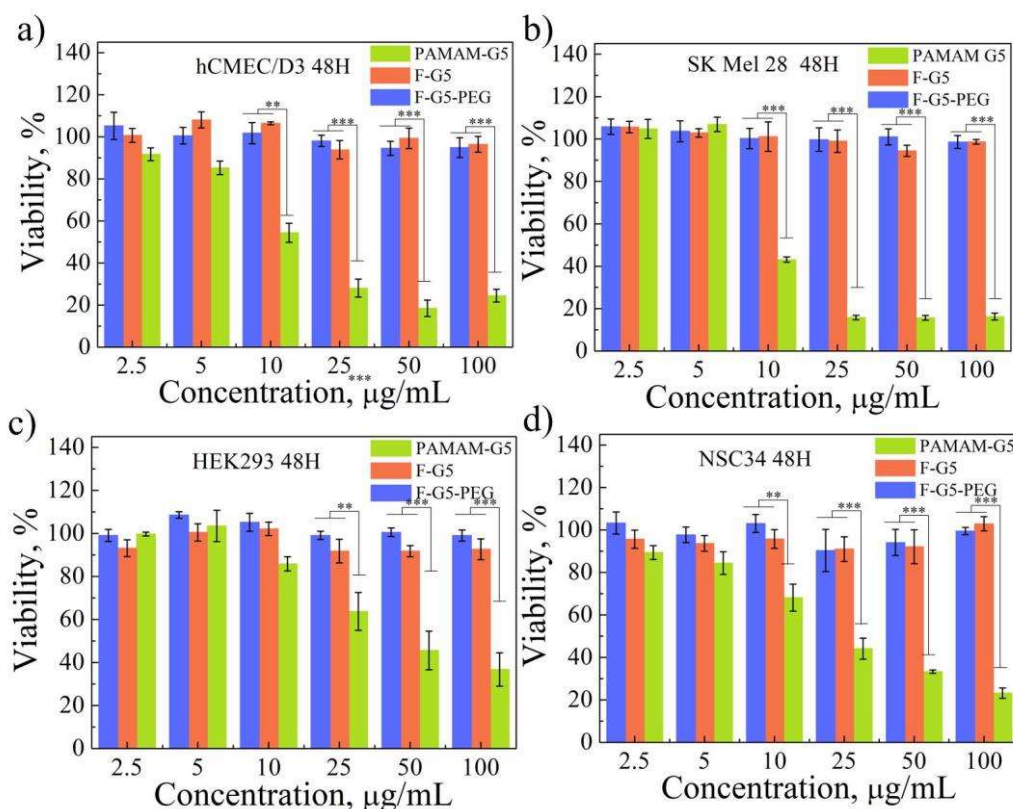
Figure 3. Biocompatibility of modified PAMAM. Cellular viability of (a) hCMEC/D3, (b) SKMel28, (c) HEK293, (d) NSC34cell lines treated with cationic PAMAM G5, F-G5 and F-G5-PEG. (***, p<0.001, **, p<0.01). Data are expressed as the mean ± standard deviation.

In DDS, the nanocarriers should be biocompatible with healthy cells. The biocompatibility of G5, F-G5, F-G5-PEG was evaluated using MTT assays in four different cell lines in the concentration range of 2.5~100 µg/mL. As shown in Fig 3a-d, after 48 h incubation, a remarkable decrease in the cytotoxicity of the cationic PAMAM dendrimers was noted when cells were exposed to the F-G5 and F-G5-PEG, indicated by the average cell viabilities of four cell lines of above 90 %, even at the highest concentration of 100 µg/mL. In great contrast, commercial G5 showed significant cytotoxicity to all cell lines, revealed by the low cell viability of below 50% at concentrations of over 10 µg/mL for hCMEC/d3 and SKMel28 cells, 25 µg/mL for NSC34 and 50 µg/mL for HEK293. In general, the intrinsic cytotoxicity of PAMAM was caused by the high positive

charges of dense terminal amines [29]. After acetaldehyde modification amines from PAMAM were replaced by imine and PEG that neutralized the overall surface charge and resulted in a significant zeta potential decrease (Fig 1c), thereby substantially alleviated cytotoxicity. These results suggested that the novel F-G5 and F-G5-PEG were potentially safe for biological application.
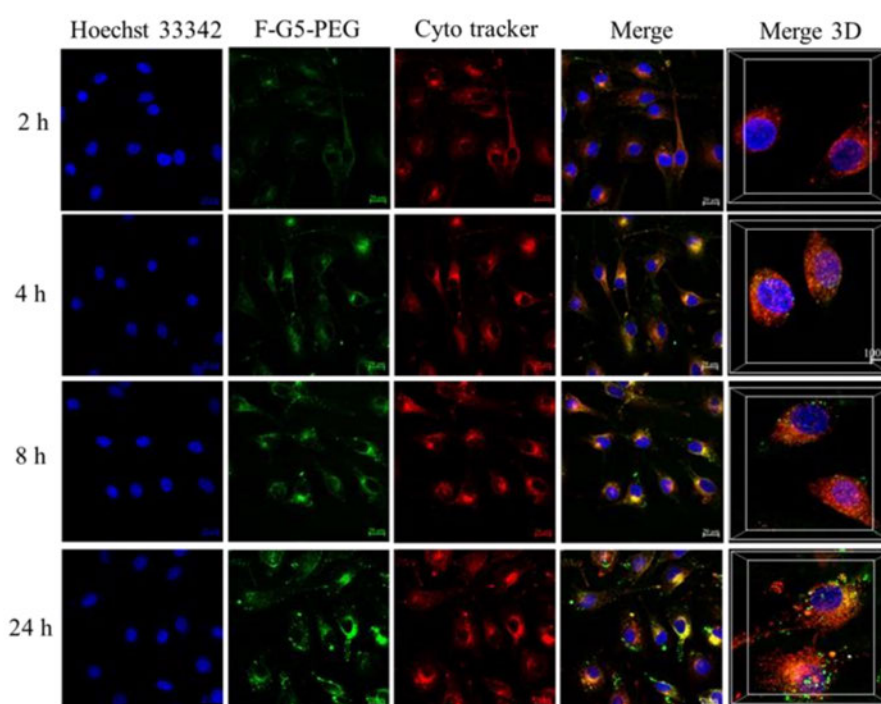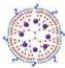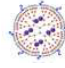
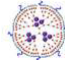### 3.4.3 Fluorescence tracking of F-G5-PEG in vitro

Figure 4. Intracellular tracking of F-G5-PEG (nanocarrier) was assessed in SKMEL28 cell line by confocal microscopy. Live cell imaging was taken at 2, 4, 8, 24 h intervals after incubation. 488 and 545 nm laser excitation were used for detecting Hoechst and Cytopainter. 2D images scale bar = 50 μm. 3D images scale bar = 100 μm.

The intracellular microenvironment-responsive behaviour of F-G5-PEG was monitored at different time intervals using fluorescence microscopy. As shown in Fig 3, after 2 h incubation, very weak green fluorescence signal was obtained. As the incubation period increased to 4 h, green fluorescent spots started to be observed, indicating some complexes have entered cell. With further prolonged

incubation time to 24 h, very bright green fluorescence images were obtained, indicating enhanced cell loading. To evaluate the subcellular localization of F-G5-PEG, the cells were stained with Cytopainter followed the manufacturer's protocol. As shown in Fig 4, at the time point 2, 4 and 8 h, the green signal (F-G5-PEG) co-localization with red signal (lysosome) very well, indicating that the F-G5-PEG was mainly accumulated in lysosome after endocytosis. After 24 h incubation, some F-G5-PEG formed to bright green granules around cell edge, that's maybe because the exocytosis of those granules. However, after 24 h incubation, most of F-G5-PEG was still co-localization with lysosome. These studies suggested that the strong green signals emitted by F-G5-PEG could potentially be used as a tool for intracellular real-time tracking and also for exploring cellular uptake mechanisms.

3.4.4 Drug Loading and Release

Table 1. Drug encapsulation efficiency and physical properties of G5/DOX and F-G5-PEG/DOX compositions

Sample	TEA:DOX·HCl (mol:mol)	Size[a], nm	Zeta, mV	EE[b], %	LE[c],%
G5/DOX	5:1	/	/	78.6±4.1	13.6±0.7
F-G5-PEG/DOX-1	5:1	59.5±7.3	6.5±0.8	94.5±2.8	7.3±0.2
F-G5-PEG/DOX-2	7.5:1	81.9±2.2	6.3±0.6	91.2±2.3	7.0±0.2
F-G5-PEG/DOX-3	10:1	127.9±1.6	8.2±1.0	84.5±3.6	6.5±0.3

a: Statistics by Z-average

b: EE= Encapsulation efficiency (EE) $= \dfrac{Wo}{Wt} \times 100$, Wt is the total DOX weight

used for drug loading and Wo is the weight of encapsulated DOX, respectively.

c: LE= drug loading efficiency (LE)$= \dfrac{Wo}{Wt+Wp} \times 100$, Wp is the total PAMAM
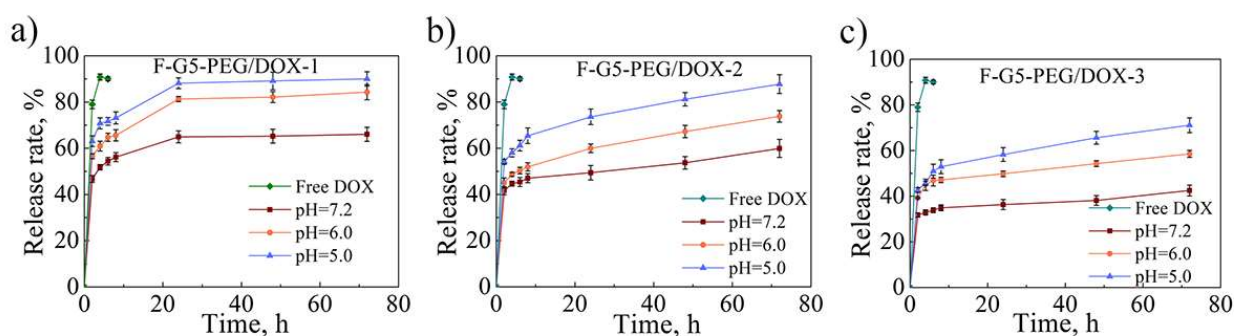
weight used for drug loading.

Figure 5. Drug release profile of (a) F-G5-PEG/DOX-1, (b) F-G5-PEG/DOX-2 and (c) F-G5-PEG/DOX-3 in PBS buffer solution with different pH value. Free DOX was used for comparison. F-G5-PEG/DOX-1/2/3 represent different drug loading procedures (Refer to table 1). Data are expressed as the mean ± standard deviation.

DOX was efficiently encapsulated into F-G5-PEG using a solvent-displacement (precipitation) method. Typically, TEA (Triethylamine) was used to neutralize DOX hydrochloride so that it could be loaded inside the PAMAM hydrophobic cavity [30]. A simple method to achieve high doxorubicin loading in biodegradable polymersomes was previously reported and demonstrated that pH conditions had a strong influence on drug loading capacity and release [31]. Similarly, we used a highly volatile organic base (TEA) to control drug loading by modulating pH conditions. We also explored the effect of molar ratio TEA to

DOX·HCl, using 5:1, 7.5:1, 10:1 as F-G5-PEG/DOX-1, -2, -3 respectively. The size and zetapotential of drug loaded nanoparticles were measured with DLS. As shown in Table 1, after drug loading, the size of F-G5-PEG/DOX composites increased dramatically compared with the carrier F-G5-PEG. Meanwhile, a higher TEA to DOX·HCl molar ratio resulted in a larger particle size. No obvious change in zetapotential were detected for all F-G5-PEG/DOX compositions, compared to the drug carrier F-G5-PEG. Presumably, DOX mostly accumulated inside the PAMAM. In our study, non-PEGylated F-G5 was also used to load DOX. However, the F-G5/DOX system was not stable in serum-containing medium and precipitation was evident by upright biological microscopy (Olympus). Additionally, a large size increase was also detected by DLS (Table S1) after mixing F-G5/DOX with 10% serum, reflecting the very smooth surface of non-PEGylated F-G5/DOX. The smooth surface of F-G5/DOX composites and extremely low surface charge significantly impaired steric stability, leading to aggregation of F-G5/DOX in serum-containing media[32]. However, with PEGylation, the F-G5-PEG/DOX system was stable in serum-containing media, and no increased particle size were detected by DLS (Table S1) during the observation period. These results were consistent with the use of PEG to improve steric hindrance and enhanced material stability in biological fluids[33].

Drug loading efficiency was determined by measuring the precipitated un-loaded DOX via UV-vis spectrometry. As shown in Table 1, F-G5-PEG/DOX-1 presented the highest drug EE (encapsulation efficiency) (94.5±2.8%) while F-

G5-PEG/DOX-3 only yielded 84.5±3.6% drug EE. The higher drug EE of F-G5-PEG/DOX-1 may be explained by the lower TEA to DOX molar ratio resulted in relative lower initial pH that slowed down the formation of dimer or multimer of DOX, thereby affording more time for DOX to assemble inside the PAMAM hydrophobic cavity. It was noteworthy that all of the F-G5-PEG/DOX compositions possessed more competitive drug EE than commercial PAMAM G5 (78.6±4.1%), the higher drug encapsulation efficiency of F-G5-PEG/Dox over G5/DOX might be that the Schiff-base terminals and PEG terminals form a protection shell, which can prevent DOX diffuse freely from dendrimer interior to outside bulk solution.

For antitumor therapeutic applications, the encapsulated DOX should be effectively released into the cytoplasm to reach the nucleus to exert its biological activity. To understand the drug release process, we investigated the cumulative release profile of F-G5-PEG/DOX, in PBS at different pH values (7.2, 6.5, 5.0). The results shown in Fig 5 indicated that DOX was sustainably released from F-G5-PEG/DOX in PBS solution at all pH values for 72 h. In comparison, free DOX drug was 'burst released' whereby almost all DOX was released within 2 h. The release of DOX from F-G5-PEG was enhanced by decreasing the pH value, revealing that the F-G5-PEG/DOX is pH sensitive. We further noticed that the drug release kinetics of the three types of F-G5-PEG/DOX were strongly associated with the initial molar ratio of TEA to DOX·HCl, reflecting the different DOX aggregation characteristics of different formulations (Table 1) as

the drug release rate was strongly associated with the solubilization of the aggregated molecules and drug diffusion. Additionally, the size of drug loaded nanocarrier will also affect the drug release rate, as smaller sizes have decreased diffusion distance which results in a faster release rate.

Fluorescence spectra can reflect the aggregation state of fluorescent molecules. DOX contains a chromophore composed of three aromatic hydroxyanthraquinonic rings [34], which can be used to monitor interactions with itself or other molecules. As shown in Fig S4, a remarkable decrease in fluorescence intensity of peaks at 550 and 595 nm were observed with the F-G5-PEG/DOX-3 compared to the equivalent amount of free DOX·HCl. This was a typical self-quenching that resulted from increased local concentrations [35]. In F-G5-PEG/DOX-3 composite, a higher TEA to DOX·HCl molar ratio resulted in a relatively higher initial pH, which facilitated dimer or multimer formation of DOX, generating a relative higher DOX local concentration and in turn leading to decreased fluorescence intensity. Meanwhile, the stronger molecular interactions would also result in a relative slower drug solubilization and diffusion rate leading to a slower drug release speed. These considerations mean that fluorescence spectra are valuable tools enabling the prediction of drug release kinetics.

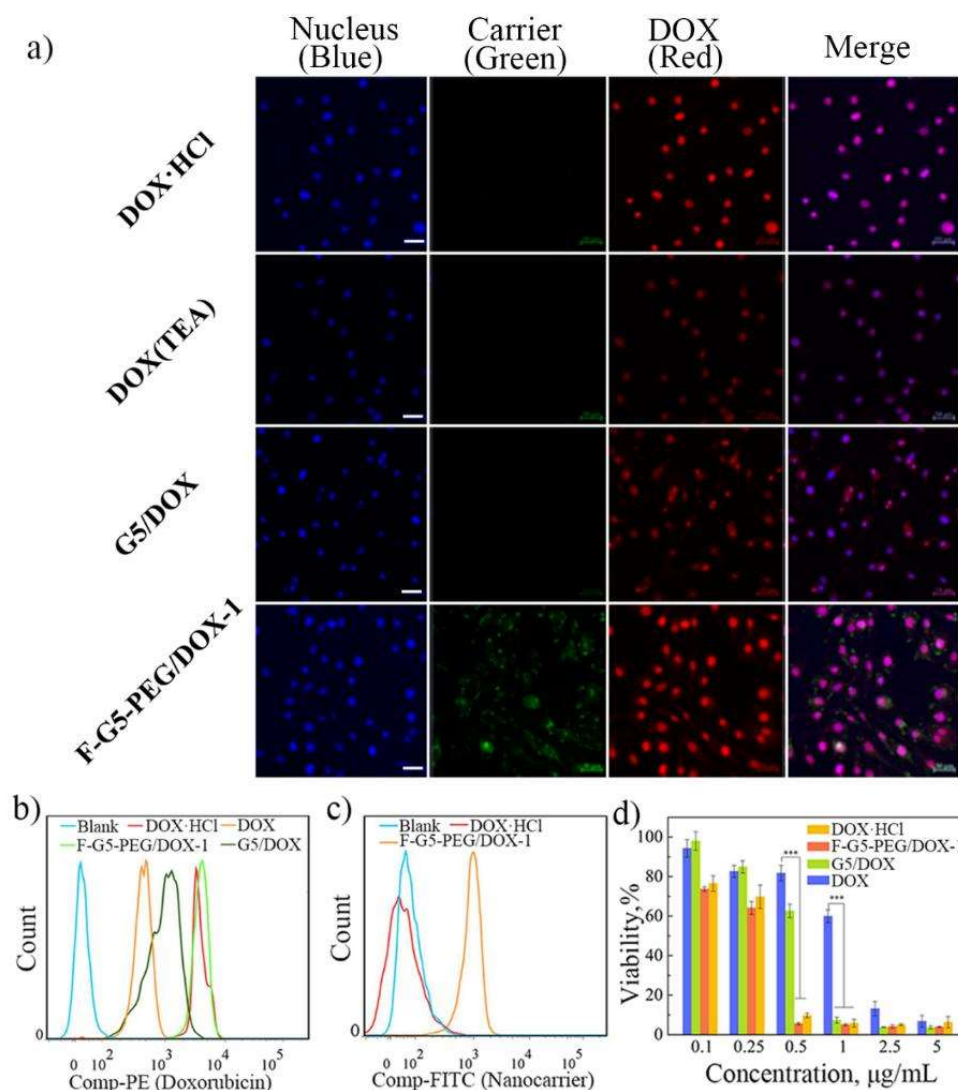3.4.5 Intracellular Drug Delivery and Therapeutic Efficacy

Figure 5. (a) Confocal microscopy images of SKMEL28 cells after 4 h culture in the presence of free DOX·HCl, DOX (TEA treated, hydrophobic DOX), G5/DOX, F-G5-PEG/DOX-1 with an equivalent amount of DOX (2.5 μg/mL). Bar =50 μm; (b) (c) Cell cytometry assay of SK MEL 28 cells after 4 h culture in the presence of free DOX·HCl, DOX, G5/DOX, F-G5-PEG/DOX-1 with an equivalent amount of DOX (5 μg/mL); (d) Cancer cell cytotoxicity were assessed using SK MEL 28 cells. Free DOX· HCl, DOX (TEA treated), G5/DOX, F-G5-PEG/DOX with an equivalent amount of DOX were added into the cell culture medium, respectively. The cell viability was tested after 48 h incubation with

different formulations. (***, p<0.001). (d) Data are expressed as the mean ±

standard deviation.

Drug carriers should be effectively taken up and deliver active drug into the cells.

As DOX is fluorescent (ex/em=490/590), its internalization by SKMEL28 cells

can be monitored by fluorescence microscopy. As shown in Fig 5a, no green

fluorescence (507 nm) was evident from free DOX or G5/DOX. This confirmed

that the green fluorescence must be resulting from the label-free fluorescent

nanocarrier. For F-G5-PEG/DOX-1, a much brighter red fluorescence was

observed (mostly in the nucleus but also in the cytosol) compared to hydrophobic

DOX or G5/DOX. This higher nuclear DOX accumulation could be attributed to

the more efficient cell uptake of the F-G5-PEG/DOX-1, as well as enhanced DOX

release from the endolysosomal compartments to nucleus. We further compared

the nanocarrier and drug uptake between different F-G5-PEG/DOX compositions

via confocal microscopy. The images in Fig S5a showed weaker green and red

signals from F-G5-PEG/DOX-2 and F-G5-PEG/DOX-3 treated cells compared

to F-G5-PEG/DOX-1 treated cells, indicating less cell uptake of both nanocarrier

and drug for F-G5-PEG/DOX-2 and F-G5-PEG/DOX-3. We also noted that DOX

was mainly accumulated in the nucleus from F-G5-PEG / DOX-1 treated cells,

while part of DOX was also distributed in the cytoplasm from F-G5-PEG / DOX-

3 treated cells. The higher nanocarrier uptake of F-G5-PEG/DOX-1 most likely

reflected the relatively smaller size of the particles, which were more easily taken

up by the cells. The higher DOX accumulation in nucleus of F-G5-PEG/DOX-

1treatment was most likely attributed to the relatively higher composition uptake and faster drug release kinetics from the endolysosomal compartments to nucleus.

Flow cytometry was used to quantitatively study cell uptake of the compounds. As shown in Fig 5b and Fig S6b, a higher DOX uptake was achieved by F-G5-PEG/DOX-1 compared to free hydrophobic DOX or G5/DOX (5.2 and 3.7 times, respectively). Nanocarrier and drug uptake between different F-G5-PEG/DOX compositions were shown in Fig S5b-c and Fig S6a-b, F-G5-PEG/DOX-2 and F-G5-PEG/DOX-3 showed 39.2% and 59.7% less nanocarrier uptake and 46.7% and 60.8% less DOX uptake, respectively, than F-G5-PEG/DOX-1. The flow cytometry results showed similar drug and nanocarrier uptake, agreeing with the confocal microscopy results and demonstrating that F-G5-PEG was an efficient drug delivery vehicle for DOX, and F-G5-PEG/DOX-1 was a more efficient nanocomposite for DOX delivery than F-G5-PEG/DOX-2 and -3.

The cytotoxicity of the DOX-loaded F-G5-PEG was quantitatively evaluated in SKMel28 cells by MTT assay. As shown in Fig 5d, F-G5-PEG/DOX-1 showed enhanced cytotoxicity (IC50=0.174 µg), whereas free hydrophobic DOX induced mild cytotoxicity as expected (IC50=0.903µg) reflecting lower solubility in cell culture media (Fig 5d). Biocompatibility experiments revealed that blank F-G5-PEG did not display any cytotoxicity (Fig 3 b and c), thereby demonstrating that cytotoxic effects were only possible when DOX was loaded within the nanocomposites. Most importantly, even at very low DOX concentration (0.5 µg/mL), F-G5-PEG/DOX-1 could still induce an impressive cytotoxic effect (5.7

± 0.5% cell viability) relative to free hydrophobic DOX drug (87.76 ± 3.9 % cell viability), which was comparable to DOX·HCl molecules. The G5/DOX system showed intermediate cytotoxicity (IC50=0.569 µg) compared with other compositions. Combined with the drug uptake investigation, these results, collectively showed that the cytotoxicity was strongly associated with the degree of DOX uptake by the respective formulations, confirming that the intracellular drug concentration was crucial for mediating cell death. We further compared the cytotoxicity between different F-G5-PEG/DOX compositions, as shown in Fig S7, F-G5-PEG/DOX-1 exhibited the best cancer cell toxicity (IC50=0.174 µg) while F-G5-PEG/DOX-3 held the weakest cancer cell toxicity (IC50=0.712 µg) and F-G5-PEG/DOX-2 held intermediate cytotoxicity (IC50=0.305 µg). The higher cytotoxicity of F-G5-PEG/DOX-1 to SKMel28 cells most likely attributed to the higher drug accumulation in nucleus by F-G5-PEG/DOX-1 as the DOX mainly works within nucleus. Here, we have to notice that the burst drug release from F-G5-PEG/DOX-1 (around 45% released from the first 2h) may also cause higher cytotoxicity, it's hard to make conclusion that the observed anticancer activity is resulted from the nanodrug formulation of F-G5-PEG/DOX-1 itself or from the burst release of DOX. However, the much less cell uptake and anticancer activity of hydrophobic DOX to F-G5-PEG/DOX implies that the nano drug delivery system does increase the solubility of hydrophobic drugs. Prospectively, surface cross-linking with biodegradable polymer may be an effective approach to prevent the burst drug release from PAMAM drug delivery

system. Supported by our cell uptake data and cancer cell therapeutic data, we have thereby show that the F-G5-PEG/DOX system may be an improved drug delivery system for DOX for cancer treatment.

3.5 Conclusion

In this study, we successfully produced a new label free fluorescent PAMAM with strong green fluorescence at maximum wavelength ex/em=485/507 nm. The novel fluorescent dendrimer F-G5/F-G5-PEG showed promising biocompatibility and intracellular imaging capability. Anti-cancer drug DOX could be efficiently encapsulated into F-G5-PEG by a solvent-displacement method. It was notable that the drug release characteristics of F-G5-PEG/DOX was pH sensitive and the drug release rate was strongly associated to the initial ratio between TEA and DOX·HCl. Attractively, the F-G5-PEG/DOX system displayed higher cell uptake and more effective therapeutic efficacy than hydrophobic DOX and G5/DOX alone. The high efficiency of this new dendritic drug vehicle suggests that further investigation into their development as carriers is warranted not just for DOX, but also for other clinically important drugs.

Maclean Fellowship for MND Research, Brazil Family Program for Neurology, and the International Macquarie University Research Excellence Scholarship (iMQRES).

Reference:

(1) Ali, U.; Karim, K. J. B. A.; Buang, N. A. *Polymer Reviews* **2015,** 55, (4), 678-705.

(2) Saraiva, C.; Praça, C.; Ferreira, R.; Santos, T.; Ferreira, L.; Bernardino, L. *J. Controlled Release* **2016,** 235, 34-47.

(3) Gothwal, A.; Kesharwani, P.; Gupta, U.; Khan, I.; Cairul Iqbal Mohd Amin, M.; Banerjee, S.; K Iyer, A. *Curr. Pharm. Des.* **2015,** 21, (30), 4519-4526.

(4) Wang, Y.; Guo, R.; Cao, X.; Shen, M.; Shi, X. *Biomaterials* **2011,** 32, (12), 3322-3329.

(5) Esfand, R.; Tomalia, D. A. *Drug Discov. Today* **2001,** 6, (8), 427-436.

(6) Hsu, H. J.; Bugno, J.; Lee, S. r.; Hong, S. *Wiley Interdiscip Rev Nanomed Nanobiotechnol* **2017,** 9, (1), e1409.

(7) Liu, Y.; Chiu, G. N. *Biomacromolecules* **2013,** 14, (12), 4226-4235.

(8) Fu, F.; Wu, Y.; Zhu, J.; Wen, S.; Shen, M.; Shi, X. *ACS Appl. Mater. Interfaces* **2014,** 6, (18), 16416-16425.

(9) White, N. S.; Errington, R. J. *Adv. Drug Delivery Rev.* **2005,** 57, (1), 17-42.

(10) Watson, P.; Jones, A. T.; Stephens, D. J. *Adv. Drug Delivery Rev.* **2005,** 57, (1), 43-61.

(11) Denora, N.; Laquintana, V.; Lopalco, A.; Iacobazzi, R. M.; Lopedota, A.;

Cutrignelli, A.; Iacobellis, G.; Annese, C.; Cascione, M.; Leporatti, S. *J. Controlled Release* **2013,** 172, (3), 1111-1125.

(12) Du, X.; Shi, B.; Tang, Y.; Dai, S.; Qiao, S. Z. *Biomaterials* **2014,** 35, (21), 5580-5590.

(13) Shi, B.; Zhang, H.; Qiao, S. Z.; Bi, J.; Dai, S. *Adv. Healthcare Mater.* **2014,** 3, (11), 1839-1848.

(14) Lee, W. I.; Bae, Y.; Bard, A. J. *J. Am. Chem. Soc.* **2004,** 126, (27), 8358-8359.

(15) Wang, D.; Imae, T. *J. Am. Chem. Soc* **2004,** 126, (41), 13204-13205.

(16) Tomalia, D. A.; Klajnert-Maculewicz, B.; Johnson, K. A.-M.; Brinkman, H. F.; Janaszewska, A.; Hedstrand, D. M. *Prog. Polym. Sci* **2018**.

(17) Tsai, Y.-J.; Hu, C.-C.; Chu, C.-C.; Imae, T. *Biomacromolecules* **2011,** 12, (12), 4283-4290.

(18) Janaszewska, A.; Studzian, M.; Petersen, J. F.; Ficker, M.; Paolucci, V.; Christensen, J. B.; Tomalia, D. A.; Klajnert-Maculewicz, B. *Colloids and surfaces. B, Biointerfaces.* **2017,** 159, 211-216.

(19) Pérez-Sánchez, A.; Barrajón-Catalán, E.; Caturla, N.; Castillo, J.; Benavente-García, O.; Alcaraz, M.; Micol, V. *J. Photochem. Photobiol., B* **2014,** 136, 12-18.

(20) Kim, H. M.; Noh, Y. W.; Park, H. S.; Cho, M. Y.; Hong, K. S.; Lee, H.; Shin, D. H.; Kang, J.; Sung, M. H.; Poo, H. *Small* **2012,** 8, (5), 666-670.

(21) Jevprasesphant, R.; Penny, J.; Jalal, R.; Attwood, D.; McKeown, N.;

D'emanuele, A. *Int. J. Pharm.* **2003,** 252, (1), 263-266.

(22) Luong, D.; Kesharwani, P.; Deshmukh, R.; Amin, M. C. I. M.; Gupta, U.; Greish, K.; Iyer, A. K. *Acta Biomater.* **2016,** 43, 14-29.

(23) Li, Y.; He, H.; Lu, W.; Jia, X. *RSC Adv* **2017,** 7, (25), 15475-15481.

(24) Yu, H.; Nie, Y.; Dohmen, C.; Li, Y.; Wagner, E. *Biomacromolecules* **2011,** 12, (6), 2039-2047.

(25) Wang, Y.; Cao, X.; Guo, R.; Shen, M.; Zhang, M.; Zhu, M.; Shi, X. *Polymer Chemistry* **2011,** 2, (8), 1754-1760.

(26) He, X.; Alves, C. S.; Oliveira, N.; Rodrigues, J.; Zhu, J.; Banyai, I.; Tomas, H.; Shi, X. *Colloids Surf. B. Biointerfaces* **2015,** 125, 82-89.

(27) Abedi-Gaballu, F.; Dehghan, G.; Ghaffari, M.; Yekta, R.; Abbaspour-Ravasjani, S.; Baradaran, B.; Dolatabadi, J. E. N.; Hamblin, M. R. *Appl Mater Today* **2018,** 12, 177-190.

(28) Patri, A. K.; Kukowska-Latallo, J. F.; Baker Jr, J. R. *Adv. Drug Deliv. Rev.* **2005,** 57, (15), 2203-2214.

(29) Kolhatkar, R. B.; Kitchens, K. M.; Swaan, P. W.; Ghandehari, H. *Bioconjugate Chem.* **2007,** 18, (6), 2054-2060.

(30) Cheng, L.; Hu, Q.; Cheng, L.; Hu, W.; Xu, M.; Zhu, Y.; Zhang, L.; Chen, D. *Colloids Surf., B* **2015,** 136, 37-45.

(31) Sanson, C.; Schatz, C.; Le Meins, J.-F.; Soum, A.; Thévenot, J.; Garanger, E.; Lecommandoux, S. *J. Controlled Release* **2010,** 147, (3), 428-435.

(32) Guerrini, L.; Alvarez-Puebla, R.; Pazos-Perez, N. *Materials* **2018,** 11, (7),

1154.

(33) Veronese, F. M.; Pasut, G. *Drug Discovery Today* **2005,** 10, (21), 1451-1458.

(34) Yin, H.; Bae, Y. H. *Eur J Pharm Biopharm* **2009,** 71, (2), 223-230.

(35) Jang, W. D.; Nishiyama, N.; Zhang, G. D.; Harada, A.; Jiang, D. L.; Kawauchi, S.; Morimoto, Y.; Kikuchi, M.; Koyama, H.; Aida, T. *Angew. Chem. Int. Ed.* **2005,** 44, (3), 419-423.

3.6 Supporting Information

Label-free fluorescent poly(amidoamine) dendrimer for traceable and controlled drug delivery

Guoying Wang[a,b], Libing Fu[a,b], Adam Walker [a,e], Xianfeng Chen[f], David B Lovejoy [a], Mingcong Hao[b], Albert Lee [a], Roger Chung [a], Helen Rizos[a], Mal Irvine[a], Meng Zheng[b], Xiuhua Liu*[c], Yiqing Lu* [b,d], Bingyang Shi*[a,b]

[a]Department of Biomedical Sciences, Faculty of Medicine & Health Sciences, Macquarie University, Sydney, NSW 2109, Australia

[b]Henan-MQ joint centre for biomedical Innovation, Henan University, Kaifeng, 475001, China

[c]School of Chemical engineering, Henan University, Kaifeng, 475001, China

[d]Department of Physics and Astronomy, Faculty of Sciences & Engineering, Macquarie University, Sydney, NSW 2109, Australia

[e]Queensland Brain Institute, The University of Queensland, St Lucia, QLD 4072, Australia

[f]School of Engineering, Institute of Bioengineering, The University of Edinburgh, King's Buildings, Mayfield Road, Edinburgh EH93JL, United Kingdom

Fig S1 The TEM image of G5 and F-G5 and F-G5-PEG. G5 was dispersed in methanol. Bar = 100 nm.
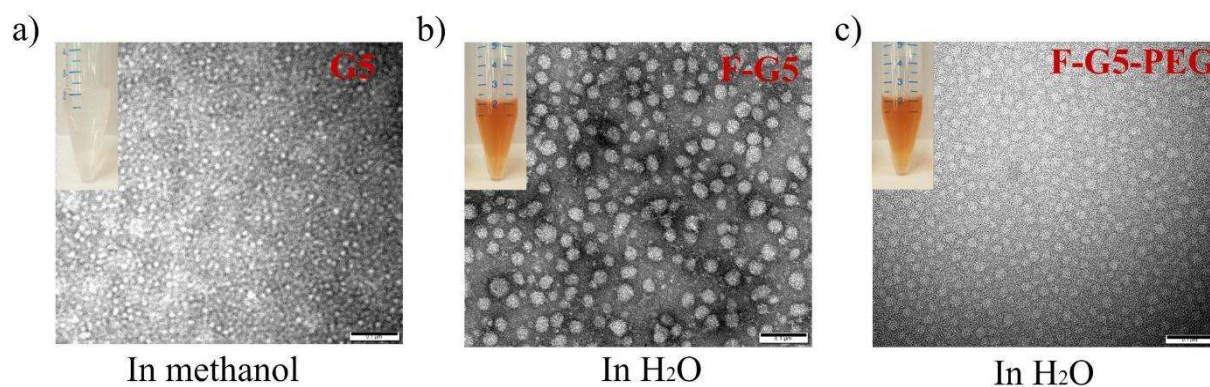
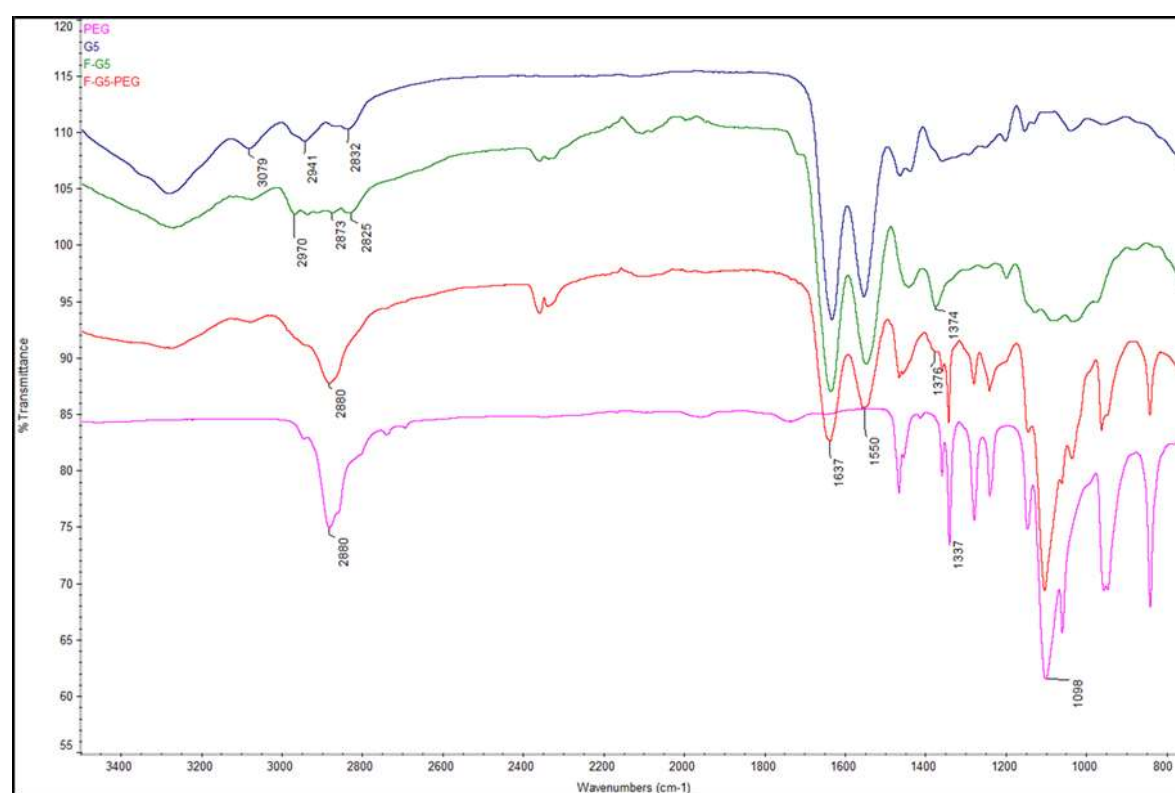Fig S2 The FTIR spectrum for G5, F-G5, F-G5-PEG and PEG$_{2K}$-NHS.

Fig S3. Chemical characterization of aldehyde-modified PAMAM. 1H NMR spectrum of PAMAM-G5,

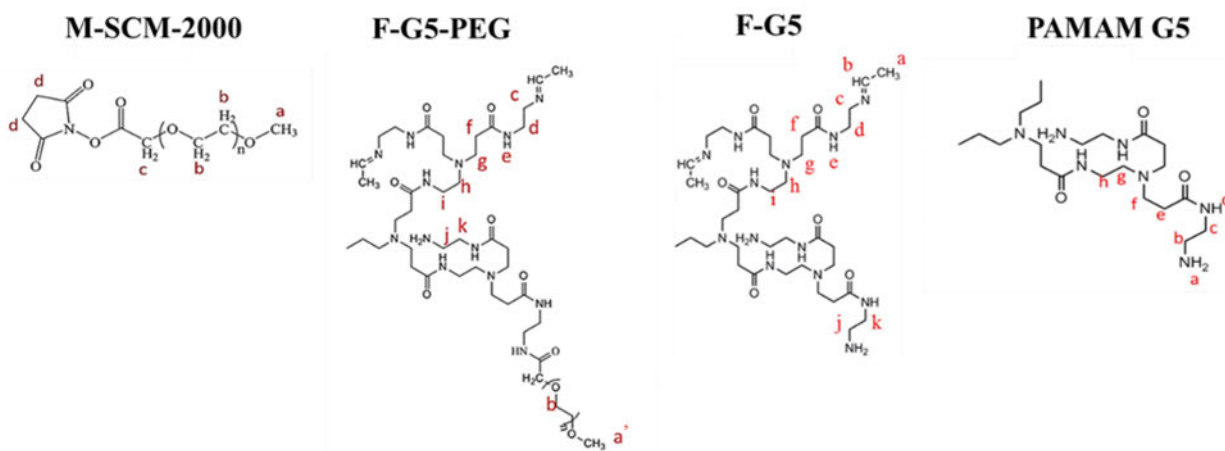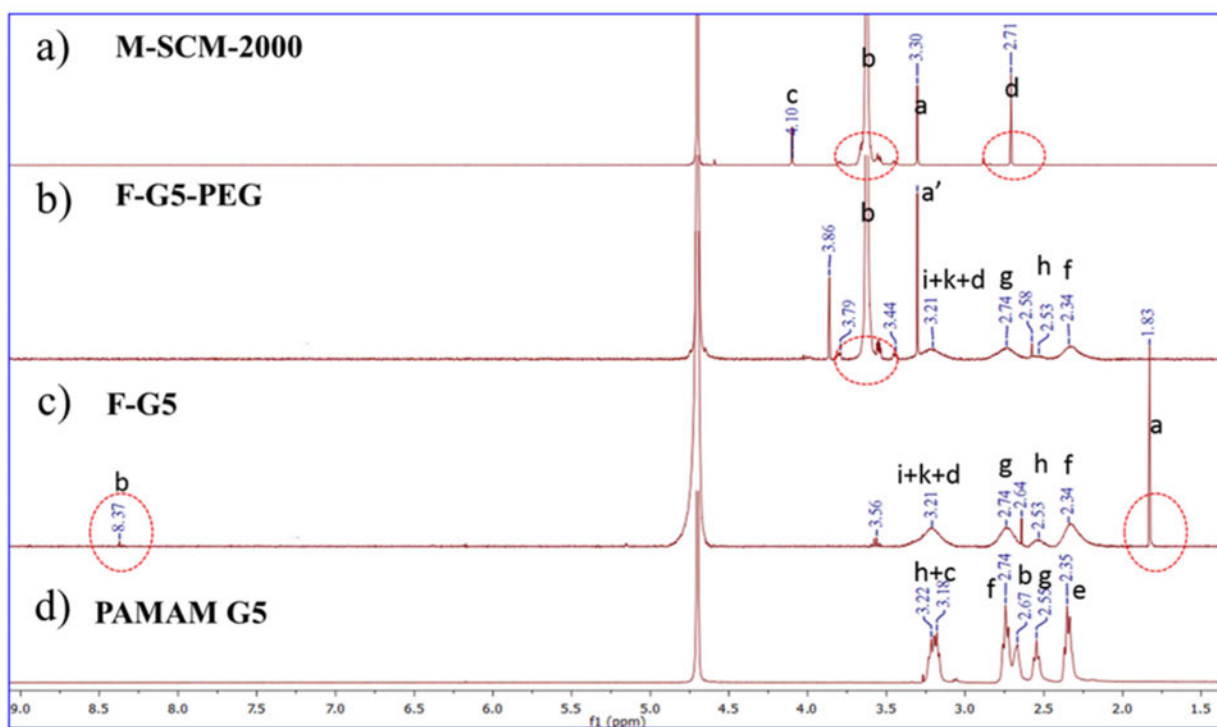M-SCM-2000, F-G5 and F-G5-PEG. Different chemical groups were represented by different alphabets.

Fig S4. (a) The long-term stability of F-G5-PEG in PBS at 37 °C; (b) The fluorescence intensity of F-G5-PEG at different pH value.
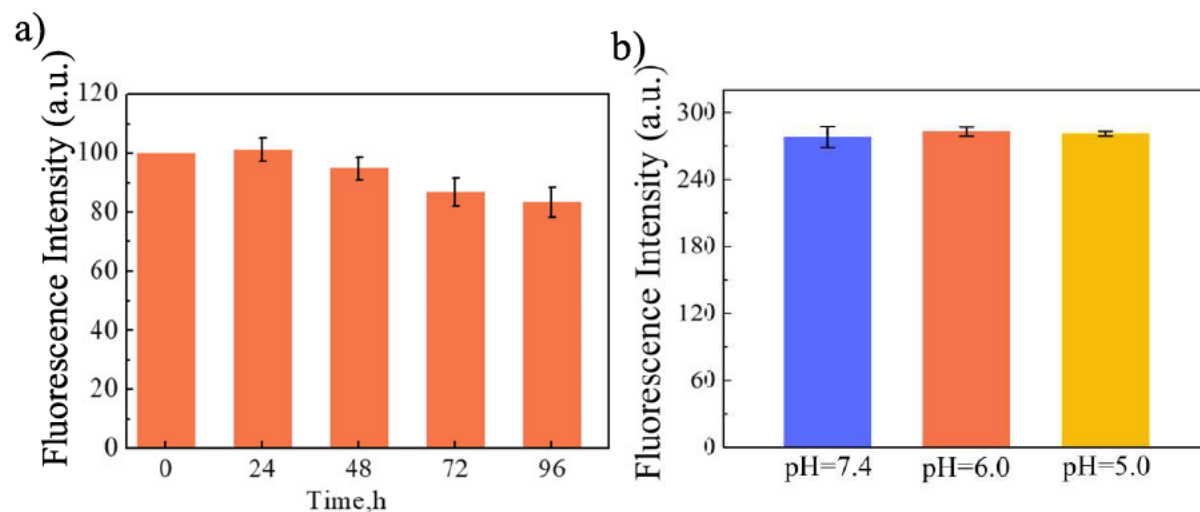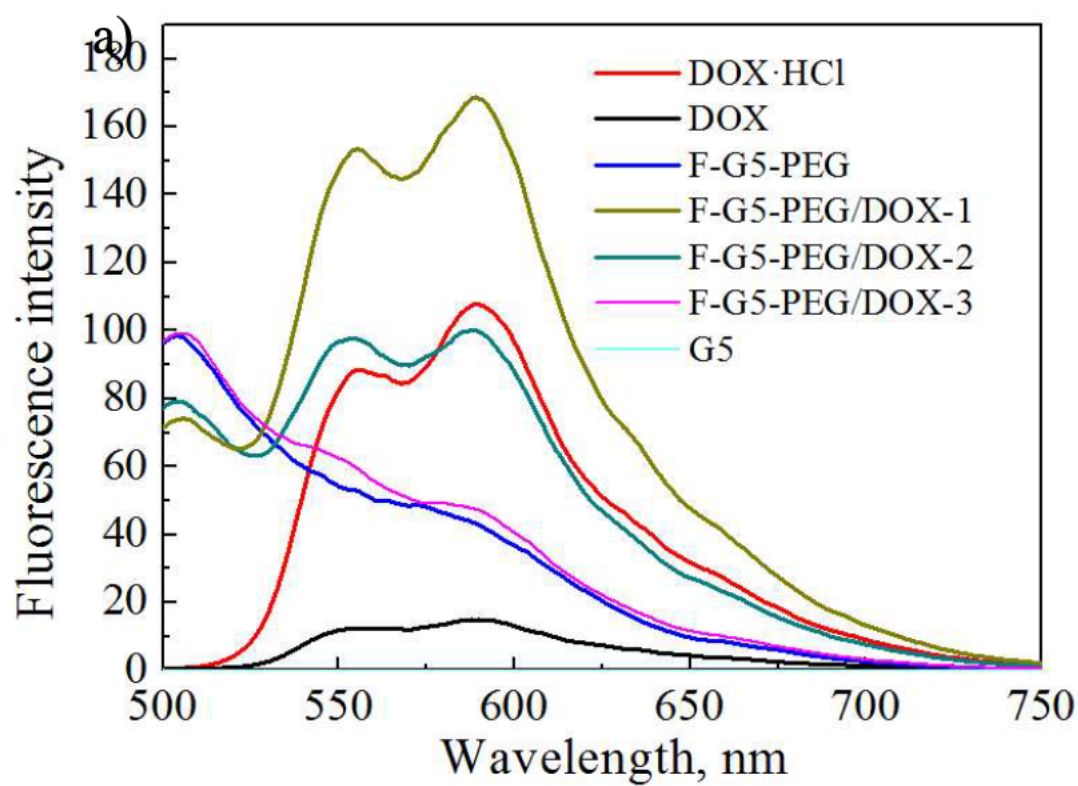
a)

b)

Fig S5. (a) The fluorescent spectrum for free DOX·HCl, free hydrophobic DOX, G5, F-G5-PEG and different F-G5-PEG/DOX compositions. (b) The fluorescence spectrum of F-G5-PEG and F-G5 at the same molar concentration (1 µM).
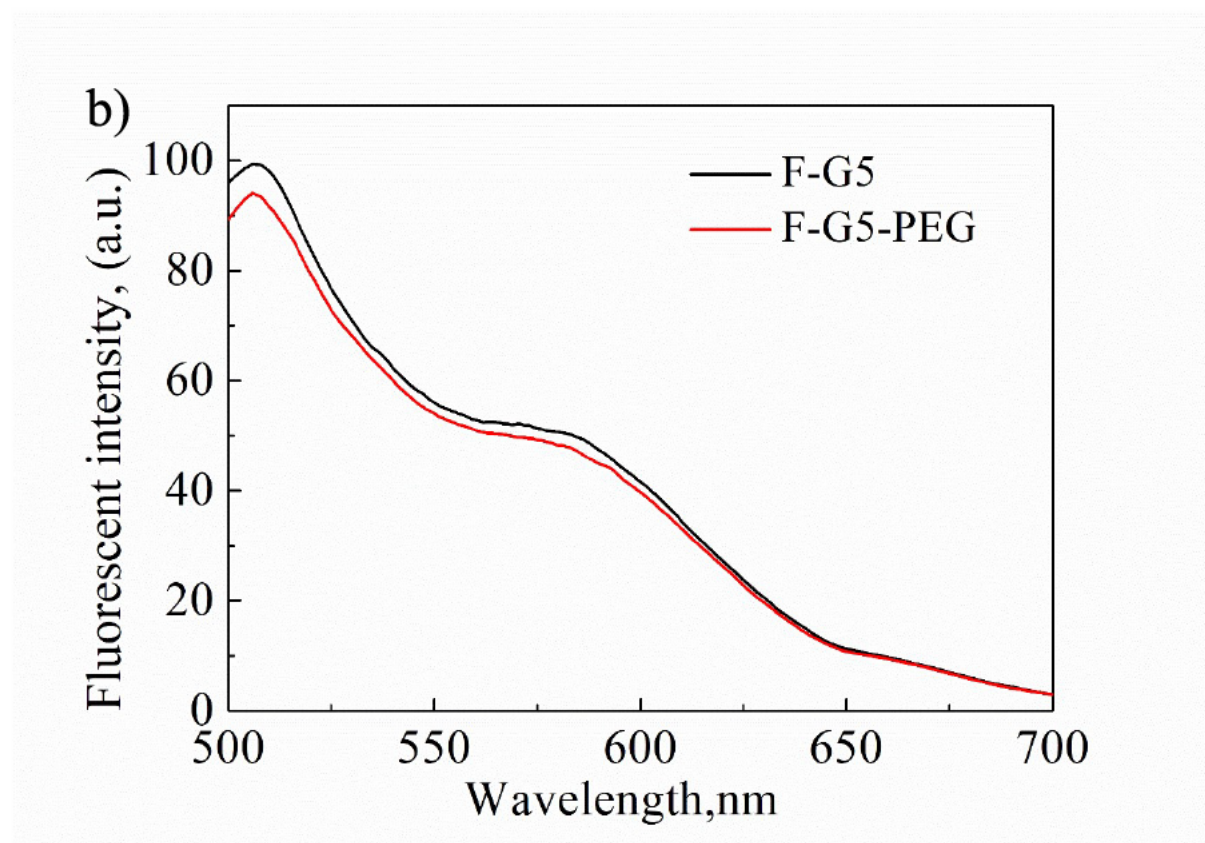
a)

Table S1. The size changes of F-G5/DOX and F-G5-PEG/DOX with 10%FBS

Sample	Size^a, nm
F-G5/DOX	150.8±6.7
F-G5/DOX+10%FBS	356.9±33.7
F-G5-PEG/DOX	97.63±2.7
F-G5-PEG/DOX+10%FBS	63.7±1.7*

a: Statistic by Intensity; *: Two peaks were detected and the data was collected by the second peak.

c: F-G5-PEG/DOX-2 was chosen for serum stability test.

Table S2. The Z-average size distribution of G5, F-G5, F-G5-PEG in PBS.

Sample	Size, nm
G5	11.9±0.7
F-G5	32.5±3.5
F-G5-PEG	31.2±1.3

Fig S6. (a) Confocal images of SKMEL28 cells after 4 h culture in the presence of free DOX· HCl, DOX (TEA treated), G5/DOX, F-G5-PEG/DOX-1/2/3 with an equivalent amount of DOX (2.5 µg/mL). (b) (c) Cell cytometer assay of SKMEL28 cells after 4 h culture in the presence of free DOX· HCl, DOX (TEA treated), G5/DOX, F-G5-PEG/DOX-1/2/3 with an equivalent amount of DOX (5 µg/mL).
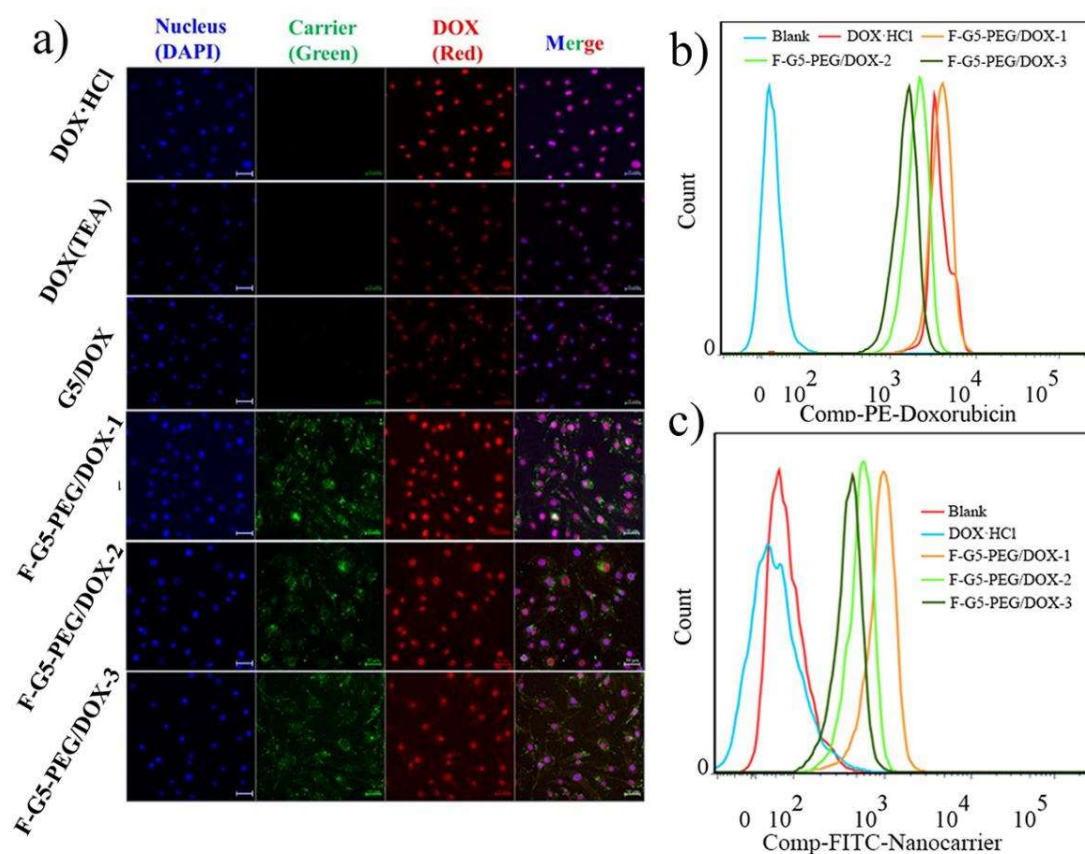

Fig S7. Flow cytometry analysis of the mean fluorescence intensity (MFI) of SKMel28 cells after incubation in the presence of free DOX· HCl, DOX (TEA treated), G5/DOX, F-G5-PEG/DOX-1/2/3

with an equivalent amount of DOX (5 μg/mL). (a) MFI of nanocarrier (FITC Channel); (b) MFI of

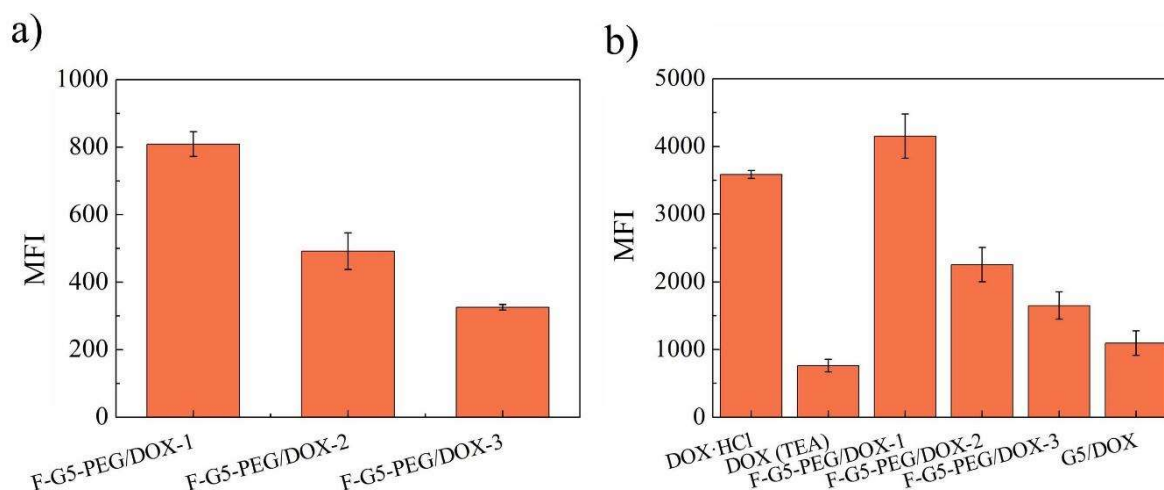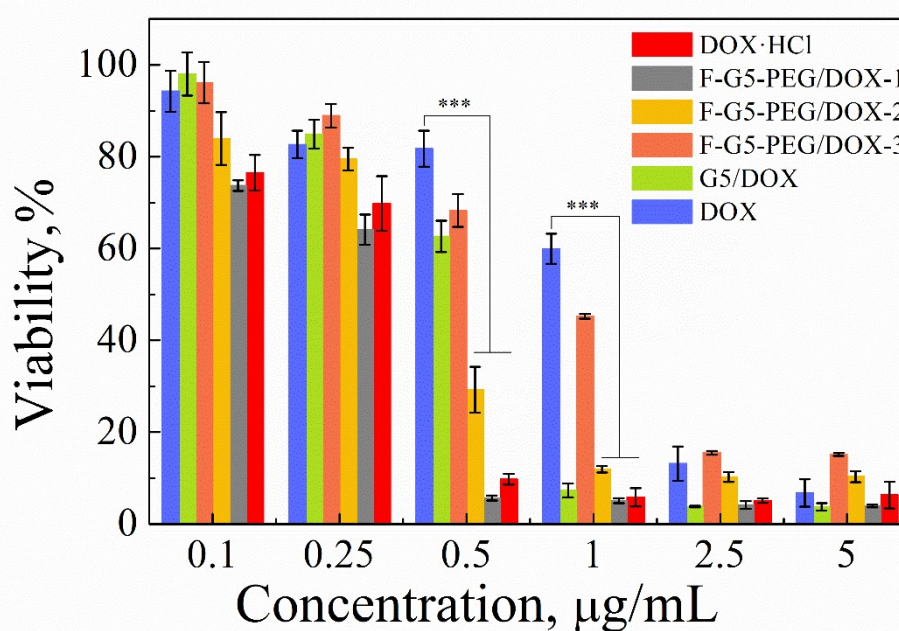DOX (PE Channel). 1×10^4 cells were analysed by flow cytometry system for each sample.

Fig S8. Cancer cell kill ability were tested by SKMEL28 cells. Free DOX· HCl, DOX (TEA treated),

G5/DOX, F-G5-PEG/DOX-1/2/3 with an equivalent amount of DOX were added into the cell culture

medium, respectively. Cell viability was tested after 48 h's incubation with different formulations. (***,

p<0.001).

Chapter 4

Selectively deliver neuron protection drugs to central nervous system (CNS) still remains a great challenge for effective amyotrophic lateral sclerosis (ALS) therapy. To date, the U.S. Food and Drug Administration (FDA) has only approved two drugs that slow ALS progression, albeit modestly: Riluzole and Edaravone. The insufficient brain or spinal cord accumulation and the short half-life of drugs in the blood-stream are the major obstacles that hinder their therapeutic efficiency. In the last few years, the rapid development of nano drug delivery systems has shown great advantages in treating neurodegenerative diseases by prolonging the drug's blood circulation and enhancing the drug's blood-brain barrier penetration. Among numerous nano-drug delivery systems, the PAMAM based drug delivery system is attracting more interesting due to its smaller size, functional surface, monodispersity, and large internal cavity. In chapter 3, we have developed an intrinsically green fluorescent PAMAM (Generation 5, FG5) with excellent fluorescent performance and superior biocompatibility that has been used for drug delivery and intracellular tracking. Due to the intrinsic fluorescence, the intracellular behaviour and CNS targeting capability of FG5 could be easily analysed by flow cytometer and fluorescence microscopy, without additional fluorophore labelling. In this chapter, neuron protection drug Edaravone (EDV) was encapsulated in the FG5 based nanocarriers by a solvent replacement method. To our best knowledge, that's the first time to report PAMAM as a nano-vehicle for neuron protection drug delivery,

thus providing the basis for developing PAMAM based nanomedicines for ALS treatment. To assess the CNS targeting capability, transferrin (Tf) was selected as a transport ligand to facilitate the BBB penetration of the FG5. The BBB transportation and neuron protection function of FG5/EDV nanocomplexes were evaluated by the *in vitro* BBB model and motor neuron cells model.

Through the study in this chapter, we further verified that as nanocarrier and nanoprobe FG5 could be successfully applied to transport neuron protection drugs, and *in vitro* results suggested that transferrin functionalization can enhance drugs neuroprotective effect and promote the nanocarriers blood-brain barrier penetration. Therefore, through the systematic study in this chapter, we provided data support for further application of the FG5 based drug delivery system in *in vivo* models (e.g. SOD1 mouse model, TDP-43 mouse model).

4.1 Contribution to this paper

	G.Y	L.F	B.S	N.S	A.W	R.C
Experiment Design	•		•			
Sample Preparation	•	•		•		
Data Collection	•					
Analysis	•			•		•

Manuscript	•		•	•	•	•

This manuscript has been prepared to submit to *Advanced Healthcare Materials*. In this manuscript, I undertook the majority of jobs from the literature review, experiment design to the final manuscript writing (>80%). My supervisor Dr. Bingyang Shi has given me great support in terms of experiment design and manuscript revising. Other people contributed to data collection, sample analysis, and manuscript revising were very helpful for this work.

Intrinsically Fluorescent PAMAM Dendrimer as Drug Carrier for Neuron Protection Study

Guoying Wang[a,b], Libing Fu[a,b], Bingyang Shi*[a,b], Nima Sayyadi[c], Roger Chuang[a], Adam Walker[d]

[a] Department of Biomedical Sciences, Faculty of Medicine & Health Sciences, Macquarie University, Sydney, NSW 2109, Australia

[b] Henan-Macquarie University joint center for Biomedical Innovation, Henan University, Kaifeng, 475001, China

[c] Department of Chemistry and Biomolecular Sciences, Macquarie University, Sydney, New South Wales 2109, Australia

[d] Queensland Brain Institute, The University of Queensland, St Lucia, QLD 4072, Australia

Abstract

Amyotrophic lateral sclerosis (ALS), is a rapidly progressed neurodegenerative disease that mainly affects motor neurons in the brain and spinal cord, which results in losing the control of muscle and eventual paralysis [1]. Excessive production of reactive oxygen species (ROS) in diseased motor neurons has been considered an important hallmark of ALS. Current ALS treatment Edaravone (EDA) is a drug well known for its antioxidant function. However, EDA can only modestly slow down the progression of the disease which is largely caused by the insufficient central nervous system (CNS) drug accumulation and the short half-life. The rapid development of nanotechnology in recent years has shown great potential of delivering more clinical drugs to CNS to promote therapeutic effect of those drugs. Herein, we developed an intrinsically fluorescent

poly(amidoamine) (PAMAM) (FGP) and surface functionalized with transferrin (FGP-Tf) to achieve traceable brain-targeted drug delivery. In this study, we fabricated EDA loaded FGP/EDV and FGP-Tf/EDV nano-complexes and tested their neuron protection and BBB penetration capabilities via *in vitro* cell models and BBB models. The demonstrated enhanced blood brain barrier (BBB) transportation and elevated neuron protection function of FGP-Tf/EDV in *in vitro* models, providing a basis for further evaluation the therapeutic effect of those nanomedicines in ALS animal models.

4.2 Introduction

Selective targeting of motor neuron protective drugs to the central nervous system (CNS) remains a great challenge for effective ALS therapy [2]. Firstly, most of the therapeutic agents cannot be delivered to the CNS due to the existence of blood-brain barrier (BBB) and blood spinal cord barrier (BSCB), the physical and biological barriers that only allow small and lipid molecular cross the tight junction [3]. Secondly, the short circulation half-life of the therapeutic agents attenuates their therapeutic efficacy [4-5]. Thirdly, the therapeutic drugs not only reached the desired sites but also to distribute into normal tissues, thus reducing the concentration of drugs in the brain and spinal cord and may also causing side effects [6]. To meet the requirement of effective ALS therapy, a promising strategy is to develop multifunctional nanomaterial drug delivery systems [7-8]. Thanks for the well-defined structure, functional surface groups, superior monodispersity,

and really small size, poly(amidoamine) (PAMAM) dendrimers are widely used as nanocarriers for drug/gene delivery to target CNS [9, [10]]. However, to our best knowledge, there is no study has been reported in using PAMAM to deliver motor neuron protective drugs to treat ALS. Therefore, to evaluate the neuron protection and CNS targeting features of PAMAM based drug delivery system is valuable for developing PAMAM based nanomedicines for ALS treatment.

Multifunctional imaging technologies to monitor the delivery and biodistribution of PAMAM based nanomedicines *in vitro* and *in vivo* will significantly benefit their applications in the field of ALS study. Thus, many efforts have been engaged to achieve visual detection of PAMAM dendrimers, most commonly through covalent attachment of fluorophores such as FITC, Cy5 onto a dendritic scaffold [11-12]. However, fluorophore-conjugated PAMAM dendrimers may affect the surface structure, size, biocompatibility, and solubility of the conjugates. Additionally, fluorophore-conjugated PAMAM dendrimers are tending to be prone to photobleaching that limits their application for imaging and real-time tracking. Thereby we developed an intrinsic green fluorescent PAMAM (FG5) by modifying PAMAM generation 5 with acetaldehyde. The fabricated FG5 exhibited superior advantages to traditional fluorophore labelled PAMAM in terms of structure stability, bio-compatibility, and photo-stability [13]. Those unique properties enable FG5 to be promising nanocarriers and nanoprobes that can be applied for ALS therapeutic drugs delivery and real-time tracking.

In this study, the second FDA approved ALS treatment Edaravone (EDV) was chosen as the drug model since EDV is well known for its antioxidant function. It protects nerve cells by clearing damaging reactive oxygen species (ROS) in the body [14]. To facilitate the BBB/BSCB penetration of EDV loaded FG5 system, transferrin (Tf, iron-binding blood plasma glycoproteins, MW $\approx$ 76 kDa) was selected as a transport ligand since the transferrin receptor (TfR) is abundantly expressed in the brain capillaries endothelial cells and have been widely used for receptor-mediated transportation of nanomaterials to pass through BBB [15-17]. The proposed pathway of the Tf functionalized FG5/EDV nanocomplexes (FGP-Tf/EDV) to pass through the blood-brain barrier (BBB), and the way they exerted functions in the brain were described in Scheme 1. As shown, the BBB penetration of FGP-Tf/EDV could be enhanced via receptor-mediated transportation. After penetrating the BBB, part of FGP-Tf/EDV would be further absorbed by neurons. The released EDV in brain tissue fluid and neurons can eradicate excessive ROS, thus achieving neuron protection. In this study, the enhanced neuron protection and elevated BBB penetration capability of FGP-Tf/EDV systems were achieved via *in vitro* motor neuron cells model and *in vitro* BBB model, thus providing the basis for further investigation of FGP-Tf/EDV system in ALS animal models.
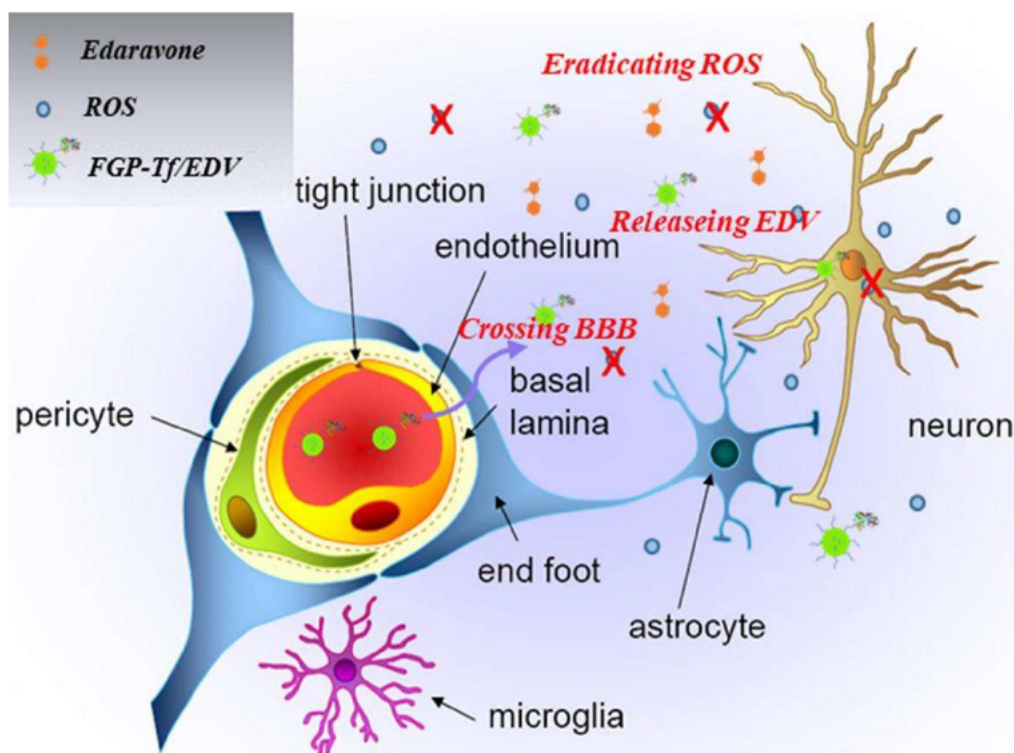
Scheme 1. The schematic illustration of the pathway of FGP-Tf/EDV to pass through the blood-brain barrier (BBB) and the way of them exert functions in the brain.

4.3 Results and discussion

4.3.1 Physical and optical properties

FG5 was prepared according to our previous report [13]. In further working with FG5, we found that after subsequent processing (storing of FG5 at RT for a month), the fluorescence intensity of FG5 was enhanced up to around 45% at the maximum emission peak (507 nm) (Fig 1A). The insert in Fig 1A showed the visualise fluorescent colour of initial FG5 (upper) and long-term stored FG5 (lower) under 488 nm laser excitation, which has changed from dark brown to deep yellow. The same fluorescent behaviour was also observed after heating of

FG5 in aqueous solution at 60 ºC overnight. It was believed that long-term storage of FG5 promoted the oxidation of internal tertiary amines in PAMAM, and these tertiary amines played an important role in forming fluorescence-emitting fragments [18-19], which was evidently induced by oxygen in the air and aqueous solution. However, FG5 may undergo degradation after heating [20]. Thus long-term oxidated FG5 as drug carrier and nanoprobes was chosen for further utilization.
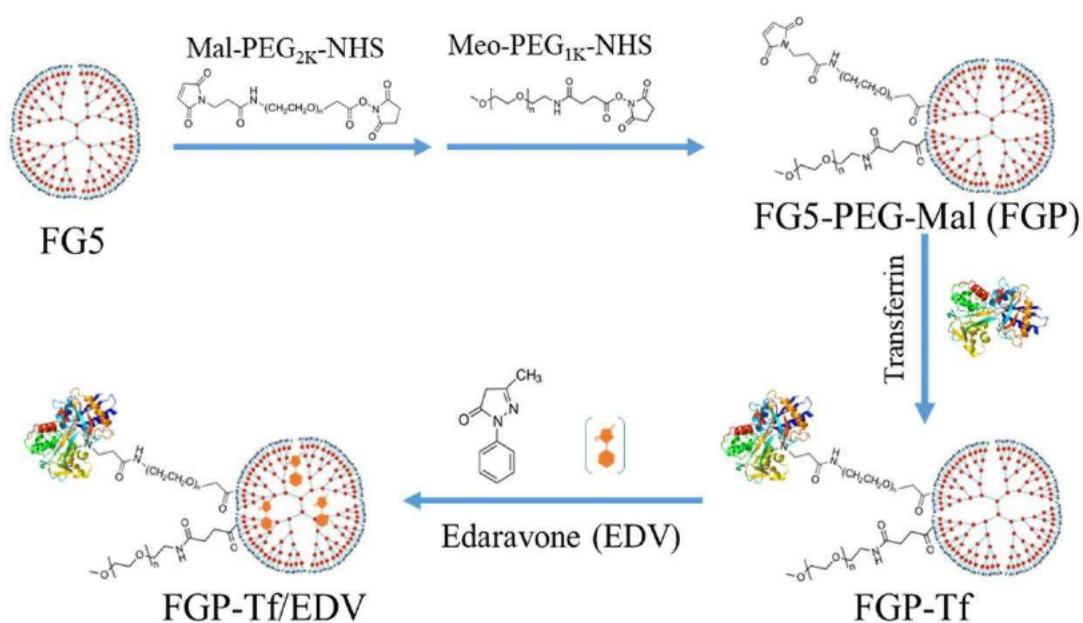
Scheme 2. The synthetic route of Transferrin-functionalized drug carrier and the drug loading approach.

Transferrin functionalized PAMAM dendrimers (FGP-Tf) were prepared according to the previous report [6]. The synthetic route of FGP-Tf and the way of EDV loading were described in Scheme 2. Briefly, Mal-PEG$_{2K}$-NHS and Meo-PEG$_{1K}$-NHS were firstly conjugated on the surface of FG5 and purified by

ultrafiltration. Simultaneously, Tf was thiolated by 2-Iminothiolane hydrochloride (Traut's reagent), after purification over 85% yield of Tf was obtained. The number of thiol groups was quantified as 2.5 per Tf through Ellmann's Reagent assay. The thiolated Tf was then conjugated to the maleimide activated FGP, and the product (FGP-Tf) was purified by size exclusion column (SEC) (Superose™ 6 increase column). As shown in Fig 1B, the retention time for the elution peak of FGP-Tf from the SEC was shorter than that of FGP and Tf, indicating the successful conjugation of Tf to FGP. The conjugation of maleimide activated FGP to thiolate Tf was also confirmed by the UV spectrum, which showed a protein specific peak at 280 nm (Fig 1C). The structure of different polymeric was confirmed by ^{1}H NMR spectra (Fig S1), as shown, the appearance of the chemical shifts of FG5 at 8.37 and 1.83 ppm was contributed to -N=CH- and -CH$_3$ groups respectively, which revealed the successful reaction of acetaldehyde with terminal amino groups of PAMAM G5. A new peak at 3.64 ppm corresponded to -CH$_2$-CH$_2$- segments that existed in PEG, indicating the successful incorporation of NHS-PEG-Mal to FG5. In addition, a small peak emerged at 6.80 ppm was assigned to the MAL group that can be used for further conjugation of transferrin. Meanwhile, the NHS specific chemical shift peak at 2.73 ppm was disappeared, suggesting the complete reaction of NHS with FG5. Furthermore, according to the integral of the proton signals at 1.83 ppm (-CH3) and amide group (-CH$_2$-CO-NH$_2$-, 2.24–2.38 ppm) in PAMAM dendrimer, about 33.5 % amino groups were reacted with aldehyde that leaving enough free amino groups for further

PEGylation. FTIR spectra of different chemical structures were further obtained. As shown in Fig S2, the chemical shifts at 1374, 2873, and 2970 cm^{-1} of FG5 were assigned to $-CH_3$ group, suggesting the successful incorporation of $–N=CH-CH_3$ groups. The C-O-C repeat segments from PEG that assigned to peak 2880 and 1098 cm^{-1} were shown in FG5-PEG FTIR spectra, revealing the successful coupling of PEG to FG5. The similar excitation and fluorescent emission spectra from FGP and FGP-Tf were shown in Fig 1D, which demonstrated a maximum excitation at 495 nm and maximum emission at 507 nm. The particle size of FGP-Tf was measured around 14 nm, slightly larger than that of FGP (~7 nm), as determined by dynamic light scattering (DLS) (Fig 1E), further confirming the successful conjugation of Tf to FGP as the increased size was close to the size of free Tf (8 nm measured by DLS). The surface charge of FGP-Tf was changed to -5.2 mV, which was more likely because the negatively charged transferrin neutralized the positively charged amino groups on FGP (Fig 1F).

As described in Scheme 2, the FDA approved ALS drug Edaravone (EDV) was efficiently encapsulated into FGP and FGP-Tf by a solvent-displacement (precipitation) method [13]. The size and zeta-potential of FGP/EDV and FGP-Tf/EDV were obtained through the DLS (Fig 1E, F). As shown, a slight size increase of drug-loaded FGP and FGP-Tf (FGP/EDV, FGP-Tf/EDV) was observed, which was potentially caused by the encapsulated drugs that changed the stretch conditions of the PAMAM. Additionally, the surface charge of FGP/EDV changed from positive to negative, and FGP-Tf/EDV displayed a large

increase in the absolute value of negative charge, which may also be caused by the drug loading procedure and encapsulated drugs that changed the structure stretch of PAMAM molecules.
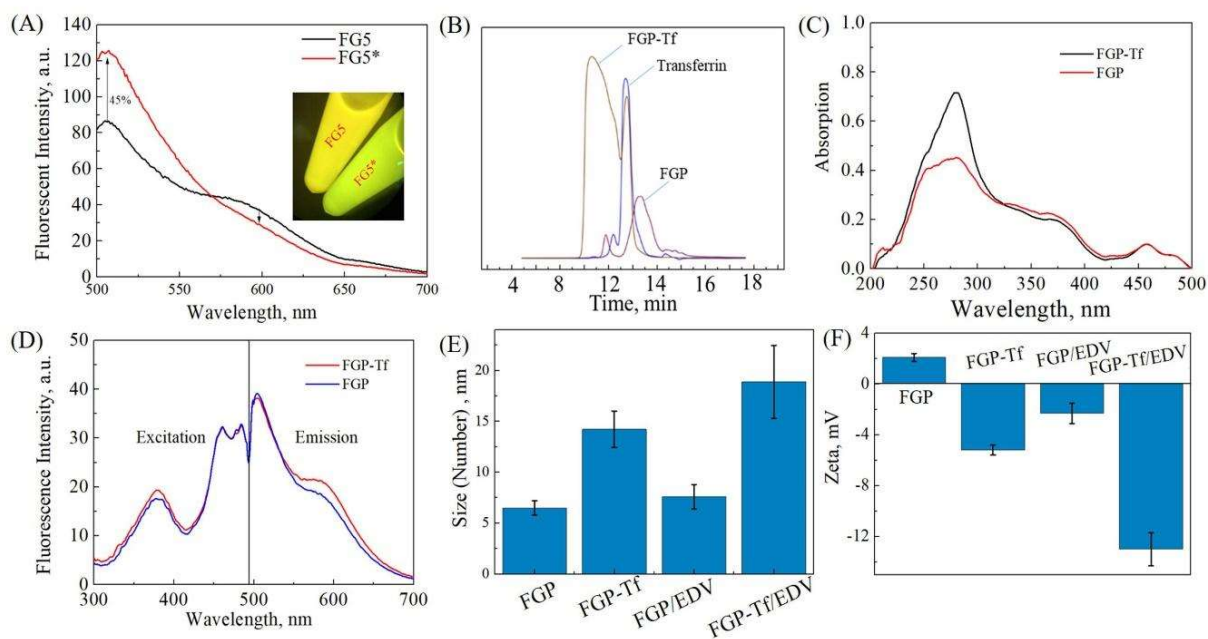

Figure 1 (A) Fluorescence spectrum of initial FG5 and oxidated FG5 (FG5*). Insert shows the visualize fluorescent images of initial FG5 (upper) and oxidizing FG5 (lower) under 488 nm laser excitation. (B) Gel filtration chromatogram of FGP, Tf and FGP-Tf. (C) UV-vis spectra of FGP-Tf was seen in all band scanning. Characteristic absorbance peak at 280 nm indicated the presence of Tf. (D) Fluorescence spectrum of FGP and FGP-Tf. (E) (F) Size and Zetapotential distribution of FGP, FGP-Tf, FGP-Tf/EDV and FGP/EDV.

4.3.2 Biocompatibility of FGP and FGP-Tf

For neurodegeneration disease therapy, the nanocarriers should have low or no cytotoxicity to healthy cells. The biocompatibility PEGylated FG5 (FGP) and transferrin functionalized FG5 (FGP-Tf) was evaluated using CCK-8 assays [21] in motor neuron like cells (NSC-34) and human brain blood vessel endothelial cells (hCMEC/D3). The CCK-8 results were shown in Fig S3, both cell lines have shown over 90% cell viability after treating with FGP and FGP-Tf at the concentration range of 12.5-100 μg/mL, indicating that those nanocarriers have excellent biocompatibility for motor neuron drugs delivery.

4.3.3 Drug loading and release

The amount of loaded EDV in nanocarriers was acquired by testing the un-loaded EDV through UV-Vis spectroscopy measurement and shown in Table S1. FGP-Tf and FGP showed similar drug loading efficiency, suggesting that the surface modification with Tf did not largely change the drug loading behaviour of FGP. To effectively scavenge ROS, the encapsulated EDV should be released into the desired region to exert its effect [22]. To predict the release behaviour, we studied the cumulative release of EDV in PBS solution (pH 7.2). As shown in Fig S4, after a boost release at the first 2 h, the rest EDV was gradually released from FGP-Tf/EDV or FGP/EDV in PBS solution and the total released drug reached 80% after 24 h, while the free EDV undergo a burst release that almost all drugs have diffused into the release buffer within 1 h. The drug release rate from FGP-

Tf/EDV was slower than FGP/EDV, which may be caused by the outer protein that slowed the diffusion of drug from internal space to external fluid. The drug release profile from FGP/EDV or FGP-Tf/EDV revealed that those neuron protection drugs could be effectively released from nanocarriers, and the controlled drug release manner may benefit the drugs retention time in blood circulation.

4.3.4 Cellular uptake of FGP/EDV and FGP-Tf/EDV

To cross the BBB and target motor neurons, the nanocarrier/drug complex should be effectively taken by blood vessel endothelial cells and neuron cells [23]. Therefore, we tested the cellular uptake of FGP-Tf/EDV and FGP/EDV by NSC-34 and hCMEC/D3 cells. The confocal images of cells after treatment with FGP-Tf/EDV or FGP/EDV were shown in Fig A-a and Fig B-a, as shown, the FGP-Tf/EDV treated cells presented higher green signals (nanocarriers) than FGP/EDV treated cells for both cell lines. To quantify the difference, we further carried out flow cytometry assay. As shown in Fig 2A-b,c and Fig 2B-b,c, the hCMEC/D3 and NSC34 cells presented 1.6 times and 1.4 times higher cellular uptake of FGP-Tf/EDV, respectively than that of FGP/EDV. To confirm if free Tf will affect the cellular uptake of drug loaded nanocomplexes, we further found that pre-incubation with free Tf (1 mg/mL) for 1 h decreased the uptake of FGP-Tf/EDV while only slight affect the uptake of FGP/EDV (Fig 2). The decreased cellular uptake of FGP-Tf/EDV was likely caused by the fact that the free Tf blocked part

of the Tf receptor, resulting in the decreased binding efficiency of FGP-Tf to the

Tf receptor on cell membrane, thus reducing the cell endocytosis. Those cellular

uptake results suggested that the surface functionalization with transferrin indeed

enhanced the endocytosis of those PAMAM/drug nanocomplexes for both

endothelial cells and neuron cells, which may facilitate their capability of passing

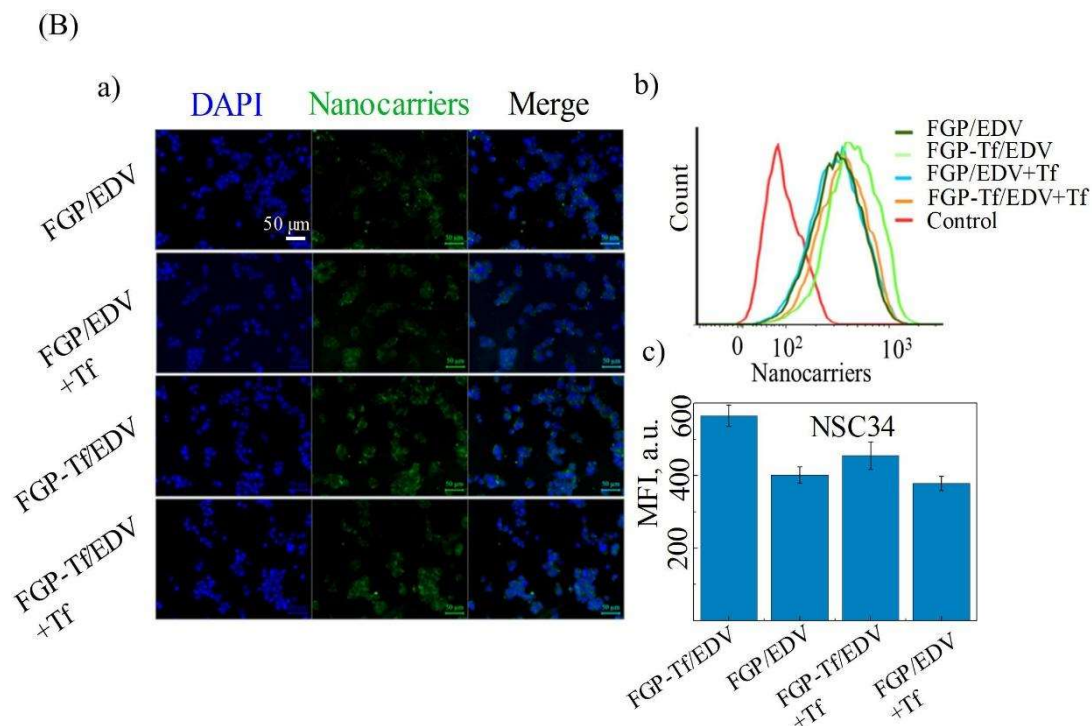through the blood-brain barrier and targeting neuron cells.
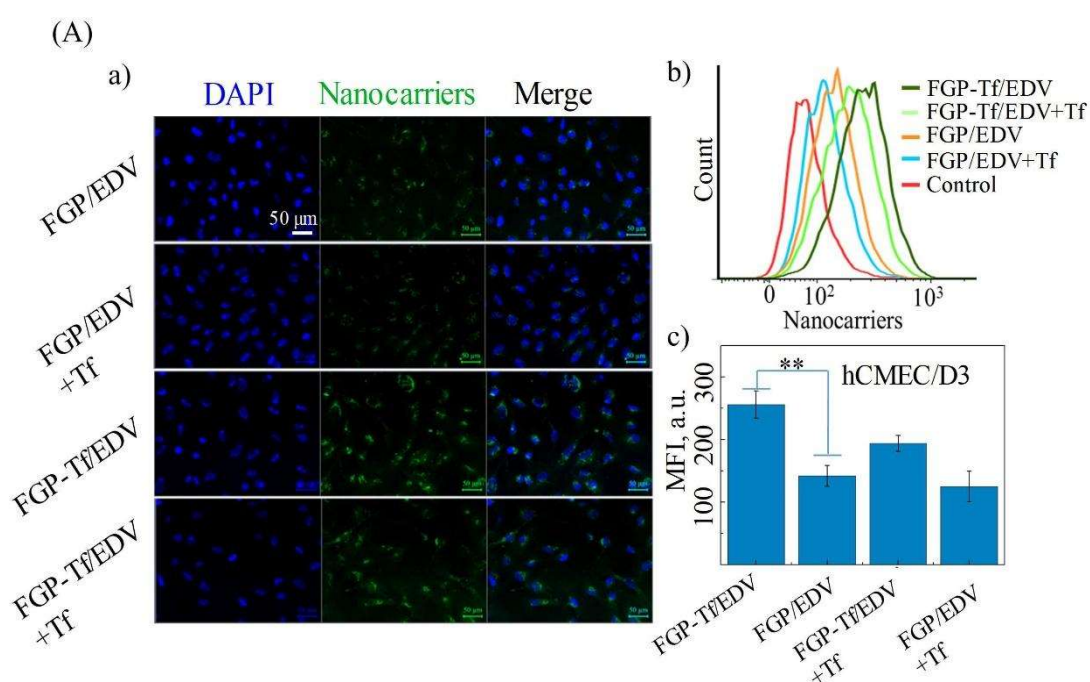
Figure 2 Cell uptake of FGP and FGP-Tf by hCMEC/D3 and NSC34 cells. Fluorescent microscopy images of hCMEC/D3 (A-a) and NSC34 (B-a); Cell flow spectra of cell uptake with hCMEC/D3 (A-b) and NSC34 (B-b); Statistic result of cell uptake with hCMEC/D3 (A-c) and NSC34 (B-c). The FGP and FGP-Tf used for cell uptake were kept at an equal concentration at 1.7 mM. The significant difference was performed to compare the cellular uptake between FGP/EDV and FGP-Tf/EDV. (**) for $p < 0.01$. MFI =Mean fluorescent intensity.

4.3.5 Neuron protection study

In order to estimate the protective effect of FGP/EDV and FGP-Tf/EDV, CCK-8 assay was performed to measure cell viability. The cell viability of the control group was considered as 100%. As seen in Fig 3A, the percentage of apoptotic

cells treated with hydrogen peroxide (H_2O_2) showed concentration depended manner. We chose H_2O_2 concentration at 0.25 mM that caused around 30% cell apoptosis for further testing the protection effect of EDV loaded nanocomplexes. As shown in Fig 3B, The FGP/EDV, FGP-Tf/EDV, and free EDA pre-treatment clearly decreased H_2O_2-induced apoptosis, and the protective effect was presented in a dose-dependent manner. There was no large difference between free EDV and EDV loaded nanocomplexes at lower concentration (2.5~5 mg/mL), but FGP-Tf/EDV showed slight enhancement in protecting neurons at higher concentration (10, 15 mg/mL), which was mainly like contributed by the higher cellular uptake of FGP-Tf that facilitated drug accumulation inside the cells.
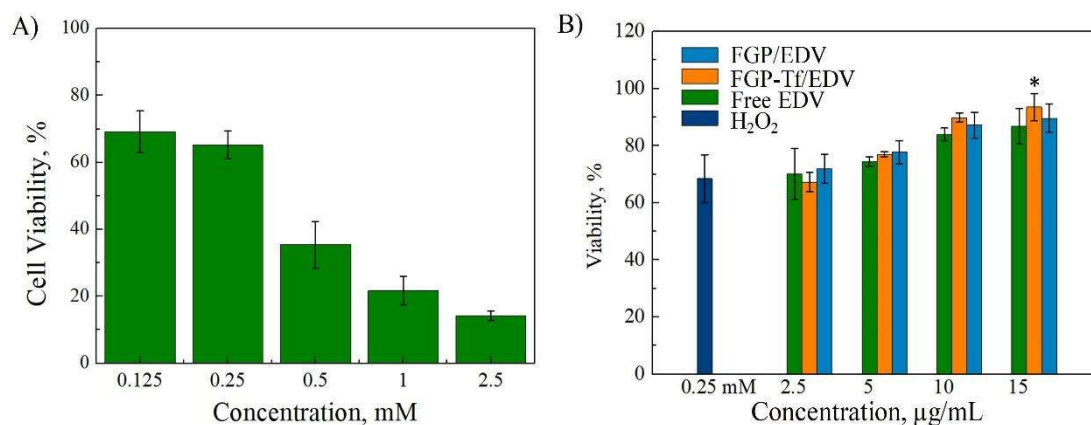

Figure 3 Protection effect from H_2O_2-induced cell apoptosis. (A) Cell viability of NSC-34 after treating with different concentrations of H_2O_2. (B) Protection effect of EDV, FGP/EDV, or FGP-Tf/EDV to NSC-34 cells against H_2O_2-induced oxidative stress. The significance level was set as 0.05, and the data indicated was performed to compare the neuroprotection efficiency between EDV, FGP/EDV, and FGP-Tf/EDV. (*) for $p<0.05$.
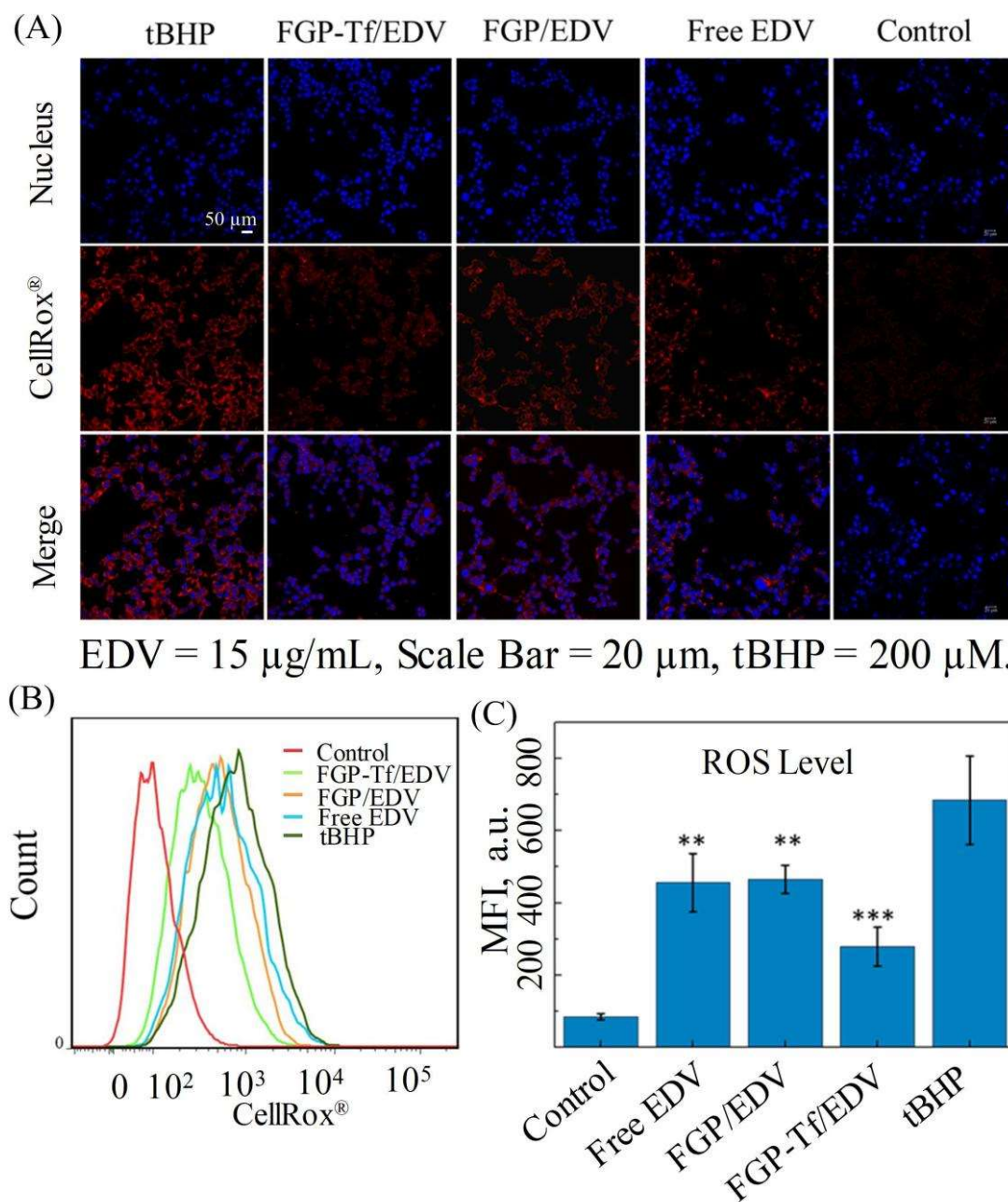
Figure 4. Intracellular ROS level evaluation. NSC-34 cells were pre-treated with FGP-Tf/EDV, FGP/EDV, and free EDV for 4 h with the equal EDV concentration at 15 µg/mL before treating with tBHP (200 µM). (A) Fluorescence microscopy observation of intracellular ROS induced by tBHP; (B, C) Cell flow evaluated the intracellular ROS level induced by tBHP. The significance level was set as 0.05

and the data indicated was performed to compare the ROS level between positive control and EDV, FGP/EDV, and FGP-Tf/EDV treated cells. (**) for p<0.01. (***) for p<0.001. MFI : Mean fluorescent intensity.

The excessive production of ROS, combined with lacking oxidant eliminating mechanisms has been recognized as the major pathogenesis of ALS [24], [25]. To elucidate the effects of FGP/EDV and FGP-Tf/EDV on tBHP-induced (tert-Butyl hydroperoxide (tBHP) an organic peroxide widely used in a variety of oxidation processes) oxidative stress, the produced ROS levels in NSC-34 cells were determined by using the CellROX® deep red fluorescence probe according to the manufacture instruction. After exposing the NSC34 cells to tBHP for 30 min, the generation of ROS was imaged by a confocal microscope. As shown in Fig 4A, the tBHP treated cells showed dramatically increase of ROS signal (Red) compared with control, which means the tBHP can effectively generate ROS. Cells pre-treated with EDV or EDV loaded nanocomplexes showed reduced ROS signal (red) to the negative control (only tBHP treated cells). Particularly, cells pre-treated with FGP-Tf/EDV presented the largest red signal decline. To quantify this intracellular ROS level change, the cells were further analyzed by flow cytometer. As seen in Fig 4 B, C, the FGP/EDV-Tf pre-treated NSC-34 cells showed around 57.2% decrease in ROS level compared to the negative control, which was higher than free EDV (34.2 %) and FGP/EDV (35.7%). Combined with the confocal images and cell flow results, those data revealed that the pre-treatment with free EDV or EDV loaded nanocomplexes can effectively eradicate

the excess ROS, esspecially, pre-treatment with FGP-Tf/EDV possessed the highest efficiency. The cells treated with only nanocarriers did not show any ROS eradicating capability (Fig S5), indicating that the reduced intracellular ROS was mainly attributed to the intracellular EDV. The highest neuron protection from FGP-Tf/EDV may be induced by the highest cellular uptake that facilitated the intracellular drug accumulation (Fig 2), which enabled more drugs to exert effect in motor neuron cells. Additionally, the PAMAM carriers also provided a protection shell to the encapsulated EDV by reducing the auto-oxidation rate of drugs, as we found that the efficiency of free EDV underwent dramatically decreased after long time storage while the FGP/EDV or FGP-Tf/EDV complex still kept protection efficiency to motor neurons (data was not shown).

4.3.6 In vitro BBB penetration study

The major obstacle that hinders nanomaterials into the brain and spinal cord is the presence of blood-brain barrier (BBB) and blood spinal cord barrier (BSCB) [26], *in vitro* BBB models are widely used as useful tools to evaluate and predict the penetration properties of nanocarriers into the central nervous system (CNS) [27-28]. *In vitro* BBB model was built by using hCMEC/d3 monolayer and confirmed by the TEER value (bbb model was ready to use when TEER value was no longer changes, ~60 $\Omega \cdot cm^{-2}$)[29], the structure of *in vitro* BBB model was shown in Fig 5A, media were taken out from abluminal site for intensity test. The transportation ability of different carriers across BBB model was shown in Fig 5B

in which FGP-Tf/EDV presented a higher transportation rate than FGP/EDV group for all time points. After 24 h incubation, the transportation ratios were 13.6 % for FGP-Tf, 9.8 % for FGP, respectively, indicating that the Tf targeting carrier possessed stronger transportability to cross the BBB compared to the carriers without targeting group. We also measured the TEER value of monolayer cells after 24 h of nanocomposite treatment, and only observed a slight decrease in TEER value (from 60.5 $\Omega \cdot cm-2$ to 57.2 $\Omega \cdot cm-2$). These data indicated that nanocomposites had only a slight impact on the integrity of the in vitro BBB model, and the transport of these nanoparticles from the apical side to basolateral site was mainly contributed by the transcytosis/extravasation. The enhanced BBB penetration of FGP-Tf/EDV was probably induced by the transferrin receptor-mediated transportation that enables more particles to pass through endothelial monolayer.
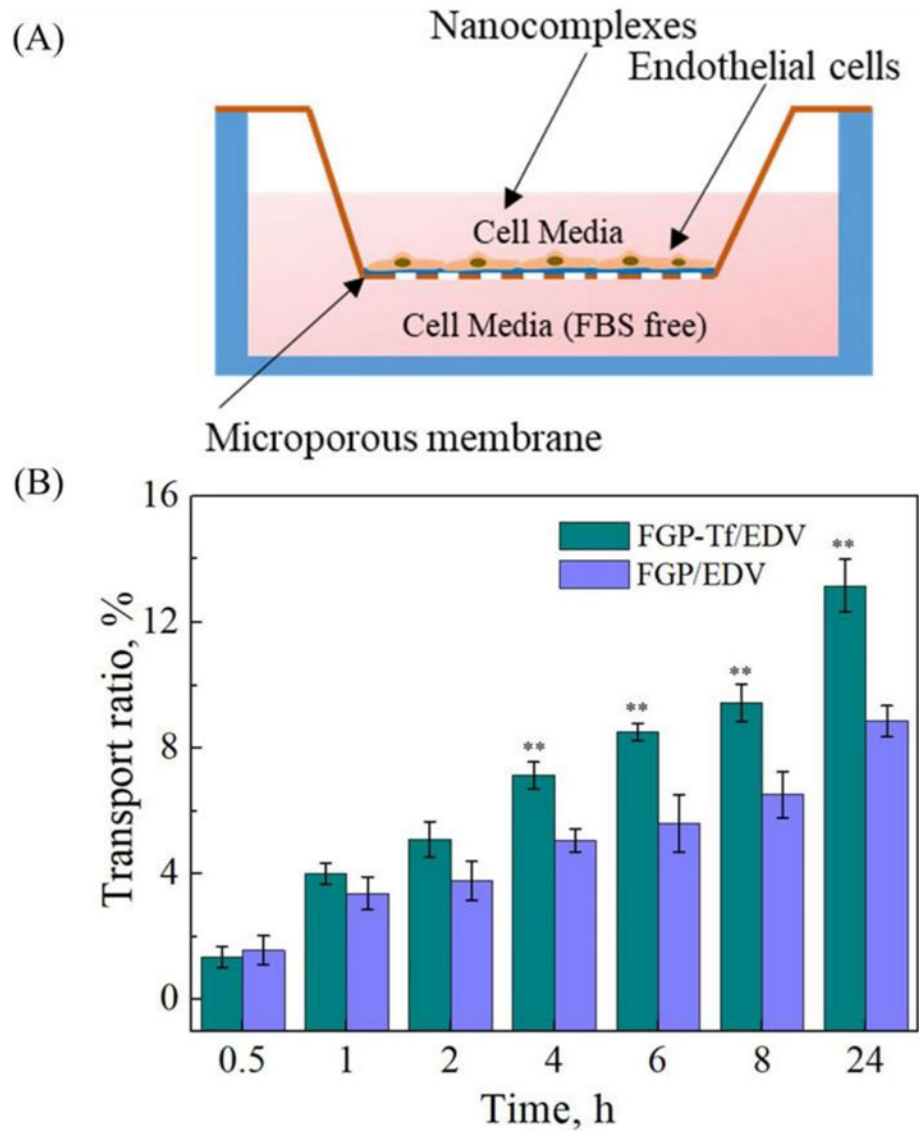
Figure 5. (A) The structure of the *in vitro* BBB model. (B) The transport ratio of FGP/EDV and FGP-Tf/EDV across the BBB during 24 h (30 min, 1h, 2 h, 4 h, 6 h, 8 h, 24 h). The significant level was set as 0.05 and the data indicated was performed to compare the BBB penetration rate between FGP/EDV and FGP-Tf/EDV, (**) for $p<0.01$.

4.4 Conclusion

The delivery of therapeutic drugs, trophic factors, and biomacromolecules across the blood-brain barrier and blood spinal cord barrier of ALS remains a challenge for the disease [30-31]. The rapid development of nanotechnologies in therapeutic and diagnosis of neurodegeneration diseases has opened a gate for the nanomaterials-based strategy for ALS treatment [31-32]. Therefore, we engaged an intrinsically green fluorescent PAMAM (FG5) as nanocarrier and nanoprobes that can simultaneously realize drug delivery and real-time tracking. The fabricated FG5 showed enhanced emission intensity, excellent biocompatibility and superior photo-stability that enabled it capable of being tracked in real-time. Enhanced blood-brain barrier (BBB) transportation and elevated neuron protection function was achieved by FGP-Tf/EDV drug delivery system, suggesting that this novel brain intrinsically fluorescent drug delivery system has a great potential toward clinical therapeutic drugs in ALS treatment and warranted for further investigation in animal models.

4.5 Experimental section

4.5.1 Materials

PAMAM dendrimer, ethylenediamine core, generation 5.0 solution (PAMAM G5), acetaldehyde, holo-Transferrin human, O-[(N-Succinimidyl)succinyl-aminoethyl]-O'-methylpolyethylene glycol (Ome-PEG$_{1K}$-NHS, MW=750), 2-Iminothiolane hydrochloride, tert-Butyl hydroperoxide solution (tBHP) and

hydrogen peroxide solution (30% in H_2O) were acquired from Sigma-Aldrich (NSW, Australia). *O*-[N-(6-Maleimidohexanoyl) aminoethyl]-*O*-[3-(N-succinimidyloxy)-3-oxopropyl] polyethylene glycol (NHS-PEG$_{2K}$-Mal; MW=2000) was obtained from Jenkem Technology (Beijing, China). CellROX™ Deep Red Reagent was purchased from ThermoFisher Scientific (Sydney, Australia). Cell Counting Kit 8 (WST-8 / CCK8) was purchased from Abcam (ab228554) (NSW, Australia). Ultra Centrifugal Filters (Amicon® with different MW Cut off = 10, 30 and 100 KD) were purchased from Merck Millipore (VIC, Australia). PD-10 Desalting column and Superose™ 6 increase column was purchased from GE Healthcare Life Science (VIC, Australia).

4.5.2 Synthesis of FG5

The intrinsically green fluorescent PAMAM was synthesized according to previous report [18]. Typically, 50 mg (3.5 mmol) G5 was added to 5 mL of Milli Q water, followed by adjustment of the pH to 10 by NaOH solution (100 mM). Excess amount of acetaldehyde (acetaldehyde: terminal amino groups = 30 : 1, mol/mol) was added in a dropwise fashion to the G5 solution, and the reaction was kept stirring for 8 h at room temperature. After 8 h reaction, the solution colour changed to brownish red. The product was then purified through dialysis against distilled water for 24 h to remove unreacted acetaldehyde. The purified product (FG5) was concentrated (add the concentration e.g. M or mg/mL) and stored at fridge (4 °C) as stock solution.

4.5.3 Synthesis of FGP-Tf

The as-prepared purified FG5 dendrimers were reacted with MAL-PEG$_{2K}$-NHS in PBS (adjusted to pH = 8.0 with 0.1M NaOH) with a ratio of FG5 to MAL-PEG-NHS 1:6 (mol : mol) at RT for 1 hr. Then the excess amount of Ome-PEG$_{1K}$-NHS was added to the above reaction mixture at a ratio of FG5 to Ome-PEG$_{1K}$-NHS 1:10 (mol/mol) and the reaction was continued for another 1 h. After that, the product FG5-PEG-MAL/Ome was purified trough ultrafiltration (Amicon® Ultra Centrifugal Filters, 10KD) with PBS buffer (pH = 7.2) to remove unreacted PEG reagents and exchanged to the buffer pH to 7.2. Thiolated Tf was then prepared according to the previous report [6]. Briefly, 10 mg Tf (0.13 mM) was dissolved in 1 mL PBS (adjusted to pH = 8.0), then 0.7 mg 2-iminothiolane hydrochloride (5 mM) in 1 mL PBS (pH = 8.0) was added to Tf solution and the mixture was kept stirring for 1 h at RT. The thiolated Tf was then purified through a PD-10 Desalting column (Sephadex G-25) to remove unreacted impurities. Then the thiol groups on Tf were specifically coupled to the peripheral maleimide of FGP in PBS (pH = 7.2) at a ratio of 2:1 (Tf to PAMAM, mol/mol) for 4 h at RT and then kept 4 °C overnight. The final product (FGP-Tf) was purified by the gel filtration using a Superose™ 6 increase column and NGC™ Medium-Pressure Liquid Chromatography System (Bio-Rad).

4.5.4 Encapsulation of Edaravone within FGP-Tf

EDV was encapsulated inside the FGP and FGP-Tf using a solvent-displacement (nanoprecipitation) method. 0.15 mmol of the as-prepared FGP or FGP-Tf was added in 3 mL of Tris buffer (0.01M, pH=7.2), while 4.5 mmol (0.8 mg) EDV was dissolved in 0.1 mL methanol. Then, the EDV solution was added dropwise to the FGP or FGP-Tf solution. This was followed by magnetic stirring of the reaction mixture overnight to allow evaporation of the methanol for drug loading. The FGP/EDV and FGP-Tf/EDV solutions were purified by ultrafiltration through an Amicon® Ultra Centrifugal Filter (weight cut-off membrane of 3KDa) to remove and collect free non-capsulated EDV. The free EDV was collected, followed by quantification of the UV-vis absorbance peak of EDV at 261 nm (The maximum UV-vis absorption peak was determined at 261 nm).

4.5.5 Characterization

Size and Zeta (ζ) potential of FG5, FGP, and FGP-Tf were measured using a Malvern Zetasizer APS instrument (Malvern, Australia). Transmission electron microscopy (TEM) image of FGP-Tf was captured by CM10 (Philips) system. Samples were negatively stained with Uranyl Acetate Replacement Stain (UAR-EMS). Fluorescent spectra were acquired by fluorospectro photometer (Fluorolog spectroscopy, Horiba). Fluorescent intensity was recorded by FlexStation 3 (Sydney, Australia). UV-vis absorption spectra were acquired by UV-Vis spectrophotometer (UV-2600, Shimadzu). Fourier transform infrared (FTIR)

spectra were obtained by NICOLET 6700 spectrometer (Thermo Scientific). ^{1}H nuclear magnetic resonance (^{1}H NMR) (400 MHz Bruker) was performed to record the proton chemical shifts; samples were prepared in deuterated water (D_2O).

4.5.6 Drug Release Study

2 mL of PBS (pH = 7.2) solution containing FGP-Tf/EDV and FGP/EDV (equal EDV amount of 50 μg) nanocomposites were separately transferred into a dialysis tube (molecular weight cut-off (MWCO)=10,000) and sealed, followed by placing the dialysis tube into 10 mL PBS buffer (pH = 7.2). The entire drug release system was settled in a constant-temperature and vibrator (vibrational speed = 200 rpm, temperature = 37 °C). At each time point, 2 mL release buffer was taken out for measurement, followed by supplementary adding 2 mL fresh PBS to keep the volume constant. The concentration of EDV was determined by a UV-vis spectrometer that measured the EDV absorbance peak at 261 nm. The cumulative release (Cr) of EDV was recorded according to the following equation [13].

$$Cr = Wt/Wo \times 100\% .$$

Wt represented the cumulative amount of released EDV at each predetermined time point, Wo represented the total amount of loaded EDV in the PAMAM carriers.

4.5.7 Cell Culture

NSC34 (Mouse Motor Neuron-Like Hybrid Cell Line) cells were cultured in Dulbecco's Modified Eagle's Medium (DMEM) and supplemented with 10% fetal bovine serum (FBS), 100 U/mL penicillin, and 100 U/mL streptomycin. hCMEC/D3 (human brain endothelial capillary) cells were continuously cultured with EMB^{TM}-2 medium (Lonza) by supplementary adding with 5% FBS, 100 U/mL streptomycin and 100 U/mL penicillin. Cells were cultured in a CO_2 (5%) incubator (ThermoFisher) and maintained at 37 °C, followed by replacing media every 2~3 days.

4.5.8 Cytotoxicity Test

NSC-34 and hCMEC/D3 cells were cultured in 96-well plates (Costar$^®$) at density of 5000 cells/well (Cells were counted by Scepter™ 2.0 Cell Counter, Merck). After inoculation, the cells were maintained in CO_2 incubator overnight to allow cells to adhere to the plate bottom. To test the biocompatibility of nanocarriers, cell culture media containing FGP or FGP-Tf were added to the wells to obtain the final concentration in the range of 12.5 to 100 μg/mL. Next, the cells were kept growing in CO_2 incubator for another 24 h before 10 μL CCK-8 was added to each well. After 2 h incubation with CCK-8, the cell viability was determined based on the absorption of media at 450 nm. For neuron protection efficacy test, 10 μL cell culture media containing FGP/EDV, FGP-Tf/EDV, and free EDV (2.5, 5, 10, 15 mg/mL equal EDV concentration) were added into

microplate wells that culturing NSC-34 cells. Experiments were carried out in triplicate. The cells were pre-incubated with free drugs or nanocarrier/drug complexes for 4 h in cell incubator, then H_2O_2 (add amount) was added into each well to obtain the final concentration of 250 mM, and the cells were allowed to be further incubated for 24 h. The cell viability was tested by CCK8 kit as the previous description.

4.5.9 Intracellular Drug Delivery

To evaluate the intracellular drug delivery, 1 mL NSC34 or hCMEC/D3 cells were seeded into 6-well plates that loaded with cover glasses at a concentration of 1×10^5 cells/well (Cells were counted by Scepter™ 2.0 Cell Counter, Merck) and maintained in CO_2 incubator overnight. Next, cell culture media containing FGP/EDV, FGP-Tf/EDV were added to cell wells to reach a final concentration of 1.5 mM. The hCMEC/D3 cells and NSC34 cells were then incubated at 37 °C for 2h and 4h, respectively. Next, cells were washed with PBS three times to remove the unabsorbed nanoparticles. For cellular imaging, the cells were fixed with 4% formaldehyde (PFA) for 15 min, followed by washing with PBS three times. Finally, cell slides were mounted with VECTASHIELD® mounting medium (with DAPI) and imaged by laser-scanning confocal microscope (LSCM, Zeiss LSM 880). To quantify the cell uptake of diverse nanocarriers, the cells were subsequently digested by Trypsin-EDTA (0.25%) (Gibco). After collection, the cells then dispersed in 0.5 mL 4 wt% formaldehyde at 4 °C overnight. Next, cells

were washed and redispersed in PBS for flow cytometer (BD LSR Fortessa X-20) assay. To evaluate if free transferrin will affect the cell uptake of those noncomplex, we pre-incubate the NSC34 and hCMEC/D3 cells with free transferrin (1mg/mL) for 1 h, then equal molecular FGP/EDV, FGP-Tf/EDV (0.15 mM) were added to cell culture media, the cells were treated and analyzed as above description.

4.5.10 Detection of Intracellular ROS Generation

NSC34 cells were seeded at a concentration of 1×10^5 cells/well in 24-well plates that loaded with glass cover slides and maintained in CO_2 incubator overnight. After that, cell culture media were replaced with media containing free EDV, FGP-Tf/EDV, and FGP/EDV at the equal EDV concentration at 15 μg/mL. Next, cells were incubated with different drug/PAMAM nanocomplexes for 30 min in CO_2 incubator. Subsequently, tBHP diluted in cell culture media were added in each well to reach the concentration of 200 μM, followed by further incubating at 37 °C for 30 minutes. Next, CellROX® reagent diluted in cell culture media was added to each well to reach the concentration of 5 μM, followed by further incubating for 30 minutes. Subsequently, cells were washed three times with PBS and fixed in 4% PFA for 10 minutes. Cell slides were mounted with VECTASHIELD® mounting medium (with DAPI) and imaged by LSCM (Zeiss LSM 880). To qualify the intracellular ROS level, NSC34 cells were seeded in a 12-well at a concentration of 2×10^5 cells/well and maintained in CO2 incubator

overnight. After that, cells were treated with the above description. The ROS level was obtained through the flow cytometer (BD LSR Fortessa X-20) at APC channel.

4.5.11 In vitro BBB penetration

BBB model was established according to the method as previously described [6]. hCMEC/d3 cells were seeded into the inserts (BD Falcon Cell Culture Inserts, 1.0 μm pore size) at a density of 7.5×10^4 cells/well and allowed to grow for 3~5 days. Especially, the media in pates were serum-free while the media in the inserts was supplemented with 10% FBS and 1% antibiotics. The media were changed every 2 days. The TEER value of the BBB model was measured daily until the value reached over 65 $\Omega.cm^2$ and remained stable. Next, 0.15 mM FGP/EDV or FGP-Tf/EDV was added in the insert, 200 μL media at the abluminal side were taken out for measurement at different time intervals. The fluorescent intensity was recorded by a microplate reader (Flexstaion 3, Australia).

4.5.12 Statistical Analysis

The significance level was determined by One-way ANOVA analysis by using the software Origin 8.0. The data of (*) represented $p<0.05$, (**) represented $p<0.01$, and (***) represented $p<0.001$. Each experiment was done in triplicate (n = 3).
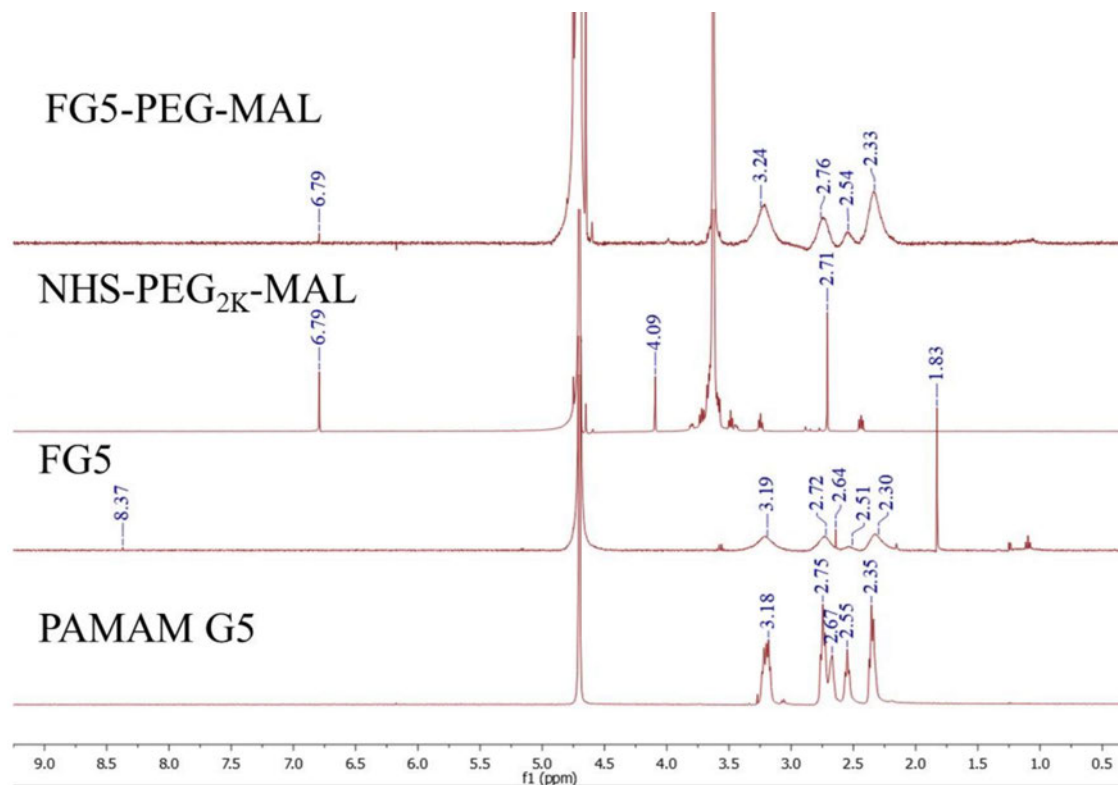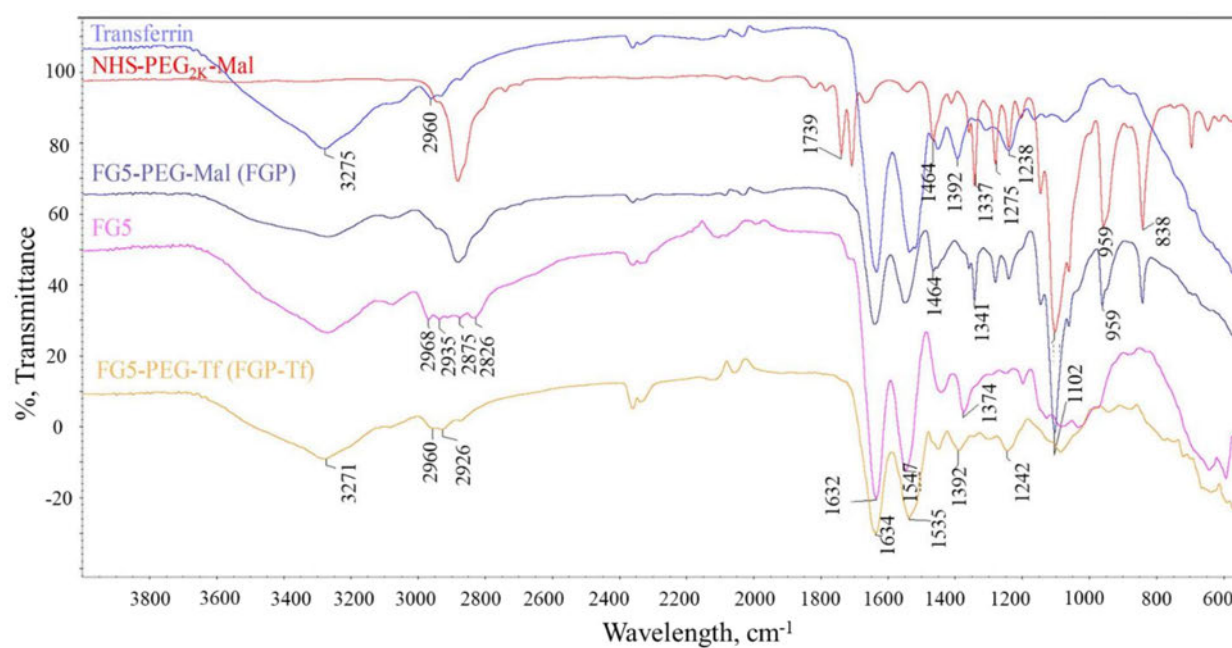
4.6 Supporting Information

Figure S1, ^{1}H NMR of different chemical structure
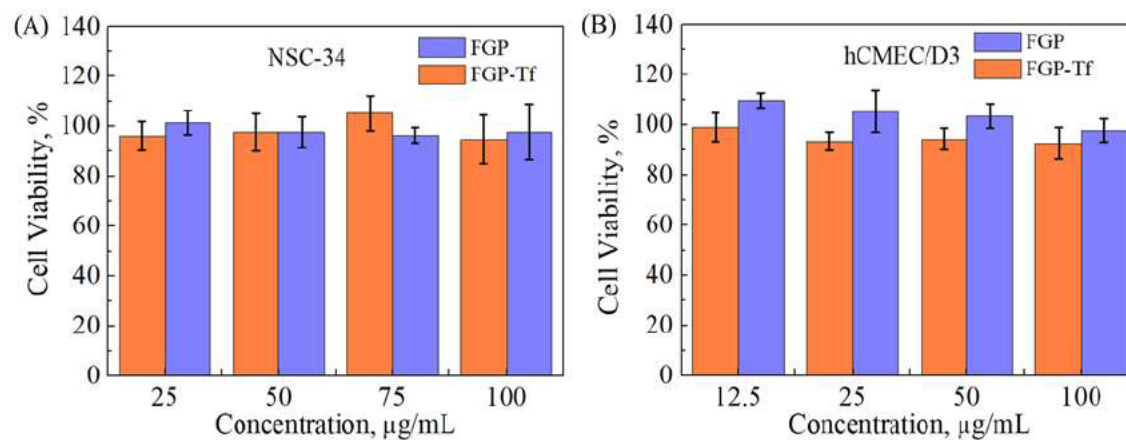
Figure S2, FTIR of different chemical structure

Figure S3 Cell cytotoxicity assay by (A) NSC-34 cells (motor neuron-like cells) and (B) hCMEC/D3 cells (human brain endothelial cell line).

Table S1 Drug loading efficiency

Sample	Carrier weight	EDV Weight	EE, % [a]
FGP-EDV	2 mg	0.8 mg	20.8±3.2
FGP-TF-EDV	2 mg	0.8 mg	25.4±3.4

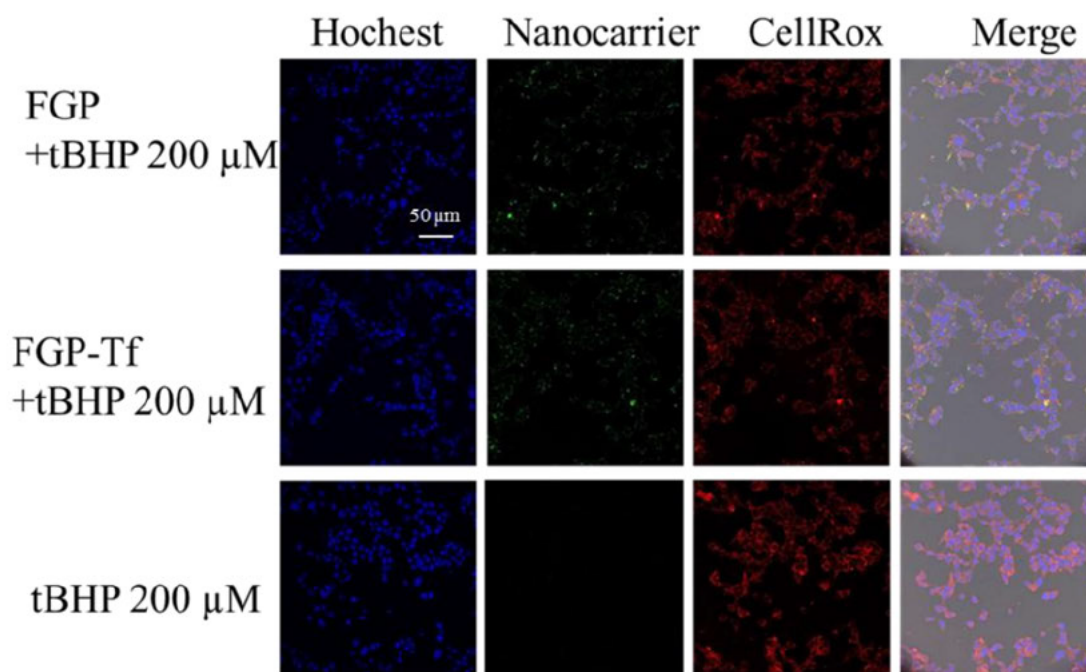a: Encapsulation Efficiency
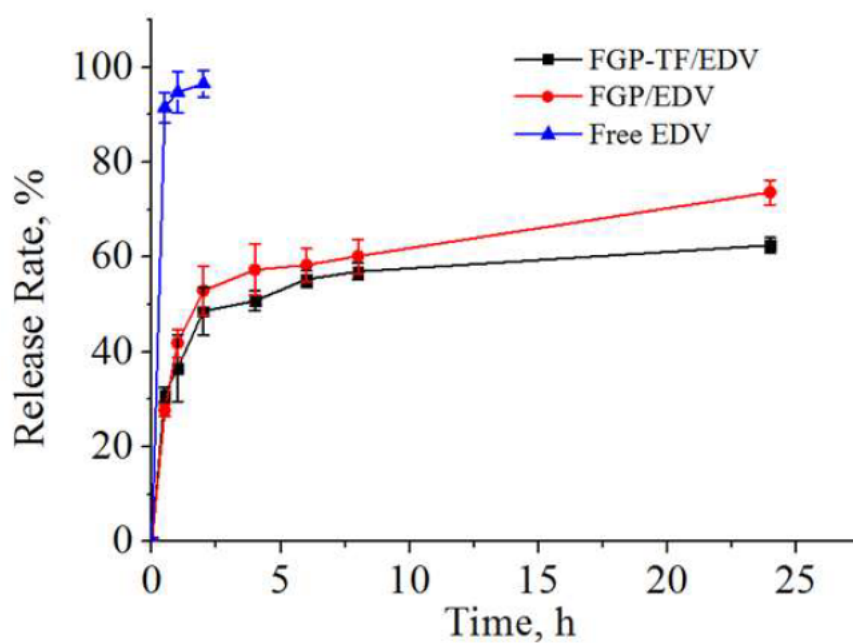
Figure S4 Drug loading and drug release profile of FGP/EDV and FGP-Tf/EDV.

FGP-Tf and FGP showed controlled drug release compared to free EDV.

Scale bar =50 μm, tBHP = 200 μM.

Figure S5 The intracellular ROS level of NSC34 cells after treating with FGP, FGP-Tf. 200 μM tBHP was used for creating excess ROS.

Reference:

[1] J.P. Taylor, R.H. Brown Jr, D.W. Cleveland, Decoding ALS: from genes to mechanism, Nature 539(7628) (2016) 197.

[2] Z. Mazibuko, Y.E. Choonara, P. Kumar, L.C. Du Toit, G. Modi, D. Naidoo, V.J.J.o.p.s. Pillay, A review of the potential role of nano-enabled drug delivery technologies in amyotrophic lateral sclerosis: lessons learned from other neurodegenerative disorders, J Pharm Sci. 104(4) (2015) 1213-1229.

[3] C. Saraiva, C. Praça, R. Ferreira, T. Santos, L. Ferreira, L.J.J.o.C.R. Bernardino, Nanoparticle-mediated brain drug delivery: overcoming blood–brain barrier to treat neurodegenerative diseases, J. Controlled Release 235 (2016) 34-47.

[4] J. Rosenfeld, M.J.J.N. Strong, Challenges in the understanding and treatment of amyotrophic lateral sclerosis/motor neuron disease, Neurotherapeutics12(2) (2015) 317-325.

[5] Q. Jin, Y. Cai, S. Li, H. Liu, X. Zhou, C. Lu, X. Gao, J. Qian, J. Zhang, S. Ju, Edaravone-encapsulated agonistic micelles rescue ischemic brain tissue by tuning blood-brain barrier permeability, Theranostics 7(4) (2017) 884.

[6] Y. Li, H. He, X. Jia, W.-L. Lu, J. Lou, Y. Wei, A dual-targeting nanocarrier based on poly (amidoamine) dendrimers conjugated with transferrin and

tamoxifen for treating brain gliomas, Biomaterials 33(15) (2012) 3899-3908.

[7] D. Silva Adaya, L. Aguirre-Cruz, J. Guevara, E. Ortiz-Islas, Nanobiomaterials' applications in neurodegenerative diseases, J. Biomater. Appl. 31(7) (2017) 953-984.

[8] C. Saraiva, C. Praça, R. Ferreira, T. Santos, L. Ferreira, L. Bernardino, Nanoparticle-mediated brain drug delivery: overcoming blood–brain barrier to treat neurodegenerative diseases, J. Controlled Release 235 (2016) 34-47.

[9] D.E. Igartúa, C.S. Martinez, C.F. Temprana, S.d.V. Alonso, M.J. Prieto, PAMAM dendrimers as a carbamazepine delivery system for neurodegenerative diseases: A biophysical and nanotoxicological characterization, Int. J. Pharm. 544(1) (2018) 191-202.

[10] L. Xu, H. Zhang, Y. Wu, Dendrimer advances for the central nervous system delivery of therapeutics, ACS Chem. Neurosci. 5(1) (2013) 2-13.

[11] Y.-J. Tsai, C.-C. Hu, C.-C. Chu, T. Imae, Intrinsically fluorescent PAMAM dendrimer as gene carrier and nanoprobe for nucleic acids delivery: bioimaging and transfection study, Biomacromolecules 12(12) (2011) 4283-4290.

[12] S.L. Mekuria, T.A. Debele, H.-C. Tsai, PAMAM dendrimer based targeted nano-carrier for bio-imaging and therapeutic agents, Rsc Advances 6(68) (2016) 63761-63772.

[13] G. Wang, L. Fu, A. Walker, X. Chen, D.B. Lovejoy, M. Hao, A. Lee, R. Chung, H. Rizos, M. Irvine, Label-free fluorescent poly (amidoamine) dendrimer for traceable and controlled drug delivery, Biomacromolecules (2019).

[14] H. Sawada, Clinical efficacy of edaravone for the treatment of amyotrophic lateral sclerosis, Expert Opin Pharmacother 18(7) (2017) 735-738.

[15] T. Moos, E.H. Morgan, Transferrin and transferrin receptor function in brain barrier systems, Cell. Mol. Neurobiol. 20(1) (2000) 77-95.

[16] R.-Q. Huang, Y.-H. Qu, W.-L. Ke, J.-H. Zhu, Y.-Y. Pei, C. Jiang, Efficient gene delivery targeted to the brain using a transferrin-conjugated polyethyleneglycol-modified polyamidoamine dendrimer, FASEB J. 21(4) (2007) 1117-1125.

[17] C. Gonzalez-Obeso, A. Girotti, J.C. Rodriguez-Cabello, A transferrin receptor-binding mucoadhesive elastin-like recombinamer: In vitro and in vivo characterization, Acta Biomater. 88 (2019) 241-250.

[18] W.I. Lee, Y. Bae, A.J. Bard, Strong blue photoluminescence and ECL from OH-terminated PAMAM dendrimers in the absence of gold nanoparticles, J. Am. Chem. Soc. 126(27) (2004) 8358-8359.

[19] D. Wang, T. Imae, M. Miki, Reprint of "Fluorescence emission from PAMAM and PPI dendrimers [J. Colloid Interface Sci. 306 (2007) 222–227], J. Colloid Interface Sci. 312(1) (2007) 8-13.

[20] G. Navarro, C.T. de ILarduya, Activated and non-activated PAMAM dendrimers for gene delivery in vitro and in vivo, Nanomed. Nanotechnol. Biol. Med. 5(3) (2009) 287-297.

[21] H. Suzuki, M. Matsuoka, Amyotrophic lateral sclerosis‐linked mutant VAPB enhances TDP‐43‐induced motor neuronal toxicity, J. Neurochem.

119(5) (2011) 1099-1107.

[22] Q. Bao, P. Hu, Y. Xu, T. Cheng, C. Wei, L. Pan, J. Shi, Simultaneous Blood–Brain Barrier Crossing and Protection for Stroke Treatment Based on Edaravone-Loaded Ceria Nanoparticles, ACS Nano 12(7) (2018) 6794-6805.

[23] X. Dong, Current strategies for brain drug delivery, Theranostics 8(6) (2018) 1481.

[24] Y. Xiao, C. Karam, J. Yi, L. Zhang, X. Li, D. Yoon, H. Wang, K. Dhakal, P. Ramlow, T. Yu, ROS-related mitochondrial dysfunction in skeletal muscle of an ALS mouse model during the disease progression, Pharmacol. Res. 138 (2018) 25-36.

[25] M.T. Carrì, C. Valle, F. Bozzo, M. Cozzolino, Oxidative stress and mitochondrial damage: importance in non-SOD1 ALS, Front. Neurosci. 9 (2015) 41.

[26] Y. Zhou, Z. Peng, E.S. Seven, R.M. Leblanc, Crossing the blood-brain barrier with nanoparticles, J. Controlled Release 270 (2018) 290-303.

[27] H.C. Helms, N.J. Abbott, M. Burek, R. Cecchelli, P.-O. Couraud, M.A. Deli, C. Förster, H.J. Galla, I.A. Romero, E.V. Shusta, In vitro models of the blood–brain barrier: an overview of commonly used brain endothelial cell culture models and guidelines for their use, J. Cereb. Blood Flow Metab 36(5) (2016) 862-890.

[28] I. Wilhelm, C. Fazakas, I.A. Krizbai, In vitro models of the blood-brain barrier, Acta Neurobiol Exp (Wars) 71(1) (2011) 113-28.

[29] B. Weksler, I.A. Romero, P.-O. Couraud, The hCMEC/D3 cell line as a model

of the human blood brain barrier, Fluids Barriers CNS 10(1) (2013) 16.

[30] H. Lu, W.D. Le, Y.-Y. Xie, X.-P. Wang, Current therapy of drugs in amyotrophic lateral sclerosis, Curr Neuropharmacol 14(4) (2016) 314-321.

[31] Z. Mazibuko, Y.E. Choonara, P. Kumar, L.C. Du Toit, G. Modi, D. Naidoo, V. Pillay, A review of the potential role of nano-enabled drug delivery technologies in amyotrophic lateral sclerosis: lessons learned from other neurodegenerative disorders, J. Pharm. Sci. 104(4) (2015) 1213-1229.

[32] M.M. Wen, N.S. El-Salamouni, W.M. El-Refaie, H.A. Hazzah, M.M. Ali, G. Tosi, R.M. Farid, M.J. Blanco-Prieto, N. Billa, A.S. Hanafy, Nanotechnology-based drug delivery systems for Alzheimer's disease management: Technical, industrial, and clinical challenges, J. Controlled Release 245 (2017) 95-107.

Chapter 5

A Robust Intrinsically Green Fluorescent Poly(amidoamine) Nanoprobe for *in vivo* Zebrafish Imaging

Intrinsically fluorescent PAMAM poly(amidoamine) dendrimers (IF-PAMAM) have attracted considerable attention in biological fields due to their excellent biocompatibility, inherent fluorescence, multifunctional surface, and high efficiency in drug or gene delivery. However, few studies have been reported in utilizing IF-PAMAM in *in vivo* models probably limited by their insufficient emission intensity, and the emission spectrum largely overlays to that of auto-fluorescence from biological organisms. In chapter 3, we have developed a novel intrinsically green fluorescent PAMAM dendrimers (FG5) with excellent fluorescent quantum yield, high wavelength excitation that enables FG5 a promising candidate for *in vivo* imaging by minimizing the influence of auto-fluorescence background from the biological matrix. Additionally, in chapter 4, we have shown enhanced BBB transportation and elevated neuron protection function of transferrin functionalized FG5 (FGP-Tf/EDV), which suggested that FGP-Tf based drug delivery system has great potential for further investigation in animal models. Before evaluating the therapeutic efficiency of FG5 based nanomedicines in *in vivo* models, it is practically required the FG5 possess sufficient fluorescence signal intensity and highly photo-stable for sensitive *in vivo* tracking and imaging. Therefore, in this chapter, we focused on using a

zebrafish model to assess the FG5 based nanoprobe' *in vivo* behaviours such as fluorescent performance, blood circulation, bio-distribution, biological barriers penetration features, and injection-methods, to give a data support for further application of FG5 based nanomedicines in animal models. Here, even though ALS mouse models (e.g. SOD1 mouse model) are more common for ALS study, due to the unique features of zebrafish, such as transparent body, similar genome (~70%) to humans, easy for genetic modification, relatively inexpensive housing, making them ideal model to build the bridge from *in vitro* cell models to *in vivo* mammalian models. Therefore, in this chapter we first selected zebrafish as animal model to test the *in vivo* bio-imaging properties of FG5.

Through the study in this chapter, we have further demonstrated that our fabricated fluorescent materials (FG5) possessed excellent capability for *in vivo* imaging and real-time tracking with strong green fluorescent signals, superior photo-stability, and very low fluorescent background (noise) from biological organisms. Additionally, we also provided a simple and effective zebrafish platform that can be potentially used for evaluating the *in vivo* behaviour of other fluorescent nanomaterials. Finally, the study in this chapter also provided a data support for optimizing FG5 based nanomedicines for further assessment in ALS disease animal models.

5.1 Contribution to this paper

	G.W	M.M	B.S	L.F	R.C	A.V	N.S
Experiment Design	•		•				
Sample Preparation	•					•	
Experiment Operation		•					
Data Collection	•	•				•	
Analysis	•	•		•		•	
Manuscript	•		•		•		•

This manuscript has been prepared for submission to *Small*. The majority of this work was completed by myself (>80%). Dr.Marco Morsch and Mr. Andres Vidal-itriago have provided me great support in zebrafish preparation, nanoparticle injection, fish imaging, and data analysis. Dr. Bingyang Shi and Dr. Nima Sayyadi have made great support in manuscript modification.

A Robust Intrinsically Green Fluorescent Poly(amidoamine) Nanoprobe for *in vivo* Zebrafish Imaging

Guoying Wang[a,b], Libing Fu[a,b], Bingyang Shi*[a,b], Marco Morsch[a], Nima Sayyadi[c], Roger Chung[a]

[a] Department of Biomedical Sciences, Faculty of Medicine & Health Sciences, Macquarie University, Sydney, NSW 2109, Australia

[b] Henan-Macquarie University joint center for Biomedical Innovation, Henan University, Kaifeng, 475001, China

[c] Department of Chemistry and Biomolecular Sciences, Macquarie University, Sydney, New South Wales 2109, Australia

Abstract

PAMAM dendrimers are emerging as versatile nanoplatforms for constructing multifunctional nanoprobes that can simultaneously deliver drugs to desired disease regions and monitor the delivery, release, and biodistribution of drugs in real-time. Recently, intrinsically fluorescent PAMAM dendrimers (IF-PAMAM) as novel nanoprobes are attracting more attention in the fields of biological imaging due to their excellent fluorescence properties, functional surfaces, high biocompatibility, and superior photo-stability. However, the majority of studies on IF-PAMAM focused on using *in vitro* rather than *in vivo* models. This could be due to the insufficient fluorescence emission intensities of intrinsic fluorescent PAMAM and the overlap of those materials with strong auto-fluorescence background from the biological organisms that result in low detection sensitivity. Therefore, we have developed a new type of intrinsic green fluorescence PAMAM (Generation 5, FG5) with enhanced emission efficiency and high

wavelength excitation that minimizes the influence of auto-fluorescence background in the biological system and enables FG5 to be tracked for *in vivo* study. In this study, we used zebrafish larvae as animal models to evaluate the bio-distribution, bloodstream circulation, and biological barriers penetration properties of our fabricated FG5 based nanoprobes. The comprehensive research provided a simple and efficient platform for evaluating the *in vivo* behaviours of variety FG5-based nanoprobes and provides a new idea for the development of PAMAM-based nanomedicines for neurodegenerative diseases.

5.2 Introduction

Amyotrophic lateral sclerosis (ALS), also known as motor neuron disease (MND) or Lou Gehrig's disease, is a rapidly progressive neurodegenerative disease that causes dysfunction of the nerves that control muscle movement that eventually leads to paralysis [1]. The main obstacle that limits the treatment of ALS is due to the fact that the causes of disease are mostly unknown [2]. Also, the presence of blood-brain barrier (BBB) and blood spinal cord barrier (BSCB) hinders small-molecule drugs (over 90%) and nearly all biologics to cross the barriers into the central nervous system (CNS) [3]. In the last few years, markedly progresses achieved from the development of nanotechnology that has opened the gate for nano-based diagnosis and therapeutic strategy of ALS [4, 5]. Particularly, due to the inherent valuable properties of nanoprobes such as high efficiency in drug loading, functional surface with desired ligands, unique optical properties, and potential capability to pass through biological barriers, nanomaterials are increasingly

recognized as promising candidates for early detection and drug delivery of ALS [3, 6]. Many nanomaterials, such as liposomes, polymer nanoparticles, PAMAM dendrimers, and gold nanoparticles, have been made to achieve efficient drug/gene delivery and bio-imaging in neurodegeneration disease, including ALS [6-8]. Among them, PAMAM dendrimers have been recognized as one of the most versatile nanoparticles that can be utilized for both diagnostics and therapy due to their relatively small size, highly branched, mono-disperse, and abundant surface functional agents [9-11]. Multifunctional methods of delivery and imaging technologies to evaluate whether PAMAM-based nanocarriers have reached the desired target will significantly benefit their applications in the field of ALS study [12, 13]. Therefore, PAMAM with detectable signals will greatly enhance its application prospects in drug delivery and bioimaging. Many efforts have been made to achieve visual detection of PAMAM dendrimers, most commonly through covalent attachment of fluorophores such as FITC, Cy5 onto a dendritic scaffold [14, 15]. However, fluorophore-conjugated PAMAM dendrimer may affect the size, mobility, surface structure, and solubility of the conjugates. Also, in some cases, the conjugated optical agents are toxic to normal cells and tissues, such as cadmium-based dyes, and some inorganic optical agents may decrease its biocompatibility [16]. Additionally, dissociating of the optical probe from dendrimer before it can reach to a specific target is another limitation that affects its optical stability. Furthermore, aggregation of hydrophobic fluorophores and subsequent self-quenching, as well as photo bleaching are major problems that

may influence the optical performance, especially by targeting *in vivo* [17-19]. To address these limitations, many intrinsically fluorescent PAMAM have been designed, such as 1-(4-carbomethyoxy) pyrrolidone-terminated dendrimers and chemically oxidized hydroxyl-terminated PAMAM dendrimers [18, 20]. However, the majority of these probes have just applied for the use of *in-vitro* rather than *in-vivo* models. To date, relatively few studies have been reported for a successful application of IF-PAMAM dendrimers in *in-vivo* models. The insufficient fluorescent intensity, the presence of high auto-fluorescence background from biological organisms that overlaps with most of intrinsically fluorescent PAMAM emission spectra limits their' *in vivo* applications [21]. Therefore, in this study, we report a novel intrinsically green fluorescent Generation 5 PAMAM (FG5) with excellent fluorescent quantum yield, superior photo-stability, and high wavelength excitation that could minimize the influence of the biological auto-fluorescence background and enables FG5 a promising candidate for *in vivo* imaging [19].

Zebrafish are emerging as an important and useful vertebrate model for studying neurodegenerative diseases include ALS, since they share a high degree of physiological and genome (~70%) to humans [22]. Their optically transparent features as embryos or larvae have made them more convenient for imaging using non-invasive imaging techniques. Additionally, the relatively easy for genetic modification, making them simple and effective models for disease and for label specific sites (cells, tissues). Furthermore, their small size and the relatively

simple laboratory culture conditions require relatively inexpensive housing, making them very cost-effective and reducing the amount of agent required for testing [22, 23]. Thus, as a simple and dynamic vertebrate model, zebrafish were widely used for assessing the features of nanomaterials, such as bio-imaging, toxicity, bio-distribution, and drug delivery [23-25]. In this study, we used the zebrafish larvae as simple vertebrate models to assess the circulation, biodistribution, and biological barriers penetration features of FG5 based nanoprobes (Scheme 1), thus building the bridge from *in vitro* cell models to *in vivo* mammalian models. To address the obstacles that hinders the application of PAMAM based nanomedicines in brain diseases, such as insufficient biological barrier penetration and short blood circulation, we further modified the FG5 nanoprobes with transferrin (Tf) since the transferrin receptor (TfR) is abundantly expressed in brain capillaries endothelial cells and have been widely used for receptor mediated transportation of nanomaterials to pass through BBB [26]. Additionally, to better bypass the biological barriers that hinder the ALS therapeutic drug delivery to CNS, we also investigated the diffusion, bio-distribution, and localization of FG5 nanoprobes in brain and spinal cord through intracranial or intraspinal cord injection (Scheme 1). Our data suggested that the PEGylated FG5 (FGP) and transferrin functionalized FG5 (FGP-Tf) hosted limited efficiency in crossing the BBB, but FGP-Tf could penetrate BSCB to a certain degree. Importantly, FGP-Tf presented significantly prolonged blood circulation time to FGP that may benefit its application for drug delivery.

Furthermore, intracranial or intraspinal cord injection of both FGP and FGP-Tf showed excellent diffusion of those nanoprobes in the brain and spinal cord that enables intracranial or intraspinal cord administration to be promising approaches for FG5 based nanomedicines to treat neurodegeneration diseases like ALS. This systematic study offered a simple and effective screening platform to evaluate the nanoprobes' *in vivo* biological properties, thus providing new thoughts in designing PAMAM based nanomedicines for ALS therapy.
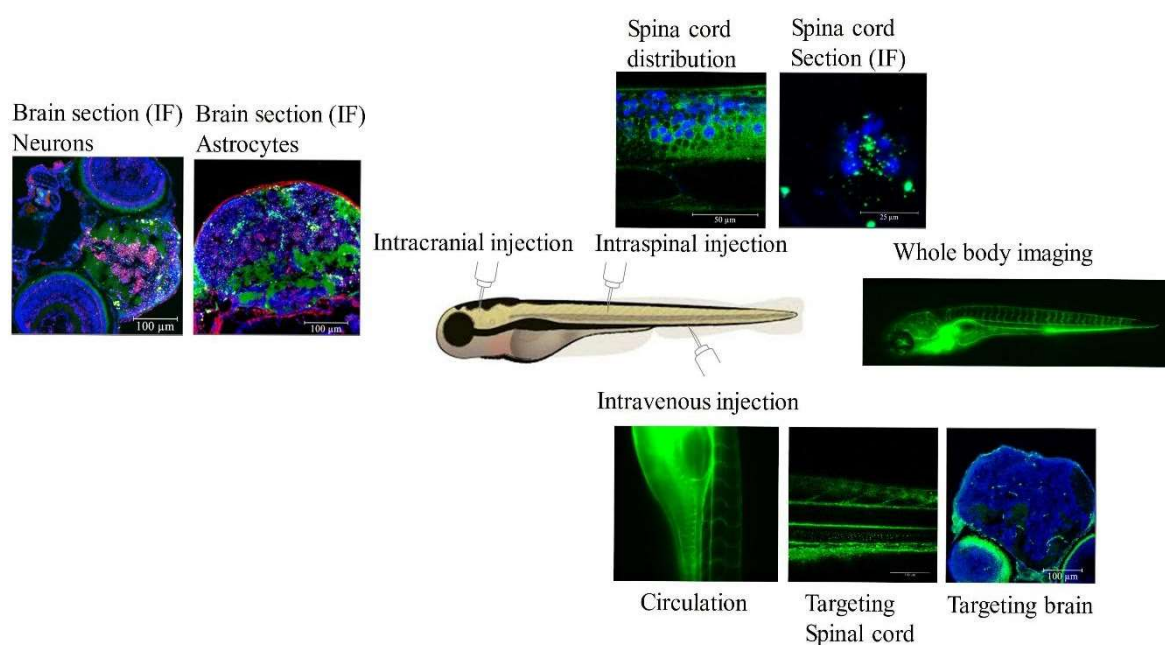
Scheme 1, Schematic illustration of different administration routes of FGP/FGP-Tf for zebrafish imaging.

5.3 Materials and Methods

5.3.1 Materials

PAMAM dendrimer, generation 5.0 solution (G5, ethylenediamine core), acetaldehyde, holo-Transferrin human, and *O*-[(N-Succinimidyl)succinyl-

aminoethyl]-*O'*-methylpolyethylene glycol (Ome-PEG-NHS, MW = 750) were purchased from Sigma-Aldrich (NSW, Australia). *O*-[N-(6-Maleimidohexanoyl) aminoethyl]-*O*-[3-(N-succinimidyloxy)-3-oxopropyl] polyethylene glycol (NHS-PEG-Mal; MW = 2000) was purchased from Jenkem Technology (Beijing, China). Other general chemicals were obtained from Sigma-Aldrich and used as received. Ultra Centrifugal Filters (Amicon®, 10, 30 and 100 KD) were purchased from Merck Millipore (VIC, Australia).

5.3.2 Preparation of FGP-Tf

Intrinsic fluorescent PAMAM was synthesized according to our previous report [19]. Typically, 50 mg (3.5 mmol) G5 in methanol was added into 5 mL of water. Then the pH of the solution was adjusted to 10 using NaOH (100 mM) solution. Then, 200 μL acetaldehyde was added dropwise to the above G5 solution. The reaction mixture was protected from the light and gently stirred at room temperature overnight. It was followed by dialysis using a dialysis bag (14K cut-off) for 24h to remove the unreacted excess acetaldehyde. The purified solution of G5 F-PAMAM (FG5) dendrimers was stored at 4 °C as a stock solution.

The as-prepared purified FG5 dendrimers were reacted with MAL-PEG$_{2K}$-NHS in PBS (adjusted to pH = 8.0 with 0.1M NaOH) at a ratio of FG5 to MAL-PEG-NHS 1:6 (mol : mol) at room temperature for 1 h. Ome-PEG-NHS (MW =1000) was then added to the solution at a ratio of FG5 to Ome-PEG$_{1K}$-NHS 1:10 (mol/mol) and kept reaction for another 1 h. After that, the prepared FG5-PEG-MAL/Ome was purified trough ultrafiltration (Amicon® Ultra Centrifugal Filters,

10KD) with PBS buffer (pH = 7.2) to remove unreacted PEG reagents and exchanged the buffer pH to 7.2. Thiolated Tf was then prepared according to a previous report [26]. Briefly, 10 mg Tf (0.13 mM) was dissolved in 1 mL PBS (pH = 8.0), then 0.7 mg 2-iminothiolane hydrochloride (5 mM) in 1 mL PBS (pH = 8.0) was added to Tf solution, the mixture was allowed to react for 1 h at room temperature. After that, the thiolated Tf was purified through a PD-10 Desalting column (GE Healthcare, Sephadex G-25) to remove unreacted impurities. The ratio of thiol groups to Tf was determined by testing the thiol groups with Ellmann's Reagent, and around 2.5 thiols groups were found on each Tf molecules. Then the thiol groups on Tf were specifically coupled to the peripheral maleimide of FG5-PEG in PBS (pH = 7.2) at a ratio of 2:1 (Tf to PAMAM, mol/mol) for 4 h at room temperature and kept 4 °C for overnight. The final compound was further buffer exchanged to water trough ultrafiltration (Amicon® Ultra Centrifugal Filters, 100 KD) when a cloudy solution was visualized the mixture was then transferred into centrifuge tube and centrifuged for 10 min at 10000 rpm. The precipitated product was re-dispersed in PBS and kept at 4 °C for further use.

5.3.3 Particle Characterization

Size and Zeta (ζ) potential of FG5, FGP, and FGP-Tf were measured using a Malvern Zetasizer APS instrument (Malvern, Australia). Transmission electron microscopy (TEM) image of FGP-Tf was captured by CM10 (Philips) system. Samples were negatively stained with Uranyl Acetate Replacement Stain (UAR-

EMS). Fluorescent spectra were acquired on Fluorolog spectroscopy (Horiba). Fluorescent intensity was recorded by Flexstation 3 (Molecular device, VIC).

5.3.4 Photo-stability and pH stability testing

For photo-stability testing, equal molar amounts of FGP-Tf and FITC were continuously scanned with 488nm laser via the Zeiss fluorescent microscopy (exposure time = 40 ms), fluorescent images were captured, and signal intensity was normalized to mean intensity at time = 0 min. For pH stability testing, FGP-Tf was dispersed in PBS with different pH conditions (7.2, 6.0, 5.0), the emission spectra were acquired by Fluorolog spectroscopy (Horiba).

5.3.5 Zebrafish housing

Zebrafish embryos were collected by natural spawning and maintained at 28°C in E3 medium, the 0.003% PTU (1-phenyl-2-thiourea) solution was added after 20 to 24 h and changed daily to control the formation of pigments. The injection was implemented in the zebrafish larvae at 5 days' post fertilization (dpf). The zebrafish experimental ethics were under the approval of Macquarie University Animal Ethics Committee (protocol no. 5201401007). To evaluate the behaviour of FGP and FGP-Tf nanoprobes in zebrafish spinal cord and to better understand the interaction between those nanoprobes and spinal cord motor neurons, injections were carried out in transgenic lines that express blue fluorescence within spinal cord motor neurons (motor neurons labelled with Tg(-3mnx1:TagBFP).

5.3.6 Zebrafish Microinjection and Imaging

FGP and FGP-Tf nanoprobes were injected into 5 dpf zebrafish (5 days post-fertilization) larvae using a microinjection protocol, respectively. Zebrafish larvae were anesthetized in 0.01% tricaine and embedded in a confocal dish (Cover-glass (22x22x0.2mm) Adhesion type, Fisher-Scientific) with 1% low-melting agarose (Fisher-Scientific), after agarose solidification, E3 medium containing tricaine was added in the dish. Borosilicate capillary glass needles were pulled and filled with 5 μL of FGP or FGP-Tf (0.15 mM). To ensure precise injection, the microinjection apparatus (WPI Inc.; Picospritzer II, General Valve Corporation) was installed next to a stereo dissection microscope (Leica, M205FA). The blood circulation of fluorescent nanoparticles can be visualized under fluorescent microscopy. Around 1~2 nL nanoparticles were injected into the interested area (brain, caudal vein and spinal cord). Live larvae were imaged post different time-points with confocal microscope (Leica SP5) and compound microscope (Leica DMI8).

5.3.7 Zebrafish Fixation and Cryosectioning

After anesthesia and euthanasia, Zebrafish were then fixed in 4% PFA in PBS on a gentle rocker overnight at 4 °C. After that, zebrafish were infiltrated with 30% sucrose in PBS at 4 degrees until they sink down to the bottom (typically overnight). The zebrafish brain and spinal cord were sectioned at 10 μm using a Leica CM1950 Cryostat after mounting with Tissue-Tek® O.C.T.™ and freezing at −80°C. Tissue sections were then transferred onto glass slides (Fisherbrand

Superfrost) and subsequently stored at $-80°C$ for further application on immunohistochemistry.

5.3.8 Zebrafish Immunohistochemistry

Before immunostaining, the frozen slides were recovered to room temperature for 10~20 minutes. After that, slides were rehydrated in PBS for another 10 min. To block the non-specific staining of the tissues with primary antibody, slides were incubated in blocking buffer (3% BSA in TBST (tris-buffered saline and 0.01% Polysorbate 20)) for 1 h at room temperature. The primary antibody was diluted in incubation buffer (3% BSA in TBST) according to the manufacturer's instructions. After blocking, the diluted primary antibody (Alexa Fluor® 647 conjugated primary recombinant Anti-NeuN antibody (ab190565, 1:200 dilution); primary anti-GFAP antibody (ab53554, 1:200 dilution) was dropped onto tissues and incubated overnight at 4°C. Then, slides were washed with PBS for 3 times (5 min each) and further incubated with secondary antibody (Alexa Fluor® 647 conjugated Secondary Goat Anti-Rabbit IgG (1:200 dilution)) for 2 h at room temperature in the dark and subsequently washed with PBS 3 times (5 min each) (For neuron labelling the incubation of secondary antibody was not needed). The antibody stained slides were further stained with Hoechst 33342 (Thermal, 1:2000 dilution) to visualize the nucleus and subsequently mounted (ProLong™ Diamond Antifade Mountant) and covered with coverslips. After that, sections were stored at 4°C for further confocal imaging.

5.3.9 Image processing

The 3D or overlayed zebrafish images were further processed with imaris software.

5.4 Results and Discussion

5.4.1 Physical and optical properties of FGP and FGP-Tf
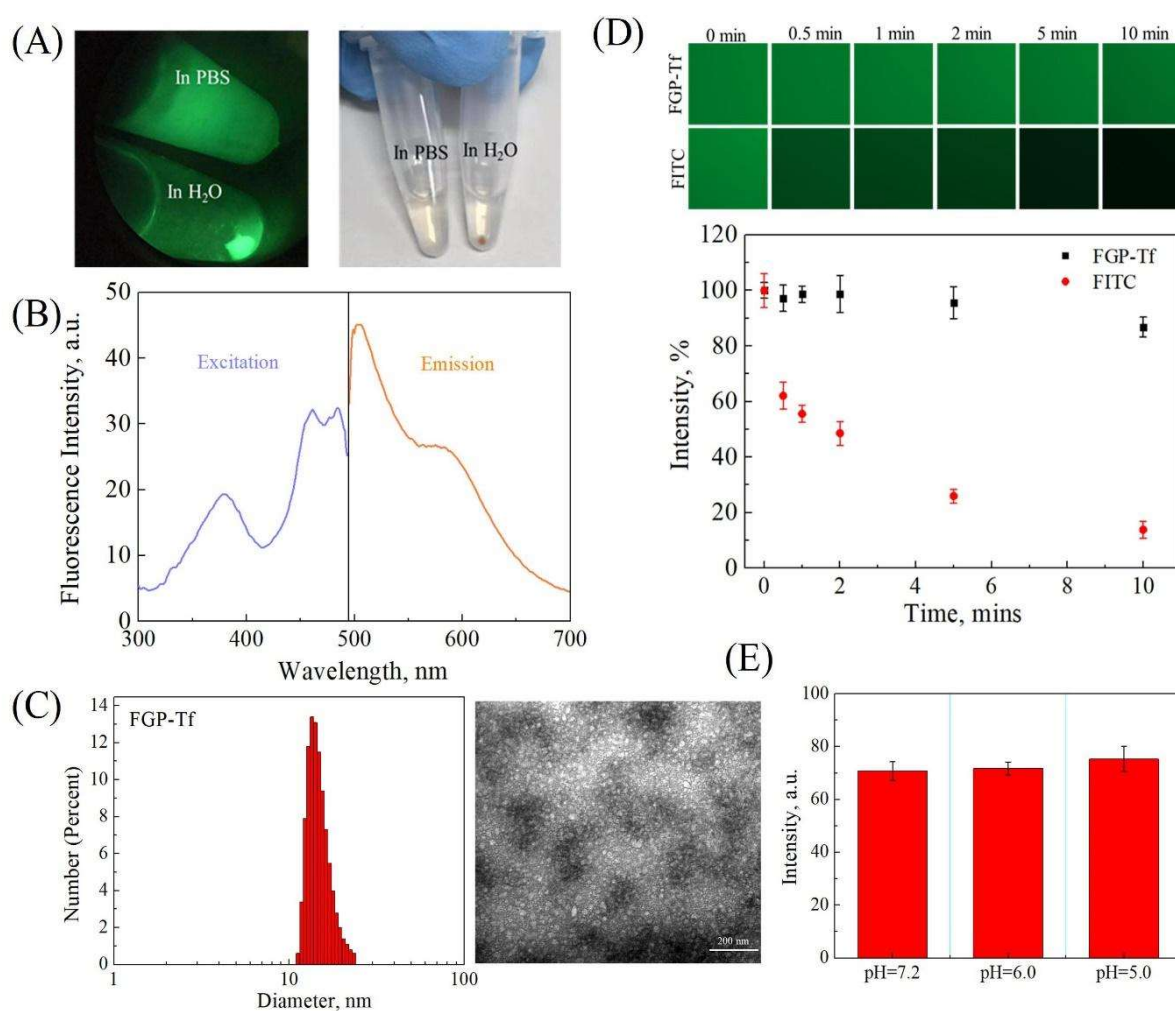
Fig 1, Physical and optical properties of transferrin functionalized intrinsic green fluorescent PAMAM (FGP-Tf). (A) The optical images of FGP-Tf in PBS and H₂O after centrifuge. Fluorescent images (left) (add excitation wavelength),

Bright images (right). (B) The fluorescent spectrum of FGP. (C) Size distribution (left) and TEM image (right) of FGP-Tf. (D) Photostability of FGP-Tf and FITC under the condition of continuous laser excitation (488 nm); Fluorescent images (upper) and Fluorescent intensity (lower). (E) Fluorescence intensity of FGP-Tf under different pH (7.2, 6.0, 5.0).

Table1, The size and zeta potential of FGP and FGP-Tf

Sample	Size, nm (Number)	Zeta, mV
FGP-Tf	15.6±1.2	-3.8±0.5
FGP	6.7±1.1	+2.1±0.7
FG5	4.6±1.5	+6.5±1.2

PEGylation was applied to intrinsic green fluorescent generation 5 PAMAM (FG5) to improve its stability in biological fluid [9]. Transferrin was subsequently conjugated on the surface of FGP to form multifunctional PAMAM (FGP-Tf) for potential BBB and BSCB penetration [27]. Briefly, 2-IT (Traut's reagent) was used to thiolate Tf, and about 90 % of thiolated Tf was collected after purification. The number of thiol groups in transferrin was determined by Ellmann's Reagent and defined at 2.5 per Tf. The FGP-Tf was purified by ultrafiltration through a molecular weight cut-off membrane of 100 KDa. Interestingly, when we changed the buffer of FGP-Tf from PBS to water, we found that the FGP-Tf formed aggregation in water and can be collected by centrifuge (10000 rpm, 10 mins). After that, the precipitated FGP-Tf could re-disperse in PBS or other ionic containing solution very well. Thus, we have effectively purified the product

(FGP-Tf) by simple buffer exchange approach as the starting materials, including pure FGP and transferrin, would not form precipitation in the water. The concentration of supernatant FGP and Tf were further tested to define the conjugation ratio between FGP and TF, after calculating the ratio of FGP to Tf in FGP-Tf was found around 1:1.5. The fluorescence spectra of FGP were shown in Fig. 1B and displayed a maximum excitation at 495 nm and maximum emission at 507 nm. Size and zetapotential of FGP and FGP-Tf were directly obtained by DLS. As seen in table 1, the original FG5 had a size of around 4.6 nm, which was close to the theoretical value of PAMAM G5 (5.0 nm). After PEGylating, the size increased to 6.7 nm, which is contributed by the addition of the PEG layer. Meanwhile the zetapotential was changed from +6.5 to + 2.1, which was probably caused by the partial replacement of positively charged amino group by the neutral PEG chain. After Tf conjugation, the size of FGP-Tf increased up to 15.6 nm, supporting the successful conjugation of Tf to FGP as the increased size was close to the size of free Tf (8 nm measured by DLS). In addition, the zetapotential of FGP-Tf changed from +6.5 to -3.8 mV, which could be the result of surface conjugation of negatively charged transferrin that neutralized the positively charged amino group. The size distribution (number) of FGP-Tf was shown in Fig. 1C (left) and presented very narrow PDI. TEM images in Fig. 1C (right) showed that the FGP-Tf had a relatively homogeneous particle size of approximately 15~25 nm, which made them suitable for use as multifunctional drug nanocarriers. We further tested the photo-stability of FGP-Tf under 488 nm

laser continuously excitation, commercial FITC was used as a comparison. As shown in Fig 1D, the fluorescence intensity of FGP-Tf decreased only 20% after 10 min of excitation, while the fluorescence intensity of FITC decreased by more than 70% after 5 min of excitation. The excellent photo-stability of FGP-Tf is a promising characterization of FGP-Tf nanoprobe for long-term continuous tracking. pH stability testing results are shown in Fig1 E indicated that the fluorescence of fabricated FGP-Tf was pH-independent, making this intrinsic fluorescent PAMAM desirable for different biological environments. To summarize, the enhanced emission intensity, high excitation wavelength, superior photo-stability, accompanied by smaller particle size made the fabricated FG5 a suitable nanoprobe for further *in vivo* imaging.

5.4.2 Nanoprobes localization in zebrafish
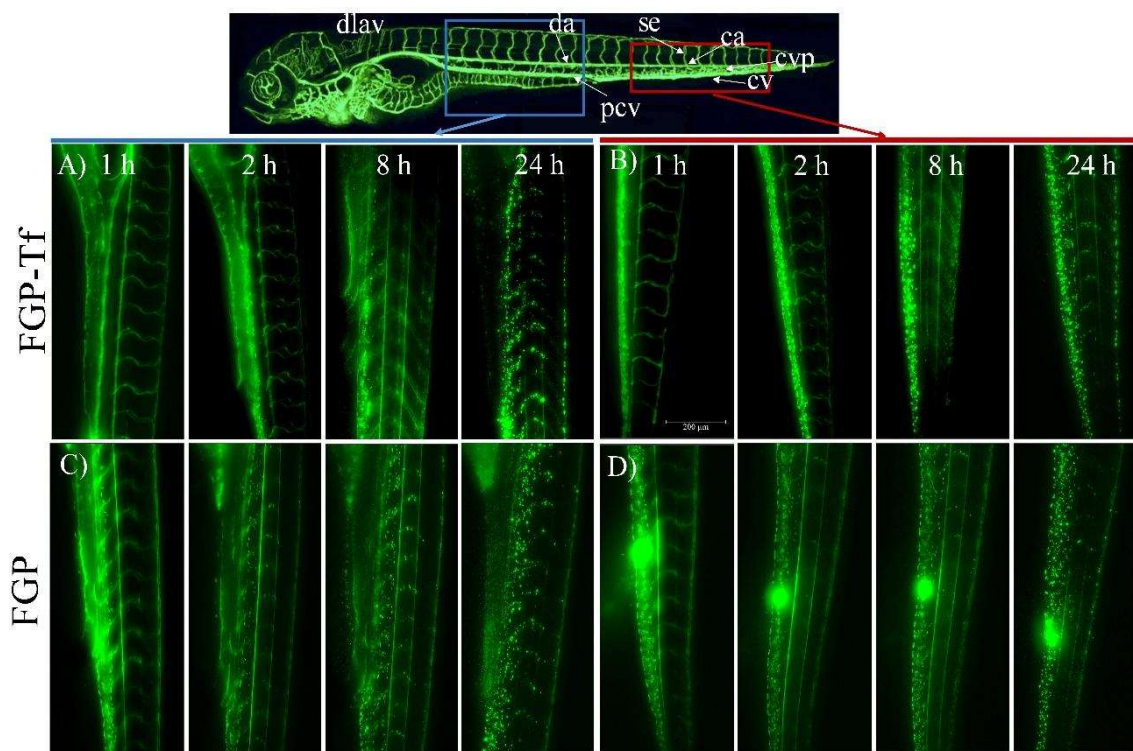
Figure 2. Nanoprobes localization in zebrafish. (A, B) Compound microscopy images of zebrafish after 1, 2, 8, 24 h of exposure to FGP-Tf. (C, D) Compound microscopy images of zebrafish after 1, 2, 8, 24 h of exposure to FGP. ca: caudal artery; cv: caudal vein; da: dorsal aorta; pcv: posterior (caudal) cardinal vein; se: intersegmental vessel; dlav: dorsal longitudinal anastomotic vessel; cvp: caudal venous plexus.

The blood circulation condition of nanomaterials plays an important role in determining their capability of "on-target" effect to desired sites[28, 29]. Therefore, evaluating the FG5' localization in bloodstream will provide the basis for optimization of the PAMAM based nanomedicines. In this study, FGP and FGP-Tf (5 nL) were injected separately in the caudal vein (cv) of 5 dpf zebrafish and imaged in live larvae by Compound Microscopy (Leica). Larvae exposed to FGP and FGP-Tf (Fig. 2) were imaged after 1, 2, 8, 24 h injection of nanoparticles, respectively. Nanoprobes signal was observed in the bloodstream within 1~2 minutes after injection (data are not shown). 1 h post-injection, green signals from FGP or FGP-Tf were detected in dorsal aorta (da), posterior cardinal vein (pcv) and intersegmental vessel (se) (Fig 2A), meanwhile, large amount of nanoparticle accumulation was observed in caudal venous plexus (cvp) for both FGP and FGP-Tf (Fig 2B), which was similar to previous report that nanoparticles were readily uptake by cvp during blood circulation [30]. The difference was that some green granules were found between da and pcv in FGP treated zebrafish (Fig 2C), which was more likely caused by the quick penetration of FGP from pcv to extravascular

tissue. 2 h post-injection, a large amount FGP-Tf was still circulating and more accumulation was found in pcv (Fig 2A, 2 h). Differently, the green signal from FGP in se and da was disappeared, which indicated the complete clearance of FGP from bloodstream. Meanwhile, more FGP granules accumulation were found between da and pcv. Interestingly, the accumulated green FGP granules more likely located along with the muscle junctions. More clear evidence was found in zebrafish post 8 h injection (Fig 2C, 8 h). The similar nanoparticles localization of FGP-Tf in muscle and muscle junctions was observed in zebrafish post 8 h injection (Fig 2A, 8 h), suggesting that the penetration rate of FGP-Tf from pcv and the diffusion rate of FGP-Tf in muscle were slower than FGP. 24 h post injection, FGP, and FGP-Tf displayed similar particle localization (Fig 2, 8 h). Briefly, a large amount of particle accumulation was located in the area between cv and ca as well as da and pcv, and some green granules were found along with the muscle junction. This indicates that those nanoparticles have been completely absorbed by different types of cells in zebrafish. Additionally, we recorded the blood circulation conditions of FGP and FGP-Tf in the middle section of zebrafish and FGP-Tf displayed clear blood circulation for up to 6h while FGP can only circulate around 1 h, non-PEGylated G-PAMAM (FG5) was also tested in this study and showed very short circulation time (several min) (Data are not shown). It is widely believed that PEGylation *in vivo* could reduce the binding of serum proteins and the process of opsonization that enables longer circulation of nanomaterials, thus the prolonged circulation time of FGP to FG5 was majorly

contributed by the PEG layer [31]. The much longer circulation time of FGP-Tf was more likely contributed by the larger size of FGP-Tf to FGP as well as the stealth effect of protein that attenuates the endocytosis of endothelial cells [32].

5.4.3 The Blood-brain penetration

Blood-brain barrier (BBB) is the major obstacle that hinders most of the therapeutic drugs to the brain [33]. The BBB penetration ability of FGP and FGP-Tf were evaluated via directly injecting those nanoparticles in cardinal vein of 5dpf zebrafish. The live larvae were imaged under fluorescent microscopy (leica) and confocal (Leica SP5). As shown in Fig 3A, very clear green signals from FGP-Tf were detected in brain blood vessels at 1, 2, 4 h post injection, however, it was hard to detect the diffusion of FGP-Tf from brain blood vessel to internal brain tissue evidenced by the similar green signal distribution from 1 to 4 h (Fig 3A, lower). The circulation signals from FGP in the brain blood vessel was only detectable within 1h (Fig 3B), suggesting that most of FGP have been quickly cleared from blood circulating within 1h. 24 h post injection, FGP and FGP-Tf mainly existed in the forms of green granules in the zebrafish brain (Fig 3 AB, 24h). In order to localise those green fluorescent granules in brain, the brain cryostat tissue sections were prepared and analyzed. As shown in Fig S1, the FGP or FGP-Tf green granules in brain section seems more likely still co-localized with the blood vessel, suggesting that FGP-Tf or FGP may still be trapped in the brain-blood vessel endothelial cells rather than crossed the blood brain barrier. Thus, it is important to design nanomaterials that can escape from endothelial cells

to exert their function in the brain [34, 35]. The limited BBB penetration ability of FGP-Tf in zebrafish was not consisted with our previous report, in which the FGP-Tf can effectively cross the *in vitro* BBB model. This difference may be due to the limitations of *in vitro* BBB model, typically, *in vivo* BBB model may reflect more realistic human BBB conditions. Moreover, we used 5 days old zebrafish as the *in vivo* BBB model, the difference in BBB structure and function between baby zebrafish and adult human, such as the expression level and the activity of transporters and receptors (including Tf receptor), the expression level of tight junction proteins, may also cause this kind of inconsistence [36]. Since the BBB structure and function may differ with different species and ages, it's important to evaluate the blood-brain barrier penetration capability of fabricated nanocarriers by using animal models that closer to human brain structures. Therefore, more investigations are needed to estimate the rationality of zebrafish as *in vivo* BBB model [37]. The blood circulation time of nanoparticles also directly affects the interaction of NPs with brain blood vessel endothelial, which implies that the longer circulation time, the more chance for NPs to pass through the BBB. Thus, even though FGP-Tf cannot effectively cross BBB, its prolonged blood circulation time provides more chances in further optimized to enhance its capability of BBB penetrating.
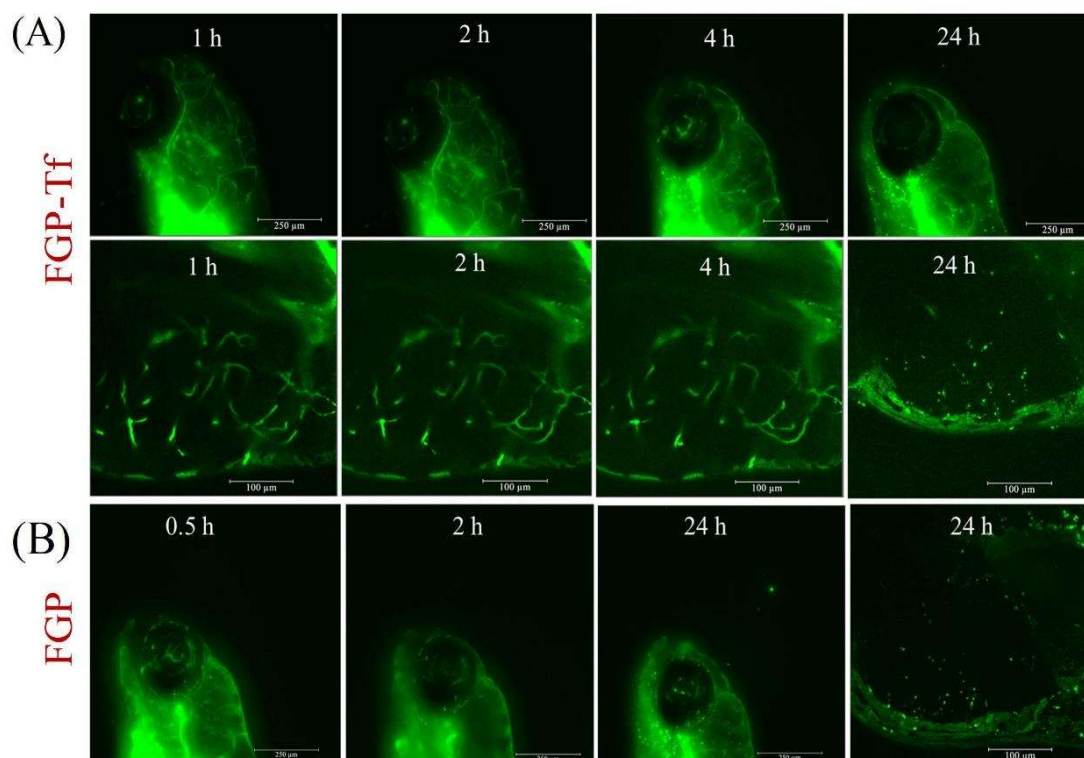
Fig 3, The blood-brain barrier penetration of nanoparticles. (A) Fluorescent microscopy images of FGP-Tf in zebrafish brain (upper) and confocal images of FGP-Tf in fixed area of zebrafish brain (lower, 1-4 h). The lower 24 h was the overlayed z-stack images of FGP-Tf in the zebrafish brain. (B) Fluorescent microscopy images (0.5, 2, 4 h) and overlayed z-stack confocal images of FGP in the zebrafish brain.

5.4.4 The bio-distribution of FGP-Tf and FGP in different organs and tissues
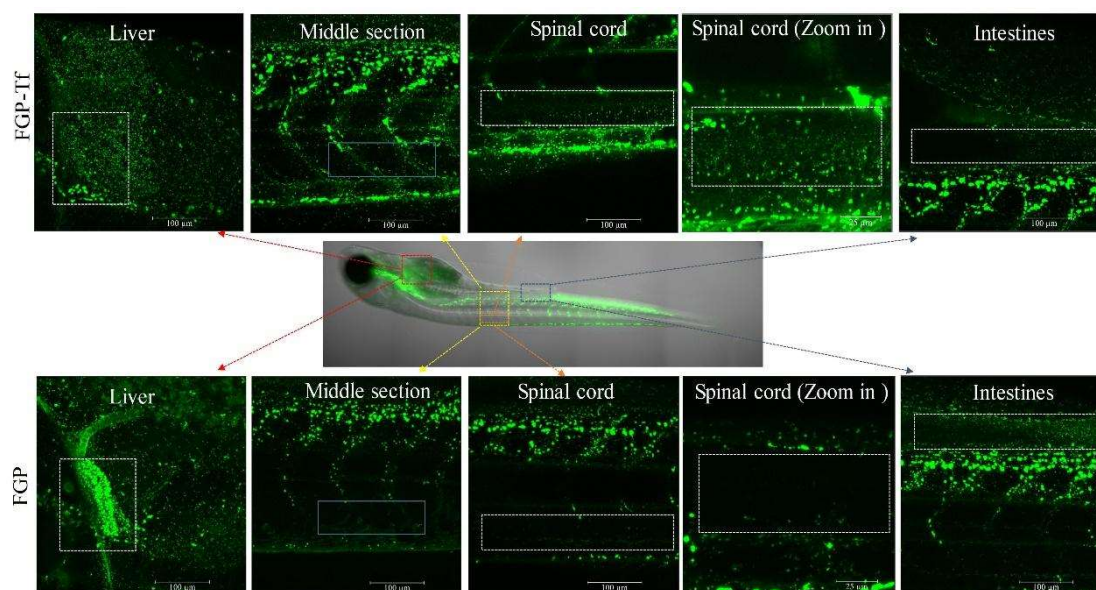
Figure 4. The bio-distribution of FGP-Tf and FGP in different organs or tissues of zebrafish 24 h post injection. Images were captured through confocal microscopy.

Next, we tested the distribution of FGP and FGP-Tf in the liver, intestines and spinal cord of zebrafish. As shown in Fig 4, 24 h post caudal vein injection, the accumulation of FGP-Tf in zebrafish liver was very weak. But there was still a relatively high level of liver accumulation of FGP in zebrafish, which indicated that the liver clearance rate of FGP-Tf was faster than FGP that may benefit from reducing the side effects of FGP-Tf toward liver. Similar to the liver, the intestines clearance of FGP-Tf also faster than that of FGP, accompany with the liver clearance result, suggesting that FGP-Tf was much easier to be cleared by digestive and detoxification systems that enable FGP-Tf a safer nanoprobe for bio-imaging and potential drug delivery. Interestingly, for both FGP and FGP-Tf

treated zebrafish, we found clear nanoparticles granules located within the muscle and along with muscle junction. That was probably because the FGP or FGP-Tf were quickly absorbed by venule vessel, subsequently penetrated the blood vessel and spread in muscle junctions, further investigate was warrant to study the behaviours of FG5 in muscle. We further focused on the spinal cord and found that both FGP and FGP-Tf could penetrate the blood spinal cord barrier (BSCB) in a certain degree, especially for FGP-Tf (Fig 4, spinal cord and spinal cord zoom in images). Meanwhile, we counted the percentage of green nanoparticles positive motor neurons and showed that around 30% of motor neurons were co-localized with FGP-Tf (Fig 5). In contrast, only 4% motor neurons were co-localized with FGP. The distribution of those nanoprobes in the spinal cord revealed that FGP-Tf could be potentially applied for delivering drugs to the spinal cord and targeting motor neurons.
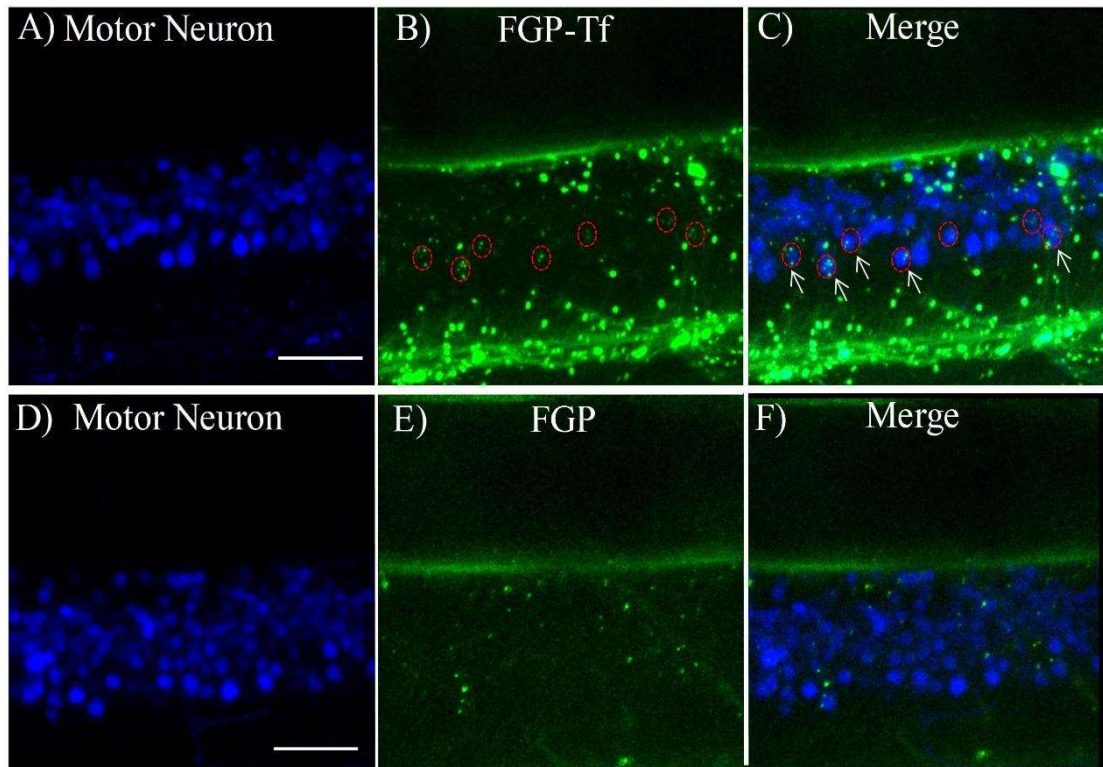
Figure 5. The bio-distribution of FGP and FGP-Tf in the zebrafish spinal cord. (A, D) Express blue fluorescent protein (mTagBFP) in motor neurons. (B, E) Green fluorescence from FGP or FGP-Tf. (C, F) The merged images and the percentage of FGP/FGP-Tf positive motor neurons.

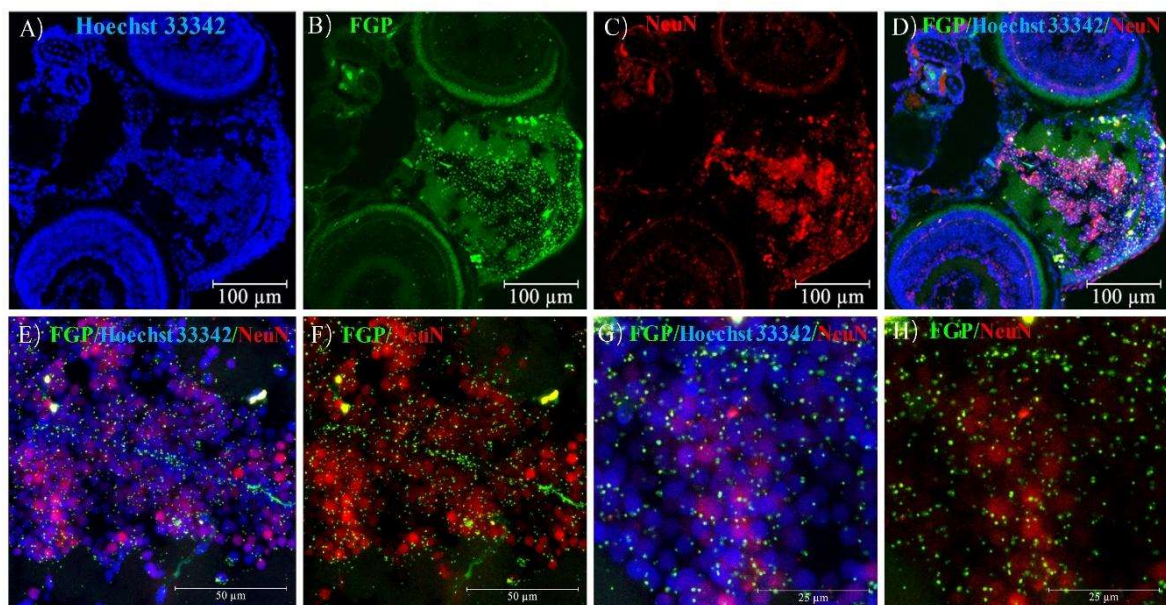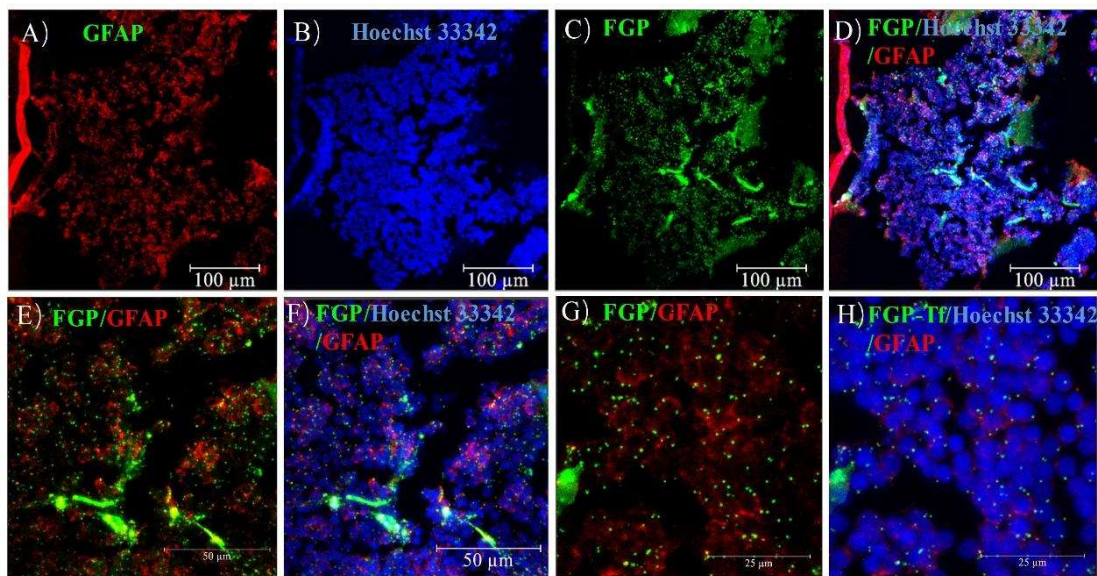## 5.4.5 Brain distribution of FGP and FGP-Tf after intracranial injection
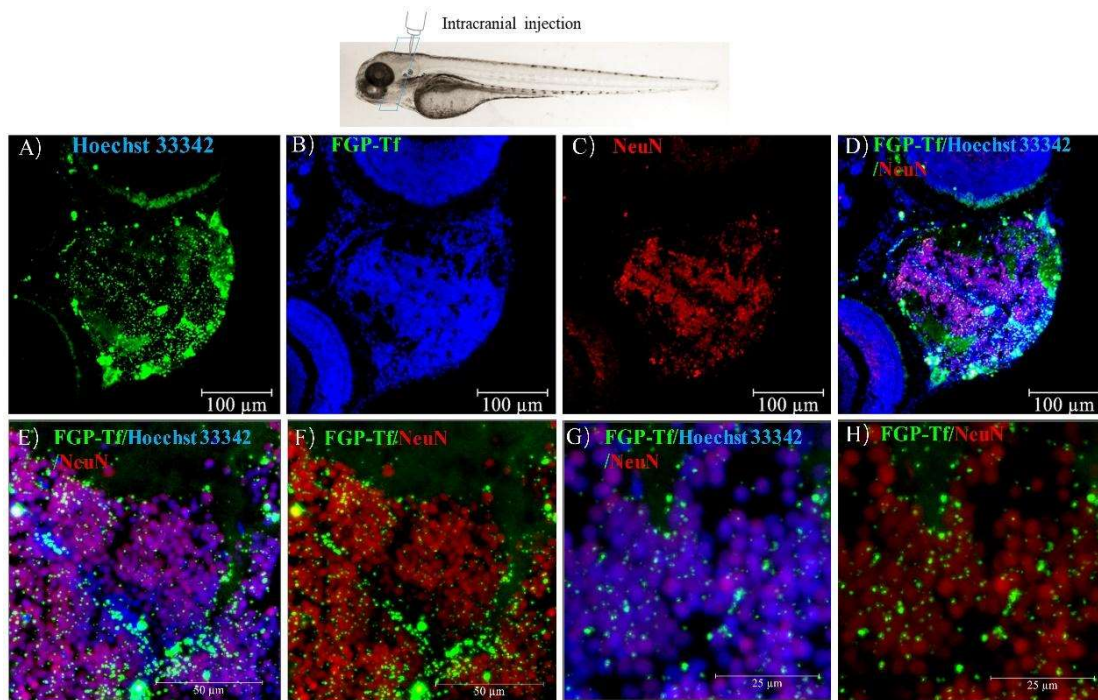
Figure 6. Confocal images of the FGP-Tf distribution in zebrafish brain slice after intracranial injection, tissues were stained by Neuron marker (NeuN). A-D are confocal images under 40 times objective magnification, E, F are images under 120 times objective magnification. G, H are images under 360 times objective magnification.
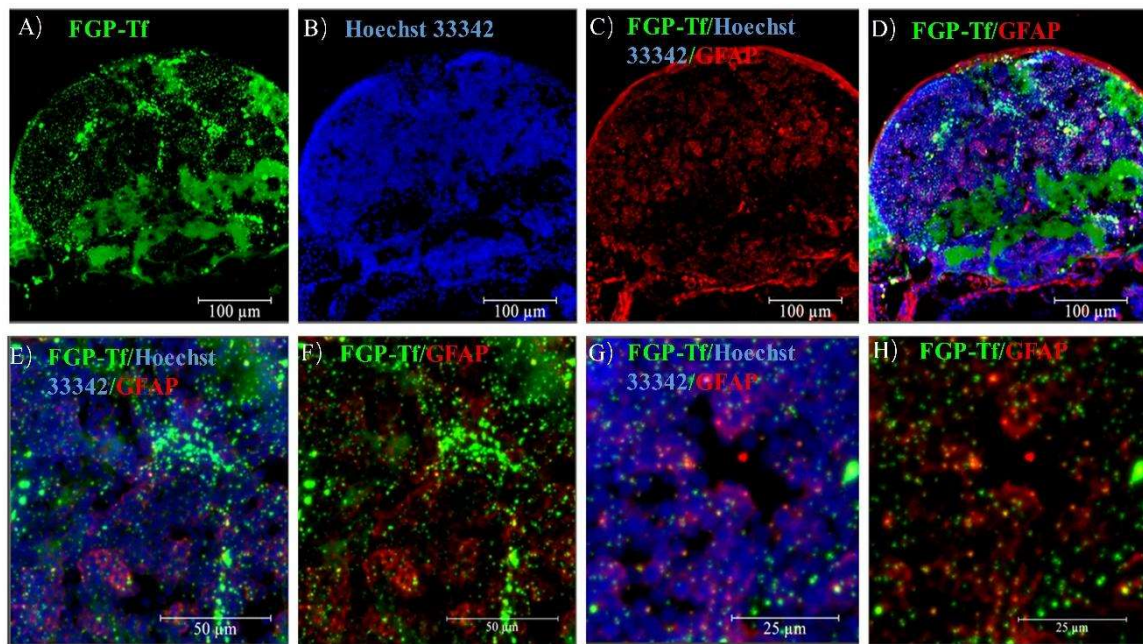
Fig 7 Confocal images of the FGP-Tf distribution in zebrafish brain slice after intracranial injection, tissues were stained by astrocytes marker (GFAP). A-D are confocal images under 40 times objective magnification, E, F are images under120 times objective magnification. G, H are images under 360 times objective magnification.

Fig 8 Confocal images of the FGP distribution in zebrafish brain slice after intracranial injection, tissues were stained by Neuron marker (NeuN). A-D are confocal images under 40 times objective magnification, E, F are images under 120 times objective magnification. G, H are images under 360 times objective magnification.

Fig 9 Confocal images of the FGP distribution in zebrafish brain slice after intracranial injection, tissues were stained by astrocytes marker (GFAP). A-D are confocal images under 40 times objective magnification, E, F are images under120 times objective magnification. G, H are images under 360 times objective magnification.
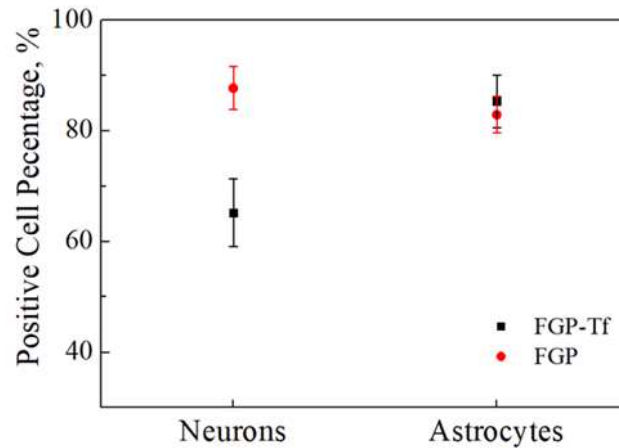
Figure 10. The positive cell percentage of FGP and FGP-Tf in neurons and astrocytes. Results were recorded by counting at least 200 cells.

As previously reported, up to 95% nanoparticles were cleared by the liver and macrophagocyte system. Only very limited nanoparticles could accumulate in the target site like brain [38]. Our zebrafish brain imaging results after caudal vein injection of FGP and FGP-Tf also proved this description. Thus, the intracranial injection may be an alternative approach that could bypass the blood-brain barrier and phagocytic system, which enables more particles to target the brain region [39, 40]. However, currently, little is known regarding the diffusion, biodistribution, and cellular phagocytosis of those intrinsic fluorescent PAMAM. In this study, FGP and FGP-Tf were administrated in the zebrafish brain via directly intracranial injection. The live zebrafish were imaged post 2, 6, 24 h injection via confocal. As seen in Fig S2 A, D, after intracranial injection, the nanoparticles were mainly accumulated in the middle cerebral cortex and gradually spread throughout the brain. 6 h post intracranial injection, the accumulation area of nanoparticles in the middle cerebral cortex was becoming smaller. Meanwhile, the transport route of

nanoparticles became much clear (Fig S2 B, E), indicating more nanoparticles were diffusing into the brain tissues. Considering the cerebral interstitial fluid is not fast-moving, the entire diffusion of nanoparticles in brain was relatively slow progress. Therefore, if an intracranial injection is considered for therapeutic drug delivery, it is necessary to avoid the rapid release of drugs from nanocarrier. 24 h post intracranial injection, the FGP-Tf were evenly distributed in the brain tissue (Fig S2 C, F) and existence as green granules, suggesting that those nanoparticles have an excellent diffusion capability and can be effectively absorbed by brain cells. To more specifically localize the PAMAM based nanoprobes to the brain tissue, 24 h post intracranial injection, the zebrafish brain was cryostat sectioned and stained with neuron and astrocytes markers. As seen in Fig 6-9, FGP or FGP-Tf evenly distributed in the whole brain tissue slice. Some green granules were located along with the central cross, which was more likely caused by the initial accumulation of NPs in the middle cerebral cortex that induced more cell absorption in those areas. The specific localization of FGP and FGP-Tf showed slight difference as the accumulated green granules from FGP were smaller and more dispersed (Fig 6-9). Additionally, the co-localization of FGP with neurons showed a higher percentage than FGP-Tf (Fig 6, 8). We further studied the targeting capability of those nanoparticles to brain cells, and the statistical result was shown in Fig 10. Particularly, both neurons and astrocytes showed the equal positive percentage of FGP and kept at a higher level (>80%), suggesting that FGP could be effectively absorbed by those cells. However, this kind of

absorption was non-specific. For FGP-Tf, the astrocytes showed relatively higher positive percentage of FGP-Tf (>80%). In contrast, the neurons showed slightly lower positive percentage of FGP-Tf (~65%), which indicated that FGP-Tf might possess a less affinity to neurons compared to astrocytes. Our brain distribution data suggested that the intracranial injection could effectively deliver those nanoparticles in the whole brain area. However, due to the evenly spread throughout the brain, nanoparticles were not selectively delivered to the specific brain cells. Therefore, conjugating brain cells targeting agents and optimizing intracranial injection approaches are warranted for further investigation [41].

5.4.6 Biodistribution in the spinal cord after intraspinal injection

As previous work has described that only limited systemically injected nanoparticles can reach their target tissue by passive transport, which limits the efficacy of these particles to achieve therapeutic results [39, 42]. Even though the FGP-Tf nanoparticles have shown the ability to cross BSCB, the penetration efficiency was still insufficient for higher dosage requirements. Thereby, we evaluated the intraspinal cord behaviour of FG5 based nanoprobes by a genetically modified zebrafish model through directly spinal cord injection. After genetic modification, the spinal cord motor neurons can express blue fluorescence, which makes it possible to evaluate the influence of nanomaterial to motor neurons in terms of cytophagy and cytotoxicity via fluorescent microscopy technology. After intraspinal injection, the nanoparticles quickly diffused from the injection point to the whole spinal cord (within 30 mins), which was much

faster than the diffusion of nanoparticles in the brain. Meanwhile, the green nanoparticles were clearly observed surrounding the motor neurons post 1 h injection (Fig S3 S4 A-B, E). 24 h post injection, most of the nanoparticles were absorbed by spinal cord cells, and more than 60% percent motor neurons showed co-localization with green nanoparticles (Fig S3 S4 C-D, F), which suggested that those nanoparticles could be effectively uptake by motor neurons. The intraspinal cord distribution of FGP and FGP-Tf after 6 h injection in Fig S5 showed that the cellular uptake of FGP was faster than FGP-Tf, which was probably caused by the relatively smaller size of FGP to FGP-Tf. We also evaluated the diffusion distance of FGP-Tf and FGP in the spinal cord, as seen in Fig S6, FGP-Tf group presented much farther diffusion distance than that of FGP, which may be because the slower cellular absorbs of FGP-Tf that allowed more particles to diffuse to the near brain site. The spinal cord cryostat section was acquired post 24 h intraspinal injection of fluorescent nanoparticles, as seen in Fig S7, both FGP and FGP-Tf were evenly distributed throughout the spinal cord and can be efficiently taken up by motor neurons. However, this cellular uptake is not specific, and the rapid and uniform spread of nanomaterials throughout the spinal cord may give all spinal cord cells an equal chance to uptake those nanoprobes.

Additionally, we also observed that those fluorescent nanoparticles could stay in spinal cord cells for at least 72 h (data not shown), which makes them possible to deliver drugs to the spinal cord and maintain the required drug concentration for a long period. Importantly, intraspinal injection of nanoparticles may also

benefit the delivery of biological macromolecules (siRNA, ASOs, therapeutic proteins) since they are unable to cross BSCB and easily degraded and removed by organisms. However, non-specific absorption by all types of spinal cord cells was still a major issue for administrating nanomedicines via intraspinal injection approaches. The development of functional nanocarriers to target specific cells are warranted for further investigation.

5.5 Conclusion

In the past few years, fluorescent PAMAM dendrimers have attacked intensive interesting in drug delivery and bio-imaging. The emerging intrinsic fluorescent PAMAM has shown great advantages to traditional fluorophore labelled PAMAM dendrimers in terms of inherent fluorescence, biocompatibility, and photostability. In this study, we fabricated a novel intrinsic green fluorescent PAMAM (FG5) and evaluated it's *in vivo* behaviour through a vertebrate zebrafish model. The excellent *in vivo* real-time tracking and bioimaging features from FG5 has filled the gap that utilizing intrinsically fluorescent PAMAM for *in vivo* applications. The circulation, bio-distribution, biological barriers penetration capability from zebrafish imaging suggested that transferrin functionalized FG5 (FGP-Tf) with prolonged blood circulation, low retention in liver and high efficiency in penetrating BSCB possessed more advantages than PEGylated FG5 (FGP) for potential drug delivery. To improve the accumulation of FG5 in the brain and spinal cord that related to ALS to satisfy the higher dosage requirement, intraspinal cord and intracranial injection were further investigated in our study.

The brain and spinal cord distribution of FGP and FGP-Tf indicated that those nanoparticles can evenly diffuse in the entire brain and spinal cord tissues and can be effectively uptake by neurons and astrocytes, however, the phagocytosis of cells in brain and spinal cord is not selective, further functionalization of FG5 with targeting peptides, antibodies and proteins is warrant for realizing better targeted therapy.

Acknowledge

5.6 Supporting information
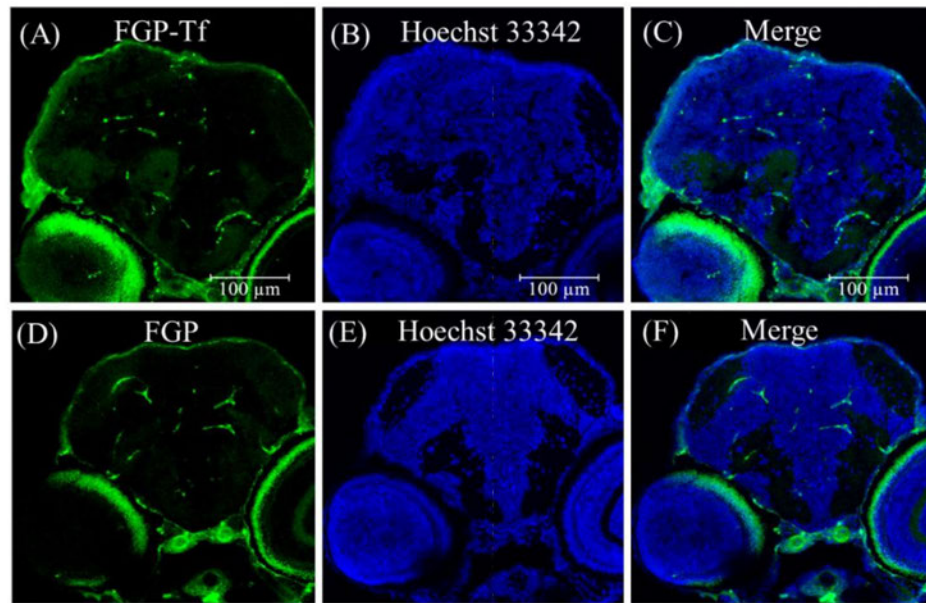
Figure S1 The bio-distribution of FGP (A-C) and FGP-Tf (D-F) in the brain slice. Nucleus were stained with Hoechst 33342.
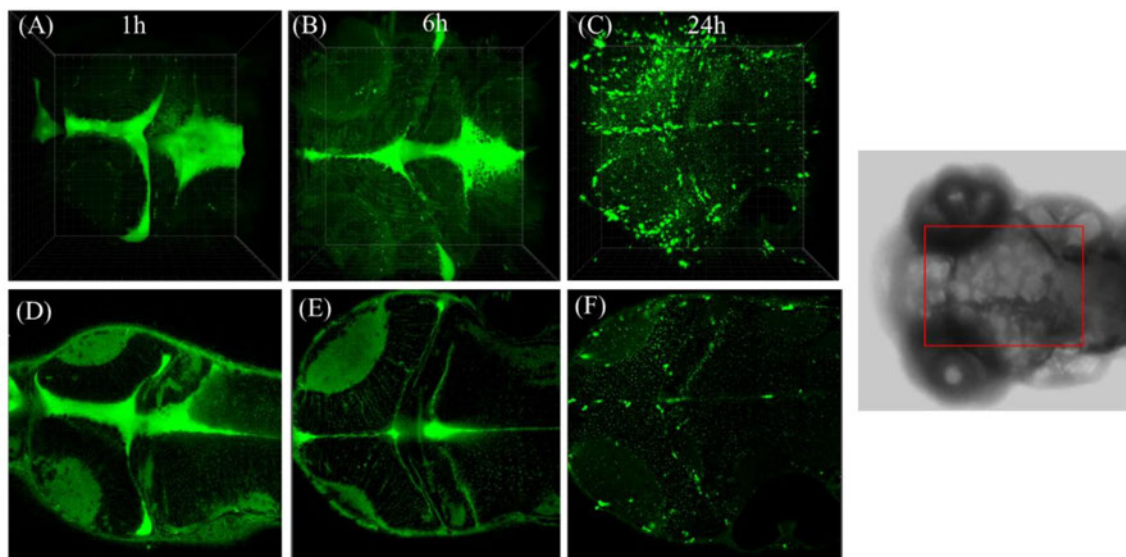
Figure S2 The diffusion of FGP-Tf after intracranial injection. (A-C) were 3D images processed by Imaris software. (D-F) were single-layer images of the zebrafish brain. Green signals were from FGP-Tf.
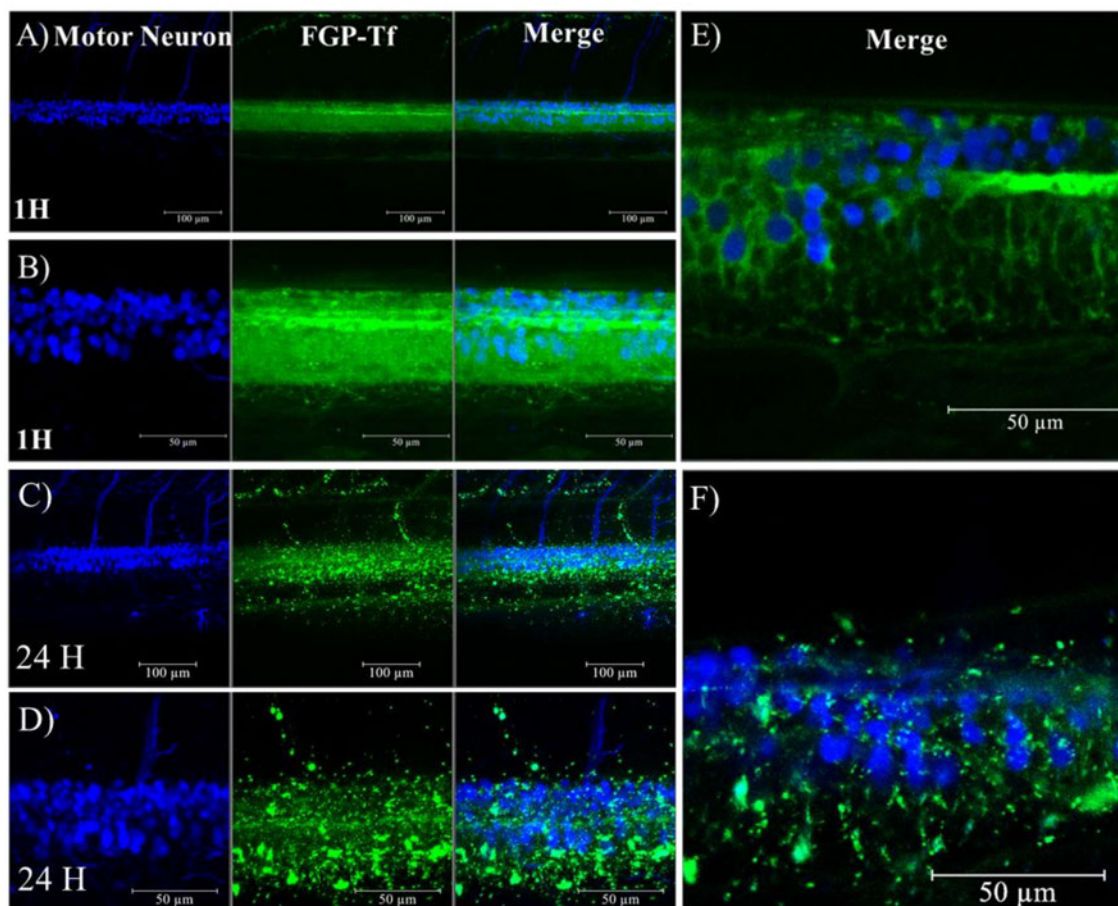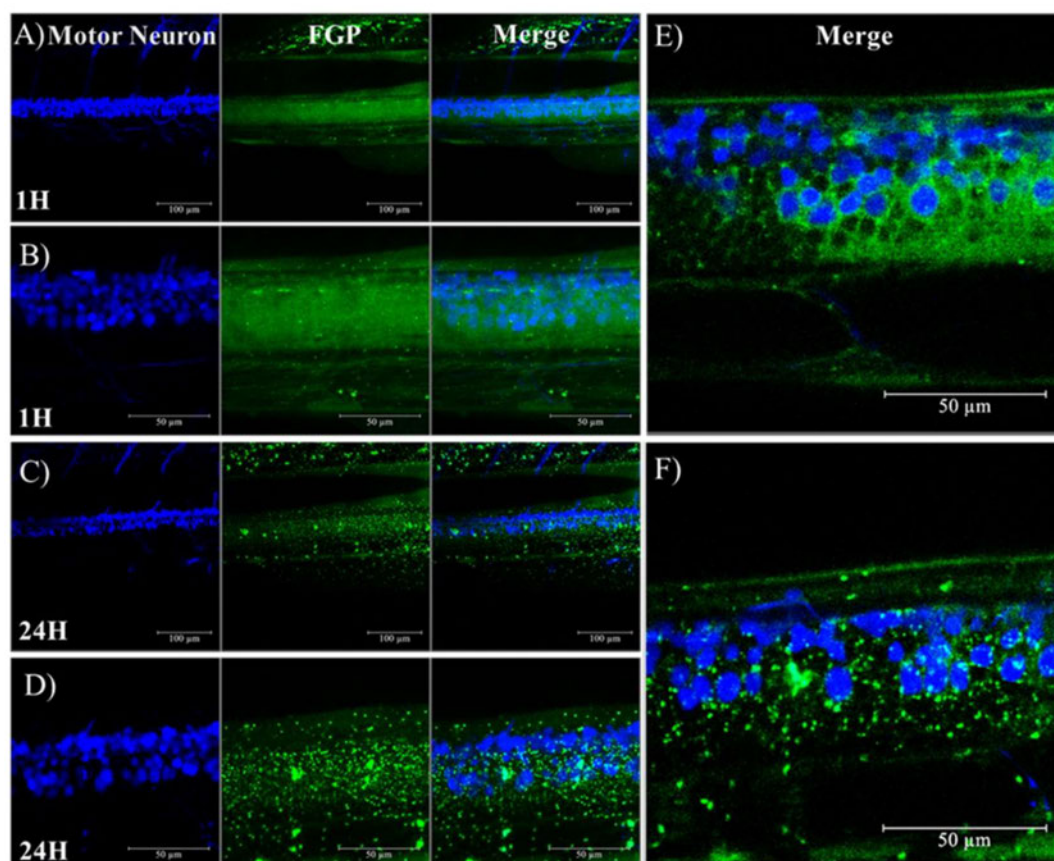
Figure S3. The bio-distribution of FGP-Tf at 1H and 24H after Intraspinal injection. A~D are the FACS overlay images of FGP-Tf in the spinal cord. E, F are the single layer FACS image of FGP-Tf in spinal cord.

Figure S4. The bio-distribution of FGP at 1H and 24H after Intraspinal injection.

A~D are the FACS overlay images of FGP in the spinal cord. E, F are the single

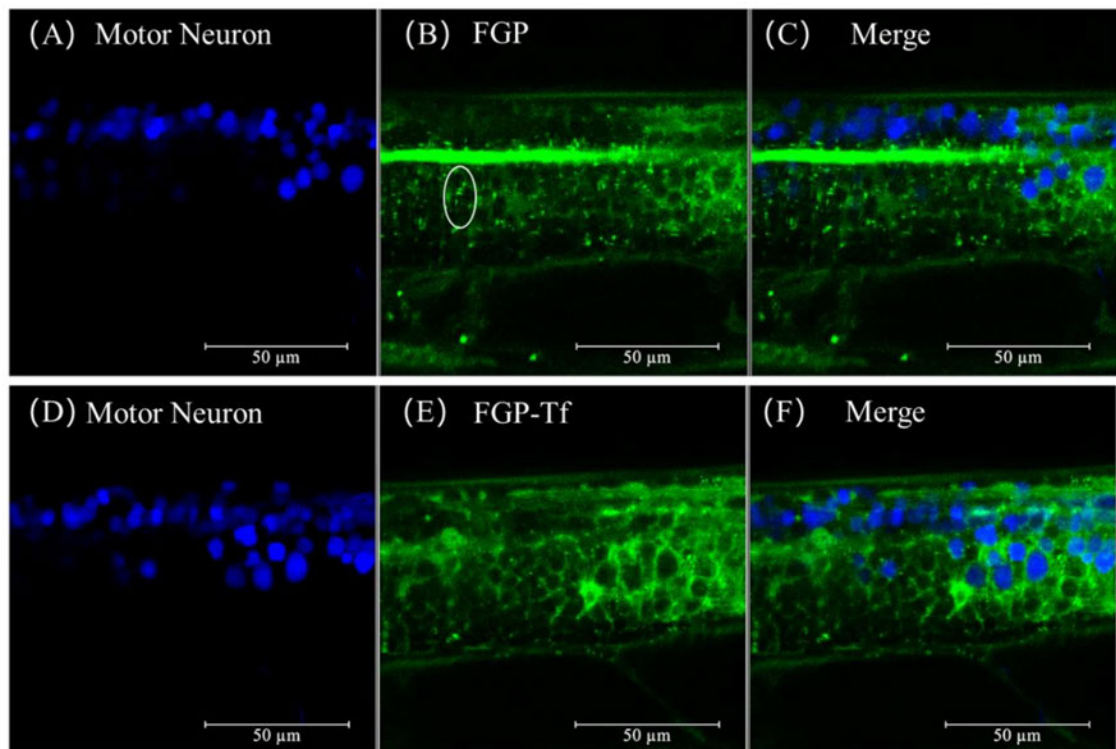layer FACS image of FGP in spinal cord.

Figure S5. The spinal cord distribution of FGP and FGP-Tf after 6h intraspinal injection. A~D are the FACS overlay images of FGP in the spinal cord. E, F are the single layer FACS image of FGP in the spinal cord.
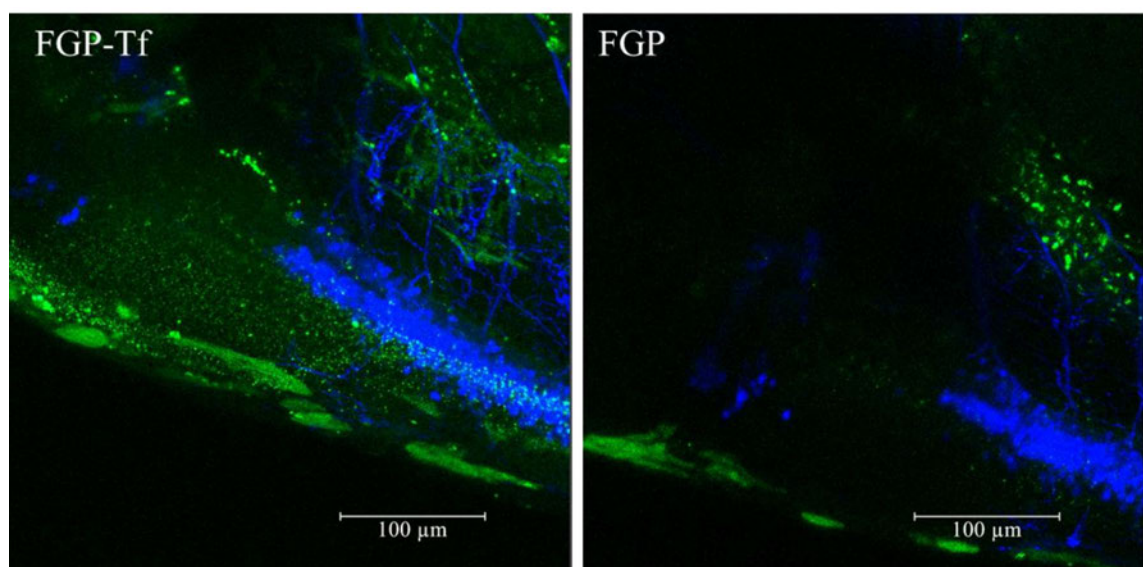

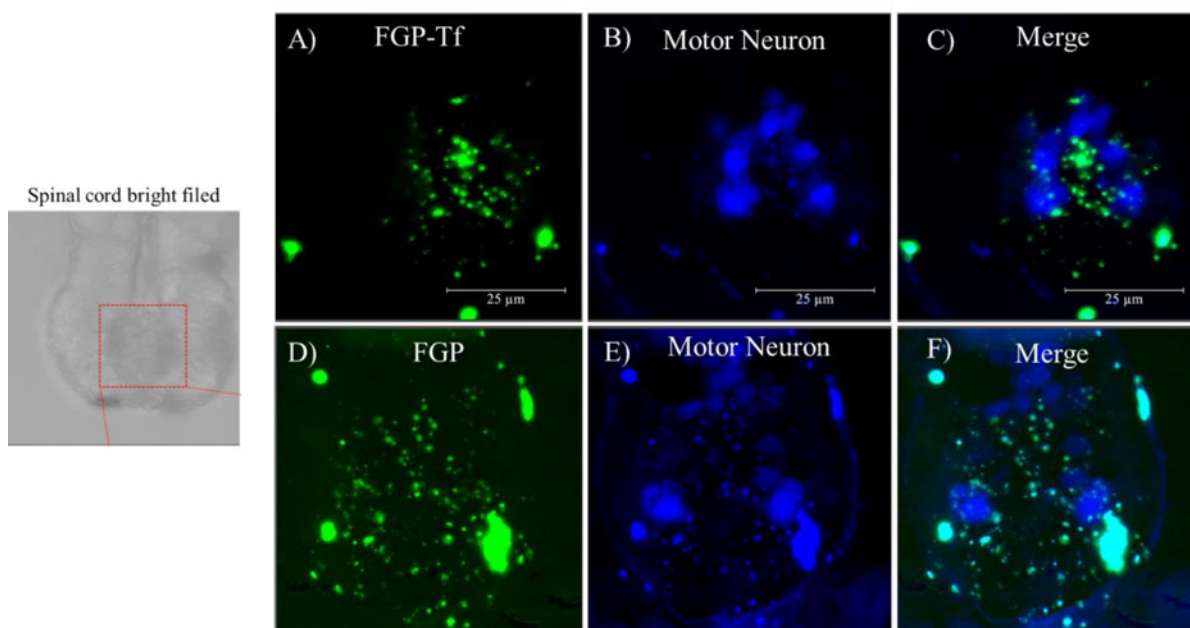Figure S6. The diffusion distance of FGP and FGP-Tf in CNS system after Intraspinal Injection.

Figure S7. Confocal images of the FGP-Tf (A-C) and FGP (D-F) distribution in spinal cord. Green signals were from intrinsically fluorescent PAMAM. Blue signals were from gene-edited motor neurons.

Reference:

1.   Hardiman, O.; Al-Chalabi, A.; Chio, A.; Corr, E. M.; Logroscino, G.; Robberecht, W.; Shaw, P. J.; Simmons, Z.; Van Den Berg, L. H., *Nature Reviews Disease Primers* **2017,** *3*, 17071.

2.   Van Damme, P.; Robberecht, W.; Van Den Bosch, L., *Dis. Models Mech.* **2017,** *10* (5), 537-549.

3.   Furtado, D.; Björnmalm, M.; Ayton, S.; Bush, A. I.; Kempe, K.; Caruso, F., *Adv. Mater.* **2018,** *30* (46), 1801362.

4.   Re, F.; Gregori, M.; Masserini, M., *Maturitas* **2012,** *73* (1), 45-51.

5.   Poovaiah, N.; Davoudi, Z.; Peng, H.; Schlichtmann, B.; Mallapragada, S.; Narasimhan, B.; Wang, Q., *Nanoscale* **2018,** *10* (36), 16962-16983.

6.   Mazibuko, Z.; Choonara, Y. E.; Kumar, P.; Du Toit, L. C.; Modi, G.; Naidoo, D.; Pillay, V., *J. Pharm. Sci.* **2015,** *104* (4), 1213-1229.

7.   Jin, Q.; Cai, Y.; Li, S.; Liu, H.; Zhou, X.; Lu, C.; Gao, X.; Qian, J.; Zhang, J.; Ju, S., *Theranostics* **2017,** *7* (4), 884.

8.   Zheng, M.; Tao, W.; Zou, Y.; Farokhzad, O. C.; Shi, B., *Trends Biotechnol.* **2018,** *36* (5), 562-575.

9.   Luong, D.; Kesharwani, P.; Deshmukh, R.; Amin, M. C. I. M.; Gupta, U.; Greish, K.; Iyer, A. K., *Acta Biomater.* **2016,** *43*, 14-29.

10.   Igartúa, D. E.; Martinez, C. S.; Temprana, C. F.; Alonso, S. d. V.; Prieto, M. J., *Int. J. Pharm.* **2018,** *544* (1), 191-202.

11.   Mignani, S.; Bryszewska, M.; Zablocka, M.; Klajnert-Maculewicz, B.; Cladera, J.; Shcharbin, D.; Majoral, J.-P., *Prog. Polym. Sci.* **2017,** *64*, 23-51.

12.   Trzepiński, P.; Klajnert‐Maculewicz, B., *J. Chem. Technol.* **2017,** *92* (6), 1157-1166.

13.   Chen, M.; Yin, M., *Prog. Polym. Sci.* **2014,** *39* (2), 365-395.

14.   Denora, N.; Laquintana, V.; Lopalco, A.; Iacobazzi, R. M.; Lopedota, A.; Cutrignelli, A.; Iacobellis, G.; Annese, C.; Cascione, M.; Leporatti, S., *J. Controlled Release* **2013,** *172* (3), 1111-1125.

15.   Biswas, S.; Deshpande, P. P.; Navarro, G.; Dodwadkar, N. S.; Torchilin, V. P., *Biomaterials* **2013,** *34* (4), 1289-1301.

16.   Chen, N.; He, Y.; Su, Y.; Li, X.; Huang, Q.; Wang, H.; Zhang, X.; Tai, R.; Fan, C., *Biomaterials* **2012,** *33* (5), 1238-1244.

17.   Tsai, Y.-J.; Hu, C.-C.; Chu, C.-C.; Imae, T., *Biomacromolecules* **2011,** *12* (12), 4283-4290.

18.   Janaszewska, A.; Studzian, M.; Petersen, J. F.; Ficker, M.; Paolucci, V.; Christensen, J. B.; Tomalia, D. A.; Klajnert-Maculewicz, B., *Colloids Surf. B. Biointerfaces* **2017,** *159*, 211-216.

19.   Wang, G.; Fu, L.; Walker, A.; Chen, X.; Lovejoy, D. B.; Hao, M.; Lee, A.; Chung, R.; Rizos, H.; Irvine, M., *Biomacromolecules* **2019**.

20.   Tomalia, D. A.; Klajnert-Maculewicz, B.; Johnson, K. A.-M.; Brinkman, H. F.; Janaszewska, A.; Hedstrand, D. M., *Prog. Polym. Sci.* **2018**.

21.   Mekuria, S. L.; Debele, T. A.; Tsai, H.-C., *Rsc Advances* **2016,** *6* (68), 63761-63772.

22.   Kari, G.; Rodeck, U.; Dicker, A. P.,   *Clin. Pharmacol. Ther.* **2007,** *82* (1), 70-80.

23.   Evensen, L.; Johansen, P. L.; Koster, G.; Zhu, K.; Herfindal, L.; Speth, M.; Fenaroli, F.; Hildahl, J.; Bagherifam, S.; Tulotta, C., *Nanoscale* **2016,** *8* (2), 862-877.

24.   Li, Y.; Song, X.; Yi, X.; Wang, R.; Lee, S. M.-Y.; Wang, X.; Zheng, Y., *ACS Appl. Mater. Interfaces* **2017,** *9* (44), 39048-39058.

25.   Pitt, J. A.; Kozal, J. S.; Jayasundara, N.; Massarsky, A.; Trevisan, R.; Geitner, N.; Wiesner, M.; Levin, E. D.; Di Giulio, R. T., *Aquat. Toxicol.* **2018,** *194*, 185-194.

26.   Li, Y.; He, H.; Jia, X.; Lu, W.-L.; Lou, J.; Wei, Y., *Biomaterials* **2012,** *33* (15), 3899-3908.

27.   Urbiola, K.; Blanco-Fernández, L.; Navarro, G.; Rödl, W.; Wagner, E.; Ogris, M.; de Ilarduya, C. T., *Eur. J. Pharm. Biopharm*   **2015,** *94*, 116-122.

28.   Yoo, J.-W.; Chambers, E.; Mitragotri, S., *Curr. Pharm. Des.* **2010,** *16* (21), 2298-2307.

29.   Chang, H.; Yhee, J. Y.; Jang, G. H.; You, D. G.; Ryu, J. H.; Choi, Y.; Na, J. H.; Park, J. H.; Lee, K. H.; Choi, K., *J. Controlled Release* **2016,** *244*, 205-213.

30.   Gomez-Garcia, M. J.; Doiron, A. L.; Steele, R. R.; Labouta, H. I.; Vafadar, B.; Shepherd, R. D.; Gates, I. D.; Cramb, D. T.; Childs, S. J.; Rinker, K. D., *Nanoscale* **2018,** *10* (32), 15249-15261.

31.   Suk, J. S.; Xu, Q.; Kim, N.; Hanes, J.; Ensign, L. M., *Adv. Drug Del. Rev.* **2016,** *99*, 28-51.

32.   Schöttler, S.; Becker, G.; Winzen, S.; Steinbach, T.; Mohr, K.; Landfester, K.; Mailänder, V.; Wurm, F. R., *Nat. Nanotechnol.* **2016,** *11* (4), 372.

33.   Saraiva, C.; Praça, C.; Ferreira, R.; Santos, T.; Ferreira, L.; Bernardino, L., *J. Controlled Release* **2016,** *235*, 34-47.

34.   Gromnicova, R.; Davies, H. A.; Sreekanthreddy, P.; Romero, I. A.; Lund, T.; Roitt, I. M.; Phillips, J. B.; Male, D. K., *PLoS One* **2013,** *8* (12), e81043.

35.   Clark, A. J.; Davis, M. E., *Proc. Natl. Acad. Sci. U. S. A.* **2015,** *112* (40), 12486-12491.

36.   O'Brown, N. M.; Pfau, S. J.; Gu, C., *Genes Dev.* **2018,** *32* (7-8), 466-478.

37.   Aday, S.; Cecchelli, R.; Hallier-Vanuxeem, D.; Dehouck, M.; Ferreira, L., *Trends Biotechnol.* **2016,** *34* (5), 382-393.

38.   Zhang, Y.-N.; Poon, W.; Tavares, A. J.; McGilvray, I. D.; Chan, W. C., *J. Controlled Release* **2016,** *240*, 332-348.

39.   Fischer, M.; Zimmerman, A.; Zhang, E.; Kolis, J.; Dickey, A.; Burdette, M. K.; Afaghpour-Becklund, M.; Chander, P.; Foulger, S. H.; Brigman, J. L., *bioRxiv* **2019**, 609354.

40.   Agrawal, A.; Min, D.-H.; Singh, N.; Zhu, H.; Birjiniuk, A.; Von Maltzahn, G.; Harris, T. J.; Xing, D.; Woolfenden, S. D.; Sharp, P. A., *ACS Nano* **2009,** *3* (9), 2495-2504.

41.   Kwon, E. J.; Skalak, M.; Lo Bu, R.; Bhatia, S. N., *ACS nano* **2016,** *10* (8), 7926-7933.

42.   Jo, D. H.; Kim, J. H.; Lee, T. G.; Kim, J. H., *Nanomed. Nanotechnol. Biol. Med.* **2015,** *11* (7), 1603-1611.

Chapter 6 Conclusion and Future Scope

6.1 Conclusion

Since their first use in 30 years ago, PAMAM dendrimers have been extensively investigated as nanocarriers and nanoprobes for drug/gene delivery and bio-imaging [1]. To date, more than 200 different kinds of PAMAM dendrimers have been created [2]. 20 years ago, the intrinsic fluorescence was first observed in a carboxylate-terminated PAMAM dendrimers, after that several intrinsically fluorescent PAMAM dendrimers have emerged for efficiency gene/drug delivery and intracellular tracking [3]. Due to their inherent fluorescence, those PAMAM dendrimers can achieve transporting and bio-imaging simultaneously [4]. In this thesis, we successfully produced a new label free fluorescent PAMAM (FG5) with strong green fluorescence. Due to the inherent fluorescence, the cellular uptake and intracellular localization of FG5 can be directly imaged through fluorescent microscopy, and the quantitative analysis of intracellular and extracellular amount of FG5 can be easily acquired through flow cytometer and fluoro photometer. Without any fluorophore labelling, treatment of dendrimers with chemical, adjusting pH, or oxidation process [4], FG5 has shown great advantages to traditional fluorophore labelled PAMAM.

In chapter 3, anti-cancer drug DOX has been efficiently encapsulated into the PEGylated fluorescent PAMAM (FGP/DOX) and displayed higher cell uptake and more effective therapeutic efficacy than hydrophobic DOX and G5/DOX alone. The excellent intracellular tracking capability of FG5 were warrant to deliver other clinical important drugs. In chapter 4, the intrinsically fluorescent PAMAM were further functionalized with transferrin for enhancing BBB penetration. The neuron protection drug Edaravone was efficiently encapsulated into PEGylated FG5 (FGP/EDV) and Tf modified FG5 (FGP-Tf/EDV). Elevated neuron protection function and enhanced BBB penetrating was achieved by FGP-

Tf/EDV drug delivery system, evidenced by higher neuron viability and lower ROS level in oxidation stress cell models and a higher transportation rate in an *in vitro* BBB model. Further evaluation of neuron protection effects will be considered to use ALS mouse models (e.g. SOD1, TDP-43).

In chapter 5, we have developed a simple and efficient zebrafish platform to evaluate their' *in vivo* behaviours, such as bioimaging, circulation in blood stream, biodistribution, biological barriers penetration, thus providing basis for optimizing IF-PAMAM based nanomedicines design. Our data suggested that these nanoprobes have excellent *in vivo* bio-imaging capability, and the FGP-Tf with prolonged blood circulation, low retention in liver and high efficiency in penetrating BSCB possessed more advantages than FGP for potential drug delivery. The brain and spinal cord distribution of FGP and FGP-Tf through local injection suggested that those nanoparticles can evenly diffuse in the entire brain and spinal cord and can be effectively uptake by neurons and astrocytes, thus it is possible to further study the therapeutic efficiency and safety of drug loaded IF-PAMAM system via directly intraspinal cord and intracranial injection.

In summary, our fabricated F-PAMAM has shown excellent *in vivo* and *in vitro* tracking and imaging capability, also these F-PAMAM has exhibited outstanding drug delivery efficiency. Further evaluation of these drug delivery system by ALS mouse models was warranted for investigation. We believe those intrinsically fluorescent PAMAM can be used in more biological fields.

6.2 Future Scope

Through the comprehensive study in this thesis, we also found some limitations regarding the drug delivery and bio-imaging from our fabricated intrinsically fluorescent PAMAM. Firstly, the drug release from those PAMAM dendrimer carriers still showed boost release within first 2 h, surface conjugation of drugs with stimulated responsible linkers or surface crosslinking with biodegradable polymers may be applied for better drug release control. Secondly, the PEGylated

PAMAM and Tf functionalized PAMAM only showed limited BBB penetrating capability and most of particles were more likely been trapped inside the brain blood vessel endothelial cells that hinder their application for CNS drug delivery. Further modification of those nanoparticles with enhanced endothelial cell escaping function may benefit their capability of passing through BBB [5], thus increasing the drug accumulation in the CNS. Finally, even though the FGP or FGP-Tf has shown excellent diffusion in brain and spinal cord and can be effectively uptake by neurons and astrocytes, this kind of cellular endocytosis was non-selective. Thus, engineering those PAMAM dendrimers with cell specific targeting agents may benefit their "on target" effect in the desired disease sites [6]. As we previously discussed in the literature review, several groups, such as bacterial toxins or antibodies that target neurons and axon compartment gangliosides, may be valuable candidates that can be used to engineer these intrinsic fluorescence PAMAM for better neurons targeting. Here, compare with I.V. injection, we also need to provide more evidence to prove the safety of local injection in the brain or spinal cord. Currently, I.V. injection is the safest way, local injection in the spinal cord is also a possible option as some drugs are directly injected in the intrathecal with less side effects. It's also worth noting that due to some limitations of zebrafish as an animal model, such as the difficulty in simulating real disease states, we will consider using more common used ALS mouse models (e.g. SOD1, TDP-43) to further evaluate the therapeutic efficiency of these nanocomposites.

Besides drug delivery and bio-imaging, those novel intrinsically green fluorescent PAMAM dendrimers also show great potential for gene delivery and tissue engineering. For example, the surface of IF-PAMAM can be modified with pH sensitive positively charged polymer that can deliver gene to target sites with traceable signal. In addition to generation 5 PAMAM, we also found this kind of fluorescent behaviour can be applied to a variety of amino group-terminal

dendritic macromolecules, like G0~G4 PAMAM dendrimers and different molecular weight Polyethylenimine (PEI). Therefore, it's possible to fabricate intrinsically green fluorescent macromoleclar polymer for tissue engineering through cross-linking of those fluorescent molecules.

Reference:

[1] P. Rao, M.M. Yallapu, Y. Sari, P.B. Fisher, S. Kumar, Designing novel nanoformulations targeting glutamate transporter excitatory amino acid transporter 2: Implications in treating drug addiction, Journal of personalized nanomedicine 1(1) (2015) 3.

[2] I. Posadas, S. Monteagudo, V. Cena, Nanoparticles for brain-specific drug and genetic material delivery, imaging and diagnosis, Nanomedicine 11(7) (2016) 833-849.

[3] D.A. Tomalia, B. Klajnert-Maculewicz, K.A.-M. Johnson, H.F. Brinkman, A. Janaszewska, D.M. Hedstrand, Non-traditional intrinsic luminescence: inexplicable blue fluorescence observed for dendrimers, macromolecules and small molecular structures lacking traditional/conventional luminophores, Progress in Polymer Science 90 (2019) 35-117.

[4] A. Janaszewska, M. Studzian, J.F. Petersen, M. Ficker, V. Paolucci, J.B. Christensen, D.A. Tomalia, B. Klajnert-Maculewicz, Modified PAMAM dendrimer with 4-carbomethoxypyrrolidone surface groups-its uptake, efflux, and location in a cell, Colloids Surf. B. Biointerfaces 159 (2017) 211-216.

[5] A.J. Clark, M.E. Davis, Increased brain uptake of targeted nanoparticles by

adding an acid-cleavable linkage between transferrin and the nanoparticle core, Proceedings of the National Academy of Sciences 112(40) (2015) 12486-12491.

[6] P. Kesharwani, S. Banerjee, U. Gupta, M.C.I.M. Amin, S. Padhye, F.H. Sarkar, A.K. Iyer, PAMAM dendrimers as promising nanocarriers for RNAi therapeutics, Materials Today 18(10) (2015) 565-572.

Appendix

1. Ethics clearance

MACQUARIE University

ANIMAL RESEARCH AUTHORITY (ARA)

AEC Reference No.: 2015/033-22   **Date of Expiry:** 10 December 2019

Full Approval Duration: 11 December 2015 to 10 December 2019

This ARA remains in force until the Date of Expiry (unless suspended, cancelled or surrendered) **and will only be renewed upon receipt of a satisfactory Progress Report before expiry (see Approval email for submission details).**

Principal Investigator:
Professor Roger Chung
Faculty of Medicine and Health Sciences
Macquarie University, NSW 2109
roger.chung@mq.edu.au

Associate Investigators:
Marco Morsch
Emily Don
Vinod Sundaramoorthy
Lucy da Silva

Others:
Alison Hogan
Rowan Radford
Sharron Chow
Dr Adam Svahn
Katherine Robinson
Ariuntugs Ultziikhutag
Libing Fu
Guoying Wang
Andres Vidal-Itriago
Natalie Scherer
Michael Udoh
Cindy Maurel

> **In case of emergency, please contact:**
> the Principal Investigator / Associate Investigator named above
> **Or Animal Welfare Officer:** 9850 7758 / 0439 497 383

The above-named are authorised by MACQUARIE UNIVERSITY ANIMAL ETHICS COMMITTEE to conduct the following research:

Title of the project: Using zebrafish to understand how the central nervous system responds to neuronal stress and death caused by neurodegenerative diseases

Purpose: 5 - Research: Human or Animal Health and Welfare

Aims: To investigate:
1. How motor neuron disease (MND)-causing genes trigger dysfunction
2. How glia respond to motor neurons expressing MND disease, and how glial activation may influence disease progression.
3. How MND-causing proteins may cause the spreading wave of neurodegeneration that characterises MND.
4. Putative therapeutics that can rescue MND-like defects in motor neurons expressing MND-causing genes.

Surgical Procedures category: 9 - Production of Genetically Modified Animals

All procedures must be performed as per the AEC-approved protocol, unless stated otherwise by the AEC and/or AWO.

Maximum numbers approved (for the Full Approval Duration):

Species	Strain	Age/Weight/Sex	Total	Supplier/Source
23 - Fish	Zebrafish (Danio rerio)	Larvae	15 000	Bred In-house
23 - Fish	Zebrafish (Danio rerio)	Adult	7 200	Bred In-house
			TOTAL 22 200	

Location of research:

Location	Full street address
FMHS Laboratory	Level 1, F10A, 2 Technology Place, Macquarie University, NSW 2109

Amendments approved by the AEC since initial approval:

1. Amendment #1 - Addition of Rola Bazzi as Animal Technician/Research Assistant (Executive approved 05/04/2016. Ratified by AEC 14 April 2016).
2. Amendment #2 - Addition of Dr Adam Svahn as Post-Doctoral Researcher (Executive approved. Ratified by AEC 16 June 2016).
3. Amendment #3 - Amend Zebrafish husbandry protocol to allow for the live collection of sperm and eggs for cryopreservation and IVF (Approved by AEC 16 June 2016).
4. Amendment #4 - Add Bianca Varney as weekend fish feeder and health check (Executive approved. Ratified by AEC 07/12/2016).
5. Amendment #5(a) - Additional substances for administration (Approved by AEC 07/12/2016).
6. Amendment #5(b) - Additional procedures (Approved by AEC 07/12/2016).
7. Amendment #6 - Add Alina Maschirow as Visiting Scholar (Executive approved. Ratified by AEC 16 February 2017).
8. Amendment #7- Add Katherine Robinson as Fish Feeder (Executive approved. Ratified by AEC 16 March 2017).
9. Amendment #8 - Add Ariuntugs Ulziikhutag as Fish Feeder (Executive approved. Ratified by AEC 16 March 2017).
10. Amendment #9 - Define the role of Fish Feeder (Executive approved. Ratified by AEC 12 April 2017).
11. Amendment #10 - Remove Dasha Monisha Syal from protocol (Executive approved. Ratified by AEC 20 July 2017).
12. Amendment #11 - Remove Bianca Varney from protocol (Executive approved. Ratified by AEC 20 July 2017).
13. Amendment #12 - Remove Isabel Formella from protocol (Executive approved. Ratified by AEC 20 July 2017).

Amendments approved by the AEC since initial approval (cont'd):

14. Amendment #13(b) - Add Libing Fu as PhD Student (Executive approved. Ratified by AEC 16 November 2017).
15. Amendment #13(c) - Add Guoying Wang as PhD student (Executive approved. Ratified by AEC 16 November 2017).
16. Amendment #14 - Add Andres Vidal-Itriago as PhD Student (Executive approved. Ratified by AEC at 22 March 2018 meeting).
17. Amendment #15 - Add Natalie Scherer as PhD Student (Executive approved. Ratified by AEC at 22 March 2018 meeting).
18. Amendment #16(a) - Remove Nicholas Cole (Approved by AEC at 22 March 2018 meeting).
19. Amendment #16(b) - Remove Rola Bazzi (Approved by AEC at 22 March 2018 meeting).
20. Amendment #16(c) - Remove Alina Maschirow (Approved by AEC at 22 March 2018 meeting).
21. Amendment #17 - Add Emily Don as Associate Investigator (Executive approved. Ratified by AEC at 22 March 2018 meeting).
22. Amendment - 01/11/2018 - Remove Jack Stoddart, Nicholas Cole and Serene Gwee from protocol (Approved by AEC 13 December 2018).
23. Amendment – 06/02/2019 - Add Iucy da Silva as Associate Investigator (Executive approved. Ratified by AEC at 14 February 2019 meeting).
24. Amendment – 04/06/2019 – Add Michael Udoh to project (Executive approved. Ratified by AEC 18 July 2019).
25. Amendment – 26/08/2019 – Addition of previously approved SOPs to project (Approved by AEC 19 September 2019).
26. Amendment – 17/09/2019 – Add Cindy Maurel to project (Executive approved. Ratified by AEC 17 October 2019).

Conditions of Approval: N/A

Being animal research carried out in accordance with the Code of Practice for a recognised research purpose and in connection with animals (other than exempt animals) that have been obtained from the holder of an animal suppliers license.

A/Professor Nathan Hart (Chair, Animal Ethics Committee)   **Approval Date: 17 October 2019**